



Katholieke Universiteit Leuven

Faculteit Wetenschappen
Departement Wiskunde
Centrum voor Plasma-Astrofysica

Koninklijke Sterrenwacht van België

SIDC - Departement Zonnestraling



New techniques for the characterisation of dynamical phenomena in solar coronal images

Eva Robbrecht

Promotoren:

Prof. dr. S. Poedts
Dr. D. Berghmans

Proefschrift voorgelegd tot
het bekomen van de graad van
Doctor in de Wetenschappen

Juryleden:

Prof. dr. C. Aerts
Prof. dr. M. Goossens
Prof. dr. R. Howard
Prof. dr. R. Keppens
Dr. R.A.M. Van der Linden

Leuven, februari 2007

Acknowledgements:

The research in this work was partially funded by Contract C90188
"SECCHI Preparation to Exploitation and Exploitation"
(BELSPO, ESA/PRODEX)

SOHO is a project of international collaboration ESA/NASA

Thanks

My thesis has proven that ‘ $2 + 2 = 5$ for extremely large values of 2’. It is only thanks to the large added value, in whatever unit, of the people in my surroundings that you are holding now this small book in your hands. It is the end product of a journey that began in the Centre for Plasma-Astrophysics (CPA) in Leuven and ended in the Royal Observatory of Belgium (ROB). I thank Marcel and Stefaan for offering me a 3-year position at the CPA. While giving examples classes in ‘Higher mathematics’, I was glad to finally understand the courses that I had attended myself as a student. However, my encounter with the theory of magnetohydrodynamics turned me into a student again. I am grateful to Ronald, for the many explanations he gave with superhuman patience. Having gone through the theory, I turned towards the Sun and wondered how things would happen in reality.

I thank my colleagues for offering me a job in the space weather pilot project. I am indebted to David, Jean-François (JF), Ronald and Frédéric for the time and effort they have invested in writing the SIDC project proposal. I know few people with such an amount of spirit, energy and dedication. The Solar Physics department at the ROB is a wonderful place to work. The green environment in our ‘circle’ reflects the open atmosphere that characterizes the department. Particularly I want to thank David, my co-promotor, for supervising my work and for giving me the guardianship over CACTus. He created many possibilities for me and introduced me in the international community of scientists. I also want to thank JF and Ronald for their precious time dedicated to interesting discussions.

The composition of our office has changed over the course of time, but I’m happy that Petra, Lena and Bogdan stayed nearby in an ‘always ready to help’ state. I have consulted them regularly for their areas of specialization, respectively direct problem solving, crazy science and computer business. I want to thank all my colleagues for making attempts in answering my questions and for disagreeing with me for the sake of the discussion. Special thanks for reading parts of the manuscript (Christophe, Matthieu), for making coffee (Christophe et al.), strong coffee (Bogdan) and tea (Judith) and for being a real clown (Matthieu).

This thesis is not written at work alone. I want to thank my parents for the good home they created, in which we could grow up and develop ourselves. The most beautiful present they gave me are my three sisters. Thanks Toska, Hanka and Saskia for keeping me connected to the real life!

Contents

Abstract	1
1 Instrumentation and data	5
1.1 The Extreme ultraviolet Imaging Telescope	6
1.2 Large Angle and Spectrometric Coronagraph	8
I Waves in the Corona	11
2 The MHD model	13
2.1 The MHD equations	13
2.2 Three types of basic MHD waves	15
2.3 The non-uniform corona	17
3 Slow magnetoacoustic waves in coronal loops	19
3.1 Waves observed in the corona	19
3.2 Data analysis	21
3.2.1 Our data-set: JOP80	21
3.2.2 Analysis of the data	25
3.2.3 Discussion	34
3.3 Conclusion and future outlook	37
II Coronal mass ejections	39
4 Automated CME detection	41
4.1 Introduction to coronal mass ejections	41
4.1.1 CME observation and dynamics	42
4.1.2 Observational limitations	44
4.1.3 Conceptual models of CME initiation	44
4.2 Motivation for automated detection	45
4.3 Detailed description of the method	45
4.3.1 Data	46
4.3.2 Preprocessing	46
4.3.3 Detection	48
4.4 Validation of the method	51
4.4.1 General results	53

4.4.2	Measurement of spatial CME parameters	54
4.4.3	Velocity measurement	56
4.5	Discussion	57
5	Statistical analysis of coronal mass ejections during cycle 23	61
5.1	Composition of the catalog	61
5.2	CME rate during cycle 23	63
5.3	Illustrations of the CME definition ambiguities	67
5.3.1	Shocks	67
5.3.2	Halo CMEs	71
5.3.3	Loop opening	72
5.4	Statistics of CME parameters	72
5.4.1	Detection of first appearance	73
5.4.2	Apparent width of CMEs	75
5.4.3	Apparent latitude of CMEs	79
5.4.4	Apparent speed of CMEs	83
5.5	Conclusion	84
6	Solar Image Processing	87
6.1	Introduction	87
6.2	Disappearing filaments in H α images	89
6.3	Dimmings and EIT waves	92
6.4	Erupting prominences in radio images	93
6.5	CMEs in coronagraphic white light images	94
6.6	Discussion	97
	Summary and Conclusions	99
	Appendices	101
A	The effect of a sound wave on spectral line profiles	101
B	Comparative table of a CACTus and CDAW output	103
C	The box-and-whisker plot	105
	Nederlandstalige samenvatting	107
	Bibliography	111

Abstract

During a total solar eclipse, a narrow strip of the Earth's surface is shielded completely by the Moon from the disk of the Sun. In this strip, the corona appears crown-like around the shade of the Moon. It was uncertain until the middle of the 20th century whether the corona was a solar phenomenon or if it was related to the Moon or whether it represented an artifact produced by the Earth's atmosphere. The answer to this question was provided by Grotrian (1939) and Edlèn (1942). Based on studies of iron emission lines, they suggested that the surface of the Sun is surrounded by a hot tenuous gas having a temperature of million degrees Kelvin and thus in a state of high ionization. This discovery was a result from spectroscopy, a field of research which started in 1666 with Sir Isaac Newton's observations of sunlight, dispersed by a prism.

It is now clear that the hot solar corona is made of a low density plasma, highly structured by the magnetic field on length scales ranging from the Sun's diameter to the limit of angular resolution (e.g. Démoulin and Klein 2000). The need to resolve and study the corona down to such scales has determined a vigorous scientific and technological impulse toward the development of solar Ultraviolet (UV) and X-ray telescopes with high spatial and temporal resolution. With the advent of the satellite SOHO (Solar and Heliospheric Observatory, see chapter 1), the picture of a quiet corona was definitely sent to the past. EUV (Extreme UV) image sequences of the lower solar corona revealed a finely structured medium constantly agitated by a wide variety of transients (e.g. Harrison 1998). Active regions consisting of large magnetic loops with enhanced temperature and density are observed, as well as 'quiet' areas, coronal holes and numerous structures of different scales such as plumes, jets, spicules, X-ray bright points, blinkers, all structured by magnetic fields. Launched in 1998, the Transition Region And Coronal Explorer (TRACE) was an important step on the way to subarcsecond telescopes. It allows a spatial resolution of 1'' in the EUV and UV bands and, simultaneously, a temporal resolution of the order of a few seconds.

Coronal physics studies are dominated by two major and interlinked problems: coronal heating and solar wind acceleration. Above the chromosphere there is a thin transition layer in which the temperature suddenly increases and density drops. How can the temperature of the solar corona be three orders of magnitude higher than the temperature of the photosphere? In order for this huge temperature gradient to be stationary, non-thermal energy must be transported from below the photosphere towards the chromosphere and corona and converted into heat to balance the radiative and conductive losses. This puzzle of origin, transport and conversion of energy is referred to as the 'coronal heating problem'. Due to its fundamental role in the structuring of the corona, the magnetic field is supposed to play an important role in the heating.

In this dissertation we describe two aspects of solar coronal dynamics: waves in coronal loops (Part I) and coronal mass ejections (Part II). We investigate the influence of (semi-) automated techniques on solar coronal research. This is a timely discussion since the observation of solar phenomena is transitioning from manual detection to ‘Solar Image Processing’. Our results are mainly based on images from the Extreme UV Imaging Telescope (EIT) and the Large Angle and Spectrometric Coronagraph (LASCO), two instruments onboard the satellite SOHO (Solar and Heliospheric Observatory) of which we recently celebrated its 11th anniversary. The high quality of the images together with the long timespan created a valuable database for solar physics research.

Part I reports on the first detection of slow magnetoacoustic waves in transequatorial coronal loops observed in high cadence image sequences simultaneously produced by EIT and TRACE (Transition Region And Coronal Explorer). Ten years of EUV observations made it clear that these disturbances are a widespread phenomenon in active region loops. The existence of these waves in the corona had been predicted by the theory of magneto-hydrodynamics (MHD), which we revise briefly. Just like in helioseismology, coronal seismology uses observations of oscillations to derive physical parameters which are not directly measurable, such as the Alfvén speed or the magnetic field strength. The comparison with helioseismology does not fully hold in the sense that the dense photosphere does not allow any seeing inside. Instead, for the corona we do have direct observations, but because of its optical thinness these observations leave space for many interpretations.

At the end of the forties, it was suggested that the corona could be heated by the dissipation of acoustic waves (sound waves) driven by the p-mode oscillations, generated by turbulence in the convection zone. While they travel upwards, these waves form shocks and heat the plasma by viscous dissipation. Nowadays, they are believed to be only important for lower chromospheric heating. By the time the upper chromosphere is reached, the acoustic waves are heavily damped and what rests is reflected by the steep temperature and density gradients in the transition zone. As such, they cannot deposit enough energy in the corona to sufficiently heat it to the observed temperatures. Dissipation of magnetic energy by Alfvén waves or directly by the reconnection process in current sheets are considered to be more likely to heat the corona.

Part II addresses the question of detecting coronal mass ejections (CMEs) in coronagraphic white light data. The study of CMEs is a rather young (~ 30 years) field of research. Coronal mass ejections are sudden expulsions of mass and magnetic field from the solar corona into the interplanetary medium. A classical CME carries away some 10^{15} g of coronal mass and can liberate energies of $10^{23} - 10^{25}$ J. They are often observed in association with low coronal activity, such as flares and filament eruptions. During the first years of CME observation, it was believed that a flare was a necessary condition for CME occurrence. The widely accepted picture today is that flares and CMEs are both different manifestations of magnetic field restructuring through reconnection (flare) and the expulsion of mass (CME). Up till now, the SOHO mission has been the best mission for CME studies because of the increased resolution, cadence, sensitivity and dynamic range of the LASCO instruments, but also because of the large array of ground-based instruments (Howard 2006). The complexity of the CME-picture grew likewise. The next mission with a coronagraph is the NASA STEREO mission (Solar Terrestrial Relations Observatory), launched on 26 Oct. 2006.

In chapter 4 we test the possibility of automatically detecting CMEs in LASCO data.

We describe the algorithm CACTus (Computer Aided CME Tracking) and test its validity on a short period of 6 days. In chapter 5 we present our newly constructed CME catalog based on our automated detection scheme. It is the first automatically generated catalog which runs over a complete solar cycle (cycle 23). It required no human interaction, which implies it is totally objective. It includes all transients obeying the observational definition of CME as a ‘new, discrete, bright, white-light feature in the coronagraph field-of-view moving radially outward’ (Hundhausen et al. 1984). As a result, our catalog contains much more events, mostly narrow, than are included in the classical CDAW CME catalog (Yashiro et al. 2004) which is assembled manually. We discuss the CME rate over the solar cycle and present important new statistics on the CACTus CME parameters (size, latitude, speed).

CME research has gained an increased interest due to their strong *space weather* impact. Space weather is defined by the European Space Agency (ESA)¹ as the ‘conditions on the Sun and in the solar wind, magnetosphere, ionosphere and thermosphere that can influence the performance and reliability of space-borne and ground-based technological systems and can endanger human life or health.’ The significance of space weather lies in its potential impact on man-made technologies on Earth and in space, for example, on satellites and spacecraft, electricity power grids, pipelines, radio and telephone communications and on geophysical exploration. Space weather also has implications for manned space flight, both in Earth orbit and further out into space. Solar activity is the main source of space weather. It is now well established that CMEs are the primary cause of geomagnetic storms and that their associated shocks accelerate high energetic particles. These particles can directly and indirectly influence the operation of spacecraft and affect communication and navigation. In order to protect systems and people that might be at risk from space weather effects, we need to understand the causes of space weather and try to predict its impact on the heliosphere as soon as possible. A growing field in this respect is Solar Image Processing (SIP). It allows continuous monitoring and interpretation of new incoming data. This is not only interesting for space weather forecasting, but it is also needed to be able to handle efficiently the large data flow which is expected from recently launched and future missions. In chapter 6 we revise the current capabilities for automated detection of CMEs and related phenomena.

¹ESA Space Weather web server is at <http://esa-spaceweather.net/>

Chapter 1

Instrumentation and data

The Solar and Heliospheric Observatory (SOHO Fleck et al. 1995) is a mission of international cooperation between the European Space Agency (ESA) and the National Aeronautics and Space Administration (NASA) to study the Sun, from its deep core to the outer corona, the solar wind, and the interaction with the interstellar medium. ESA was responsible for the development of the spacecraft while NASA's responsibilities include its launch and operations. The spacecraft was launched from the Cape Canaveral Air Station (Florida, United States) on 2 December 1995 and placed into a halo orbit around the First Lagrangian Point (L1). The L1 point is approximately 1.5 million kilometers sunward from the Earth (about four times the distance to the Moon). This position allowed for the first time an uninterrupted view on our remote Sun. All previous solar observatories have orbited the Earth, from where their observations were periodically interrupted when our planet 'eclipsed' the Sun.

SOHO was designed for a nominal mission lifetime of two years. Because of its spectacular success it has been granted several extensions with the last extension guaranteeing a lifetime until Dec. 2009. This allows SOHO to cover a complete 11-year solar cycle, but also it will offer a third eye in addition to the two STEREO spacecraft which was launched on 25 October 2006. Utilizing two identical spacecraft - one ahead and one behind the Earth - the Solar Terrestrial Relations Observatory (STEREO) will offer us a first 3D view of the sun.

The scientific payload of SOHO comprises 12 complementing instruments¹. CDS (Coronal Diagnostic Spectrometer), CELIAS (Charge, Element, and Isotope Analysis System), COSTEP (Comprehensive Suprathermal and Energetic Particle Analyzer), EIT (Extreme ultraviolet Imaging Telescope), ERNE (Energetic and Relativistic Nuclei and Electron experiment), GOLF (Global Oscillations at Low Frequencies), LASCO (Large Angle and Spectrometric Coronagraph), MDI/SOI (Michelson Doppler Imager / Solar Oscillations Investigation), SUMER (Solar Ultraviolet Measurements of Emitted Radiation), SWAN (Solar Wind Anisotropies), UVCS (Ultraviolet Coronagraph Spectrometer), VIRGO (Variability of Solar Irradiance and Gravity Oscillations). They can be classified in three categories depending on their field of study:

The solar interior: GOLF and VIRGO perform long-term, uninterrupted series of oscillations measurements of the full solar disk, respectively in velocity and in the irradiance domain. In this way, information is obtained about the solar interior. SOI/MDI measures oscillations on the surface of the Sun with high angular resolution, providing precise information about the Sun's convection zone - the outer layer of the solar interior.

¹<http://sohowww.nascom.nasa.gov/instruments>

The solar atmosphere: SUMER, CDS, EIT, UVCS, and LASCO constitute a suite of telescopes, spectrometers and coronagraphs that observe the hot atmosphere of the Sun, the corona, extending far above the visible surface. SUMER, CDS and EIT observe the inner corona. UVCS and LASCO observe both inner and outer corona. They gather measurements of the temperature, density, composition and velocity in the corona, and follow the evolution of coronal structures with high resolution.

The solar wind: CELIAS, COSTEP and ERNE analyze in situ the charge state and isotopic composition of ions in the solar wind, and the charge and isotopic composition of energetic particles generated by the Sun. SWAN compiles maps of the hydrogen density within the heliosphere, starting from $20 R_{\odot}$. It uses telescopes sensitive to a particular wavelength of hydrogen, allowing the large-scale structure of the solar wind streams to be measured.

The research reported in this thesis focuses on transients in the low and high corona and is based on EUV observations from EIT and TRACE (Handy et al. 1999) and white light observations from LASCO. Below we describe in more detail the EIT and LASCO instruments.

1.1 The Extreme ultraviolet Imaging Telescope

The EIT instrument (EIT, Delaboudinière et al. 1995) onboard SOHO produced new observations of the corona in the EUV temperature range of 1 to 2 MK. Because UV is mostly absorbed by the Earth’s ionosphere these observations are not possible with ground based instruments. EIT provides full-disk images of the Sun at four selected bandpasses in the extreme UV, mapping the low corona and transition region up to $1.5 R_{\odot}$ from Sun-center ($1 R_{\odot} = 1$ solar radius $\approx 700\,000$ km). Normal incidence multilayer optics are used to image the Sun on an EUV sensitive 1024×1024 charged coupled device (CCD) camera. This was relatively new technology in the early nineties. By dividing the telescope mirrors into quadrants it was possible to isolate the emissions from narrow temperature ranges by ‘tuning’ the coatings of each quadrant to the desired passband (Table 1.1). A rotating mask allows only a single multilayer-coated quadrant of the telescope to be illuminated by the Sun at any time.

Wavelength	Ion	Peak Temperature	Observational Objective
304 Å	He II	8.0×10^4 K	Chromospheric network, coronal holes
171 Å	Fe IX-X	1.3×10^6 K	Corona/Transition Region boundary, structures inside coronal holes
195 Å	Fe XII	1.6×10^6 K	Quiet corona outside coronal holes
284 Å	Fe XV	2.0×10^6 K	Active regions

Table 1.1: EIT bandpasses, adapted from Delaboudinière et al. (1995)

Uninterrupted by occultations by the Earth, EIT allowed access to a frequency domain in dynamical analysis that had been previously inaccessible in soft X-ray and EUV observations due to such periodic gaps in the data. Analysis of EIT data has illustrated how variable the solar atmosphere is. Its high spatial and temporal resolution confirmed the pervasive variability of EUV structures and lead to a re-evaluation of the term ‘quiet

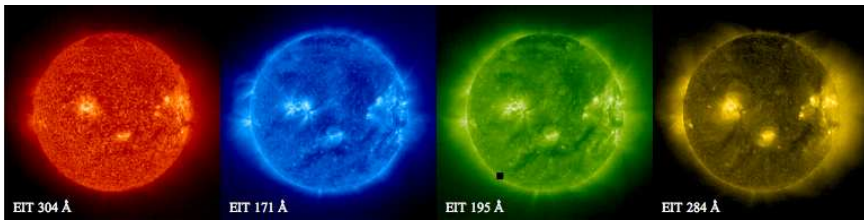


Figure 1.1: Images produced by the EIT instrument on 2004/08/24 for the 4 selected bandpasses as described in Table 1.1. The colors are artificial. The left image differs from the other images, since it shows the chromospheric network. The remaining images show the hot solar corona, with increasing temperature to the right. The chromosphere and corona are separated by a thin layer in which the temperature rises steeply over two orders of magnitude.

sun' (Moses et al. 1997, Mason 1999). Also the study of the structure and dynamics of polar coronal holes was heavily boosted due to the new coronal observations. The images from EIT and also from TRACE (Handy et al. 1999) gave a strong impulse to the field of coronal seismology. In the mid nineties, very few *imaging* observations of the corona (e.g. eclipse observations, spectroheliograms) existed with a pixel resolution high enough to observe oscillations spatially. Movies in the Fe XII spectral line showed new outflow in polar plumes, which was interpreted by Deforest and Gurman (1998) as acoustic wave motions and was later also observed in coronal loops (Berghmans et al. 1998). Analysis of these first observations will be discussed in the next chapter. Beside waves, many other coronal transients had been newly discovered or could be studied more thoroughly thanks to the better resolution, temporal coverage and longer duration of the sequences. Newly discovered EUV jets were seen to emerge from the EUV bright network in the polar coronal holes, other than their soft X-ray counterparts. Macrospicules were observed at the boundaries of coronal holes. These had been extensively studied in Skylab observations (e.g. Bohlin et al. 1975), but the limited duration and frequency of the observations couldn't fully resolve interpretation ambiguity. Other coronal transients observed are brightenings (Berghmans et al. 1998, they are the coronal counterpart of blinkers in the transition region), explosive events (supersonic transients), coronal rain and tadpoles. Apart from these small scale transients SOHO allowed better multi-thermal analysis of coronal loops.

Further, the EIT synoptic full-Sun observations are ideally suited to witnessing the overall solar activity and indicate source regions of flares and coronal mass ejections. This instrument has thus not only led to a wealth of discoveries of transient phenomena, but also serves as a continuous eye monitoring the main source of disturbed space weather.

1.2 Large Angle and Spectrometric Coronagraph

LASCO² (Brueckner et al. 1995) is a set of two (originally three) coronagraphs jointly observing the solar corona from near the solar limb to a distance of $30 R_{\odot}$, that is about one seventh the Sun - Earth distance. This instrument was the first to observe the corona beyond $10 R_{\odot}$. The invention of the coronagraph by Lyot in 1930 had opened the way for observations of the corona at times other than during total solar eclipses. The instrument is essentially a telescope that artificially eclipses direct solar radiation by occulting the solar disc and projects scattered light onto the focal plane. In addition, it utilizes special features to minimize the instrumental stray light (Brueckner et al. 1995), that is light scattered within the instrument. Since the corona is much fainter than the photosphere (e.g. $< 10^{-6} B_{\odot}$ at the limb and $< 10^{-8} B_{\odot}$ at $3 R_{\odot}$ with B_{\odot} the photospheric brightness), stray light suppression is the most demanding technical requirement for a coronagraph. Ground based coronagraphs additionally suffer from stray skylight and, therefore, cannot directly observe the white light K-corona (electron scattered), other than using polarization filters. This instrument is used at several high altitude observatories permitting routine ground-based observations of the inner corona out to $\sim 2.5 R_{\odot}$. Beyond this point the faint corona can only be observed from space, using external occulters. The father of the externally occulted coronagraph is J. W. Evans (1948). It is basically a Lyot coronagraph with a circular occulting disk placed in front of the entrance aperture such that no direct sunlight falls into the instrument (Koomen et al. 1975). In externally occulted coronagraphs the largest single source of stray light is the ring of diffracted sunlight from the edge of the occulting disk. This can be largely reduced by adding more disks on a common spindle, where each disk intercepts the diffracted light from the edge of the one before. A remaining source of stray light is scattering from the lenses itself, due to macroscopic inhomogeneities in the glass or surface inhomogeneities (like scratches). The advent of superpolished mirrors and extremely smooth coatings greatly reduced the residual scatter. The problems of scatter are so severe that the making of satisfactory coronagraphs remains an art. Evans for example describes the techniques, including polishing the surface with 'nose oil':

"Wash the hands in detergent or a solvent to remove all traces of grease. Then touch the side of the nose with a forefinger and lightly touch the surface of the lens in two or three spots leaving distinct finger marks. Now take a very clean, soft cloth and bunch it into a pad [...]. With short, vigorous strokes spread the oil from the finger marks into an extremely thin film over the surface. This requires a good pressure, and progress can be determined by feel. The friction in polished areas is very noticeably less than on the bare glass. If the lens is held in direct sunlight and viewed against a dark background, the polished area will appear more brilliant (i.e. darker) than the bare glass. Care must be used to avoid too much nose oil on the surface. One soon learns with a little experience." (Excerpt from Golub and Pasachoff 1997)

The LASCO coronagraphs have stray light levels which are an improvement of at least one order of magnitude over previously flown coronagraphs (Brueckner et al. 1995), such

²Online LASCO handbook: <http://lasco-www.nrl.navy.mil/>

Telescope	Field of view	Bandpass	Occluder	Resolution
C1	1.1 - 3.0 R_{\odot}	narrow	internal	5.6 "
C2	2.0 - 6.0 R_{\odot}	white light	external	11.4 "
C3	3.7 - 30.0 R_{\odot}	white light	external	56 "

Table 1.2: LASCO instrument details

that the faint outer corona could be recorded as far as 30 R_{\odot} against the black sky of the outer space.

Beginning in January 1996, three LASCO coronagraphs C1, C2 and C3 imaged the solar corona from 1.1 to 3 R_{\odot} (C1), from 2.0 to 6.0 R_{\odot} (C2) and from 3.7 to 30 R_{\odot} (C3). The CME detection study described in chapter 4 is only based on data from C2 and C3. C1 is an internally occulted coronagraph, in which the light from the solar disk is eliminated by a mirror. A tunable Fabry-Perot interferometer allows the selection of 5 spectral regions with a resolution of 0.07 nm, by means of a broadband blocking filter 5 nm wide. After the loss of SOHO in June 1998, the C1 telescope was damaged and could not be used anymore. C2 and C3 are both externally occulted and measure broadband photospheric light scattered by the free electrons and dust particles in the corona. The major disadvantage of external occultation is the poor spatial resolution near the edges of the occulter, due to vignetting (the occulter has to be slightly oversized and this shadows the inner edge of the field of view (FOV)). This limits observing the corona by externally occulted coronagraphs to a finite distance of the solar limb ($> 1.5 R_{\odot}$). LASCO overcomes these problems by using three different coronagraphs with overlapping FOVs. The three LASCO cameras record their images on a front-side illuminated CCD of 1024×1024 pixels. The imaging area is a 21.5 mm square, achieving a pixel resolution of respectively 5.6, 11.4 and 56 arc-sec. A composite LASCO C2-C3 image is shown in Fig. 1.2. Two different large-scale structures are easily identifiable. The bright structures of straight lines fanning out from Sun center are coronal ‘streamers’, overlying the polarity inversion line. The second large-scale structure, only visible in the upper panel, are coronal mass ejections, appearing as circular cones erupting from the east and west. As a consequence of this solar activity, the lower panel is contaminated by protons and electrons.

Altogether the LASCO experiment offers significant improvements with respect to previous instruments of its kind. Earlier long-term coronal observations have been acquired by several space missions: OSO-7 (1971-72 Koomen et al. 1975), Skylab (1973-74 MacQueen et al. 1974), Solwind on the P78-1 satellite (1979-1985 Koomen et al. 1975, Sheeley et al. 1980) and the Solar Maximum Mission (1980-1989 MacQueen et al. 1980). Pioneering images of the inner heliosphere are expected from the Sun Earth Connection Coronal and Heliospheric Investigation package (SECCHI, Howard et al. 2002) onboard the twin STEREO spacecraft. It is a suite of remote sensing instruments consisting of an extreme ultraviolet imager (EUVI), two LASCO equivalent white light coronagraphs (COR1 and COR2) to explore the inner and outer corona from 1.25 to 15 R_{\odot} and a wide field heliospheric imager (HI) to image the inner heliosphere from the outer corona to beyond the Earth, between 12 and 318 R_{\odot} . The most novel instrument, HI, extends the concept of traditional externally occulted coronagraphs. Its FOV will not be sun-centered but side-looking, occulting the sun and brightest part of the corona at one edge of the FOV. Additionally, a small baffle over the top of the objective lens protects it from earthshine.

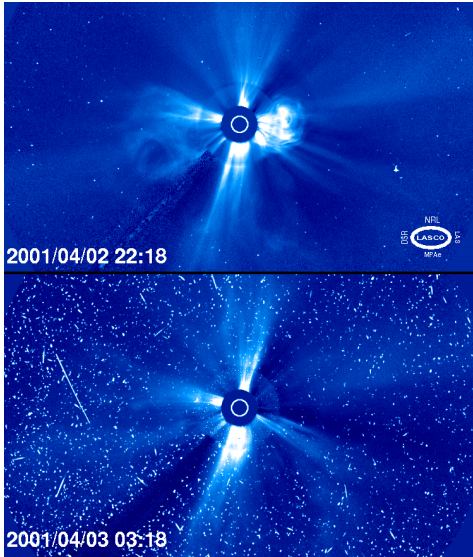


Figure 1.2: Two composite LASCO C2-C3 images showing the outer solar corona in white light. The blue color is artificial. The images are formed by sunlight scattered by electrons in the corona. Bright means thus higher electron density than dark. The white circle in the middle indicates the size of the solar disk. The bright dots in the upper panel are mostly due to stars and cosmic rays, moving through the LASCO field of view. They can be easily removed from the images by applying a median filter. The lower panel is additionally contaminated by energetic particles as a consequence of solar activity.

To optimize the stray light requirements, HI is also split into two telescopes, HI-1 and HI-2. The HI instruments, with their unique FOV, will provide the first direct imaging observations of CMEs in the inner heliosphere.

Part I
Waves in the Corona

Chapter 2

The MHD model

This chapter describes the theoretical framework in which solar coronal waves were first proposed. An extensive description and motivation of the MHD theory can be found in many textbooks (Goedbloed and Poedts 2004, Goossens 2003, Aschwanden 2004).

2.1 The MHD equations

A plasma consists of a highly ionized gas. In many plasmas in the solar system (e.g. the solar corona) the magnetic and the electric fields largely control the motion of particles. Such plasmas can be described using the model of magnetohydrodynamics (MHD). The equations governing the MHD model are the equations of fluid mechanics combined with the Maxwell equations. These describe a plasma as a magnetized fluid using the approximation of quasi-neutrality and not considering kinetic effects due to the interaction of individual particles. Moreover it is assumed that velocities are non-relativistic. In quantitative terms this means we assume length scales larger than the mean free paths (~ 30 km in the corona, derived from parameters given in the NRL plasma formulary 2004 revised) and time scales large compared to the collisional time scales (of the order of a second for the corona). For the phenomena described in this thesis these assumptions are valid and sufficiently satisfied. Nevertheless, it is important to realize that the magnetohydrodynamic approach to plasma physics is subject to limitations.

In hydrodynamic (HD) terms a single fluid plasma is characterized by the following parameters: density ρ , pressure p and speed v . In MHD we have additionally a vector \mathbf{B} describing the magnetic induction. Variables printed in bold denote vector quantities. In 3D this brings the total number of unknowns to 9. For a perfect gas, thermodynamic quantities ρ , p and T are connected by the perfect gas law:

$$p = \frac{k_B}{m} \rho T \quad (2.1)$$

where k_B is the Boltzmann constant and m the mean particle mass. We thus can eliminate

the temperature and are left with 8 unknowns.

$$\frac{\partial \rho}{\partial t} + \nabla \cdot (\rho \mathbf{v}) = 0 \quad (2.2)$$

$$\rho \left[\frac{\partial \mathbf{v}}{\partial t} + (\mathbf{v} \cdot \nabla) \mathbf{v} \right] = -\nabla p + \frac{1}{\mu} (\nabla \times \mathbf{B}) \times \mathbf{B} - \rho \mathbf{g} \quad (2.3)$$

$$\frac{\partial p}{\partial t} + \mathbf{v} \cdot \nabla p = \frac{\gamma p}{\rho} \left(\frac{\partial \rho}{\partial t} + \mathbf{v} \cdot \nabla \rho \right) + \underbrace{(\gamma - 1) \eta j^2}_{\text{underbraced}} \quad (2.4)$$

$$\frac{\partial \mathbf{B}}{\partial t} = \nabla \times (\mathbf{v} \times \mathbf{B}) - \underbrace{\eta \nabla^2 \mathbf{B}}_{\text{underbraced}} \quad (2.5)$$

$$\nabla \cdot \mathbf{B} = 0 \quad (2.6)$$

Equations 2.2 to 2.5 form a basic set of 8 nonlinear partial differential equations describing a non-viscous plasma under the assumptions made by magnetohydrodynamics, where we have neglected the viscosity. The underbraced terms describe the effects of electric resistivity. These terms are neglected in the model of ideal MHD in which it is assumed that no energy is dissipated. **Equation 2.6** is the solenoidal constraint, an initial condition for the induction equation which states that no magnetic monopoles exist.

Equation 2.2 is the *continuity equation* and expresses the simple fact that mass only changes due to motion (in and out a volume) and not due to creation or annihilation. It thus expresses the conservation of mass. **Equation 2.3** is the *equation of motion*. It expresses Newton's first law of mechanics: $\mathbf{F} = m\mathbf{a}$, i.e. forces (\mathbf{F}) cause masses (m) to accelerate (\mathbf{a}). Apart from the force due to the magnetic field \mathbf{B} all other forces (written at the right hand side) are also present in hydrodynamics (HD). They are the force due to the plasma pressure gradient $-\nabla p$, the force due to an external gravitational field \mathbf{g} and the viscous force $\rho\nu\nabla^2\mathbf{v}$. In MHD we have additionally the *Lorentz force* $\mathbf{j} \times \mathbf{B}$, from which the current density \mathbf{j} is eliminated by Ampère's law

$$\mathbf{j} = \frac{\nabla \times \mathbf{B}}{\mu}, \quad (2.7)$$

with $\mu = \mu_0$, the magnetic permeability in vacuum. **Equation 2.4** is the *internal energy equation*. If we neglect the dissipative term, it states that the pressure is only changed by reversible compression (or expansion) of the plasma. γ denotes the ratio of the specific heats, at constant pressure and at constant volume. When hydrogen is fully ionized $\gamma = \frac{5}{3}$; this is a good approximation for the solar corona. **Equation 2.5** describes the evolution of the *magnetic induction* \mathbf{B}^1 . The righthand side of this equation consist of two parts. The first term describes the tendency of the magnetic field lines to be convected with the fluid, while the second term describes the decay of the magnetic field due to the magnetic diffusivity η , defined as $\frac{1}{\mu\sigma}$, where σ denotes the electrical conductivity. In the perfectly conducting limit (adopted in ideal MHD) $\eta = 0$, so that only the first term remains. According to the frozen-flux theorem, introduced by Alfvén, the magnetic field can then be regarded as frozen into the plasma. For the corona this is usually a good approximation, because the motions appear on a time scale τ much shorter than the diffusion time scale τ_d , the time scale on which the second term of Eq. 2.5 influences the magnetic field. This

¹From here on we refer to \mathbf{B} as the magnetic field which is common practice in solar physics.

is expressed by a large magnetic Reynolds-number, defined as the ratio of these typical time scales $R_m \equiv \tau/\tau_d$.

The Lorentz force

After applying a vector identity for the triple vector product $(\nabla \times \mathbf{B}) \times \mathbf{B}$, the Lorentz force can be rewritten as

$$\mathbf{j} \times \mathbf{B} = (\mathbf{B} \cdot \nabla)\mathbf{B}/\mu - \nabla(B^2/(2\mu)).$$

From the cross product $\mathbf{j} \times \mathbf{B}$ we already know that the Lorentz force should not have a component along the magnetic field. Indeed, expanding further the first term and splitting the ∇ -operator in a component along (∇_{\parallel}) and across (∇_{\perp}) the magnetic field, we are left with a force normal to the magnetic field

$$\begin{aligned} \mathbf{j} \times \mathbf{B} &= \nabla_{\parallel}(B^2/2\mu) + \frac{B^2}{\mu R_c} \mathbf{e}_n - (\nabla_{\parallel}(B^2/2\mu) + \nabla_{\perp}(B^2/2\mu)) \\ &= \frac{B^2}{\mu R_c} \mathbf{e}_n - \nabla_{\perp}(B^2/2\mu). \end{aligned} \quad (2.8)$$

where \mathbf{e}_n is the unity vector normal to the magnetic field line in the opposite direction of the local center of curvature and R_c is the local curvature radius. The smaller R_c is, the more curved are the field lines. The first RHS term in Eq. 2.8 is the magnetic tension force which tries to straighten the field lines. In the limit of straight magnetic field lines ($R_c \rightarrow \infty$) this term vanishes. The second term is the magnetic pressure force and exists when the magnetic field pressure $B^2/2\mu$ varies across the magnetic field. It is directed from high to low field strength. The sum of the thermal pressure and the magnetic pressure gives the total pressure

$$p_T = p + B^2/2\mu.$$

The ratio of the plasma pressure to the magnetic pressure is called the plasma- β

$$\beta = \frac{p}{B^2/2\mu}.$$

When $\beta \ll 1$ we have a so-called low plasma- β , meaning that the magnetic pressure dominates the total pressure. This is the case in the highly magnetized low density corona where $\beta \approx 0.01$.

2.2 Three types of basic MHD waves

Every type of wave is the result of a restoring force as reaction to a small perturbation and travels with its typical speed, depending on the parameters of the medium. After excitation, a wave can be damped giving its energy to the medium. Sound waves (also called acoustic waves or sonic waves) for example exist in neutral fluids and gases, due to the pressure restoring force. In 1940 Hannes Alfvén was awarded the Nobel Prize for Physics for *his contributions and fundamental discoveries in magnetohydrodynamics and*

their fruitful applications in different areas of plasma physics. His best-known contribution is the discovery of a new kind of waves, which we now call *Alfvén waves* (Alfvén 1942). These waves are not directly visible because they consist of oscillations of the magnetic field without density perturbations. Nevertheless, Alfvén waves are now believed to play a key-role in the mechanisms for fast solar wind acceleration and coronal heating. In the highly magnetized corona, pure sound waves do not exist. They are linked to the magnetic pressure force, creating *fast and slow magnetoacoustic waves*. Chapter 3 describes the earliest detections of propagating intensity disturbances in coronal loops, which we have interpreted as slow magnetoacoustic waves. Higher pressure means higher density, in EUV observations acoustic waves appear thus as intensity variations (as a matter of fact, the intensity is proportional to ρ^2).

To introduce the three basic wave modes (fast and slow magnetosonic and Alfvén), we use the ideal MHD model, neglect gravity and study small amplitude perturbations of a uniform static plasma. We perturb the static equilibrium by an infinitesimally small displacement vector field $\boldsymbol{\xi}(\mathbf{r}, t)$. This small perturbation causes a local disturbance in all plasma parameters: $\rho = \rho_0 + \delta\rho$, $p = p_0 + \delta p$ and $\mathbf{B} = \mathbf{B}_0 + \delta\mathbf{B}$. We linearize the equations by neglecting squares and products of small quantities. In the linearized equations all physical variables can be eliminated in function of the displacement vector, such that only $\boldsymbol{\xi}(\mathbf{r}, t)$ appears as variable. Substituting the appropriate expressions in the equation of motion, we obtain the force-operator equation which is of the form

$$\rho_0 \frac{\partial^2 \boldsymbol{\xi}}{\partial t^2} = \mathbf{F}(\boldsymbol{\xi}), \quad (2.9)$$

where

$$\mathbf{F}(\boldsymbol{\xi}) \equiv \nabla(\boldsymbol{\xi} \cdot \nabla p_0 + \gamma p_0 \nabla \cdot \boldsymbol{\xi}) + (\nabla \times \mathbf{B}_0) \times (\nabla \times (\boldsymbol{\xi} \times \mathbf{B}_0)) + (\nabla \times (\nabla \times (\boldsymbol{\xi} \times \mathbf{B}_0))) \times \mathbf{B}_0.$$

Assuming harmonic solutions of the form

$$\boldsymbol{\xi}(\mathbf{r}, t) = \boldsymbol{\xi} e^{i(\mathbf{k} \cdot \mathbf{r} - \omega t)},$$

with \mathbf{k} the wave vector and ω the wave frequency, the following wave equation can be derived

$$\omega^2 \boldsymbol{\xi} = c_s^2 \mathbf{k}(\mathbf{k} \cdot \boldsymbol{\xi}) + v_A^2 [\mathbf{k} \times (\mathbf{k} \times (\boldsymbol{\xi} \times \hat{\mathbf{B}}_0))] \times \hat{\mathbf{B}}_0 \quad (2.10)$$

with

$$c_s \equiv \left(\frac{\gamma p_0}{\rho_0} \right)^{1/2} \quad \text{and} \quad v_A \equiv \frac{B_0}{(\mu \rho_0)^{1/2}} \quad (2.11)$$

the sound speed and the Alfvén velocity, respectively. $\hat{\mathbf{B}}_0$ denotes a unit vector in the direction of the magnetic field \mathbf{B}_0 . Using linear algebra on the three components of the vector equation 2.10 we can derive the dependence of the wave frequency ω on the wave vector \mathbf{k}

$$(\omega^2 - k_{\parallel}^2 v_A^2)(\omega^4 - k^2(c_s^2 + v_A^2)\omega^2 + c_s^2 v_A^2 k_{\parallel}^2 k^2) = 0, \quad (2.12)$$

where $k_{\parallel} = k \cos \theta_B$ is the component of \mathbf{k} along \mathbf{B}_0 . This expression is called the dispersion relation which gives an equation for the possible wave phase speed $v_p \equiv \omega/k$.

Equation 2.12 splits in two independent components

$$\omega^2 = k_{\parallel}^2 v_A^2, \quad (2.13)$$

$$\text{and} \quad \omega^2 = \frac{1}{2} k^2 (c_s^2 + v_A^2) \left[1 \pm \sqrt{1 - \frac{4k_{\parallel}^2 c_s^2 v_A^2}{k^2 (c_s^2 + v_A^2)^2}} \right]. \quad (2.14)$$

They define the frequencies of the (*shear*) *Alfvén wave* (2.13), the *fast* (+) and the *slow* (-) *magnetoacoustic wave* (2.14). Dispersion relations impose relations between the frequency (time) and the vector wave number (space) that must be satisfied in order for a wave to exist in a plasma. The requirements that electromagnetic waves in free space propagate at the speed of light ($\omega/k = c$) or that sound waves in a neutral gas propagate at the sound speed ($\omega/k = c_s$) are familiar examples of dispersion relations (Goedbloed and Poedts 2004). Equations 2.13 and 2.14 show that the phase speeds of waves in magnetized plasmas depend on the intensity of the magnetic field, the plasma density and under some conditions the direction of wave propagation \mathbf{k} . In the case of the slow magnetoacoustic wave, the plasma pressure and the magnetic pressure counteract resulting in low wave frequencies, while in the case of fast magnetoacoustic waves these two pressures act in concert. Alfvén waves arise purely from the magnetic tension force and hence do not compress the plasma. They propagate as transversal waves strictly along the magnetic field lines at a velocity equal to the Alfvén velocity. They are thus highly anisotropic, just like the slow magnetoacoustic waves, which are confined to propagate in a small cone around the magnetic field direction. The fast magnetoacoustic waves at the contrary, travel almost isotropically. In the corona (i.e. low β) they are mainly driven by the magnetic pressure force.

2.3 The non-uniform corona

As mentioned above, the properties of MHD waves in a uniform plasma, can depend strongly upon the angle θ_B between the wave vector and the magnetic field. Consequently, MHD waves are highly affected by plasma structuring, governed by the magnetic field. Soft X-ray and EUV observations have revealed the magnetic structuring of the corona. The solar surface is covered abundantly with coronal loops, appearing as bright arches on a darker background. The brightness differences are mostly due to differences in density so that loops appear as closely packed structures of hot plasma. Although no direct evidence exists, loops are assumed to outline the coronal magnetic field. In virtually all theoretical models that appeared in the literature, loops are, therefore, envisioned as magnetic flux tubes containing plasma with parameters, different from the ambient coronal parameters. The simplest representation of a loop is a straight cylindrical flux tube, described in cylindrical coordinates (r, θ, z) such that the parameters obey the following

$$\mathbf{B}_0(r), \rho_0(r), p_0(r) = \begin{cases} \mathbf{B}_i, \rho_i, p_i, & \text{for } r < a \\ \mathbf{B}_e, \rho_e, p_e, & \text{for } r > a \end{cases} \quad (2.15)$$

$r = a$ being the radius of the cylinder representing a coronal loop. The indices i and e refer to the internal and external plasma, respectively. The introduction of a boundary

between two media leads to a new branch of surface wave modes on top of the previously derived body wave modes that exist in each medium separately (Edwin and Roberts 1983, Roberts 2000). There are two branches of phase speeds: (1) a fast mode branch with phase speeds between the internal and external Alfvén speeds, containing the kink ($n = 1$) and sausage ($n = 0$) modes² and (2) a slow-mode branch with phase speeds between the internal tube speed c_T and the sound speed c_s . Because of their higher density, the characteristic speeds are lower in the loop than in the ambient corona.

The density scale height

Besides the magnetic field, gravity, which we neglected in the previous discussion, is the other agent which causes non-uniformity in the solar atmosphere. Gravitational stratification leads to an exponential decrease in pressure (and accordingly density) with height z above the photosphere. For a uniform temperature along the loop this is expressed as

$$p(z) = p_0 e^{-z/\Lambda(T)}.$$

Here

$$\Lambda = \frac{p_0}{\rho_0 g},$$

is the scale height, the length scale on which this effect has influence. Typically this is 0.15 Mm in the photosphere and 100 Mm in the corona (Priest 1984). These values are in correspondence to the scale heights, recently derived by Andries et al. (2005) based on the detection of multiple harmonics in a standing kink oscillation (Verwichte et al. 2004).

The above sketched loop model is too simple and serves only as a cartoon illustrating the influence of non-uniformity. For example, the question arises how the loop radius $r = a$ can be defined in practice. Extensions of the above model include 1D-models where the internal parameters depend on r (concentric shells) and 2D-models where they also depend on z , the coordinate along the loop axis.

² n is an integer describing the azimuthal behaviour of the oscillating tube

Chapter 3

Slow magnetoacoustic waves in coronal loops

On May 13, 1998 the EIT instrument on board of SOHO and the TRACE instrument produced simultaneous high cadence image sequences of the same active region (AR 8218). TRACE achieved a 25 sec cadence in the Fe IX (171 Å) bandpass while EIT achieved a 15 sec cadence in the Fe XII (195 Å) bandpass (operating in 'shutterless mode', SOHO JOP 80). These high cadence observations in two complementary wavelengths have revealed the existence of weak transient disturbances in an extended coronal loop system. These propagating disturbances seemed to be a common phenomenon in this part of the active region. The disturbances originate from small scale brightenings at the footpoints of the loops and propagate along the loops. The projected propagation speeds roughly vary between 65 and 150 km s⁻¹ for both instruments which is close to and below the expected sound speed in the coronal loops. The measured slow magnetoacoustic propagation speeds seem to suggest that the transients are sound (or slow) wave disturbances. The observation of sound waves along the same path probably indicates that they propagate along the same loop. Given the systematic higher speeds measured in the hotter EIT line could be consistent with sharp temperature gradients across the loops. The results have been published in Robbrecht et al. (1999) and Robbrecht et al. (2001).

3.1 Waves observed in the corona

During the seventies short period oscillations were observed in type IV radio bursts. Rosenberg (1970) suggested that these pulsations were evidence of the presence of MHD waves in the corona. Because of their short periods (0.5-3 sec) they were interpreted as fast sausage waves. In rare cases, longer periods (~ 40 sec) were also observed and were believed to be fast kink waves. In the range of standing slow MHD modes (> 500 sec) no significant observations were available. Aschwanden (1987) (Table III) made an estimation of the typical periods occurring in different structures in the corona. It was realized that the fast waves arise only as free (or body) modes in regions where the Alfvén speed is lower than the ambient Alfvén speed (see formula 2.11). Essentially, this means that fast waves only exist in high density loops which can oscillate freely. Concise reviews on these early observations are found in Roberts et al. (1984) and Aschwanden (1987).

All theoretically predicted MHD waves are now believed to be observed. Aschwanden (2004) and Nakariakov and Verwichte (2005) give a recent overview. Slowly propagat-

ing waves are visually observed in EIT (e.g. Robbrecht et al. 2001) and TRACE (e.g. De Moortel et al. 2000). Standing kink oscillations are frequently observed in TRACE loops (Aschwanden et al. 1999, Nakariakov et al. 1999, Wang and Solanki 2004). Very recently quasi-periodic transverse oscillations of dark ‘tadpole’ tails have been interpreted as propagating kink oscillations (Verwichte et al. 2005). They are located in the downward outflow region, after a high energetic X-ray flare had been observed. The first *imaging* observation of the standing sausage mode has probably been obtained with the Nobeyama heliograph and the soft X-ray telescope (SXT) aboard Yohkoh (Asai et al. 2001, Nakariakov et al. 2003). We await the first EUV observation of the sausage mode which is expected to be observed in the next generation of EUV instruments (e.g. AIA onboard SDO, see Section 3.3). Doppler shift measurements from SUMER (UV spectrometer onboard SOHO) and intensity fluctuations are studied as evidence for slow standing acoustic oscillations (Wang et al. 2002, Kliem et al. 2002).

The observation of propagating slow waves in the corona

Brekke et al. (1997) and Kjeldseth-Moe and Brekke (1998) reported the first observations of high-velocity flows in active region loop systems observed with CDS (Coronal Diagnostic Spectrometer onboard SOHO). The (line-of-sight) velocities observed at a temperature of 240 000 K are of the order of $v = 50 \pm 10 \text{ km s}^{-1}$ and are deduced from spectral line Doppler shifts using

$$v = \frac{\Delta\lambda}{\lambda}c,$$

with c the speed of light and $\Delta\lambda$ the shift in band pass λ . They found, within the same loop system, velocities in opposite directions seen in neighbouring loops. They argued these disturbances cannot not be caused by mass-flows along the loops because that would require velocity values considerably larger than the measured values. As an alternative explanation they proposed propagating magnetoacoustic waves. Previously, Eriksen and Maltby (1967) had studied the effect of propagating sound waves on the profiles of spectral lines to explain the net redshift observed in the transition region. They found that although there is no net mass motion, propagating compressive waves will cause spectral line asymmetries and line shifts in the direction of wave propagation (see appendix A for a short explanation). The speed deduced from spectral line shifts, is proportional to the density enhancement caused by the sound wave compression and reflects the back and forth motion of the particles induced by the wave. The actual *wave* speed should be close to the sound speed being roughly 74 km s^{-1} at a temperature of 240 000 K.

The quasi-periodic propagating intensity disturbances studied in this chapter were first observed during a search for transient brightenings in high cadence EIT data. This new class of weaker footpoint brightenings produced wave-like disturbances propagating along quasi-open field lines. The EIT dataset has been analyzed in detail by Robbrecht et al. (1999) and also a multi-wavelength study was performed (Robbrecht et al. 2001) comparing the 195 Å data from EIT with the 171 Å data from TRACE (see section 3.2). This allowed observing these coronal features simultaneously at different temperatures bearing characteristic wave speeds.

Ten years of EUV observations made it clear that these disturbances are a widespread phenomenon in active region loops, mainly observed in high cadence (15-30 sec) 195 Å

and 171 Å TRACE data (Nightingale et al. 1999, De Moortel et al. 2000, 2002, King et al. 2003). The observational properties of these disturbances can be summarized as follows: they propagate along loops with (projected) speeds in the range 65 - 235 km s⁻¹, are marginally detectable above the noise level (10% enhancement in intensity) and decay very fast (exponentially). Periods of around 3 and 5 minutes have been found regularly. They are not found to be related to flaring activity, but are rather believed to be a response to underlying motions.

The phenomenon of propagating disturbances along loops is comparable to the moving features observed in EUV observations of polar plumes (Deforest and Gurman 1998). They argued that these moving features are slow magnetoacoustic waves because: (1) the propagation speed was always less than the sound speed; (2) the moving features repeated in quasi-periodic trains and (3) Doppler shifts had not been reported in plumes corresponding to bulk motions at the observed speeds. Ofman et al. (1999) reported an increase in relative intensity of the features with radial distance and found a good match between the observations and a one-dimensional analytical model of spherical slow magnetoacoustic waves in a stratified atmosphere.

Nightingale et al. (1999) have analyzed the time variability of EUV brightenings in coronal loops, based on TRACE data in the 171 Å and 195 Å lines. Because these small EUV brightenings do not show temperature increases, they concluded that these small brightenings cannot be associated with upflows of heated plasma by chromospheric evaporation. Instead, their near-isothermal density enhancements seemed to be caused by compressional waves, which start near the loop footpoints and propagate along the loops with approximate sound speed.

Contrary to the acoustic wave interpretation, Reale et al. (2000) interpreted the evolution of a transient brightening of a coronal loop, observed by TRACE, in terms of an initially empty and cool magnetic flux tube along which plasma motion takes place. This interpretation is inspired by a transient heating episode occurring along the loop. It consists of a closed loop with high curvature and the authors concluded that the loop must have an inclination angle of $\sim 60^\circ$ w.r.t. the vertical. However, Nakariakov et al. (2000) have shown that the propagating disturbances in coronal loops can be interpreted as slow magnetoacoustic waves.

3.2 Data analysis

3.2.1 Our data-set: JOP80

On May 13, 1998, the EIT and TRACE instruments have produced a unique image sequence in the context of the multi-instrument campaign SOHO JOP80 (Clette et al. 1998). JOP80 is dedicated to the high resolution imaging study of coronal and transition region dynamics (EIT shutterless-mode campaign). The aim was to study bright structures (active region loops, bright points) with the highest possible time resolution (~ 15 sec) and wide spatial coverage. The first results of JOP80 have been reported by Berghmans and Clette (1999). In JOP80, EIT is the lead instrument, followed by several space-born instruments: SXT (Soft X-ray Telescope), TRACE (Transition Region And Coronal Explorer), MDI (Michelson Doppler Imager), CDS (Coronal Diagnostics Spectrometer),

Instrument	EIT	TRACE
Bandpass	195 Å	171 Å
Ion	Fe XII	Fe IX
Level	Corona	Low Corona
Temp	1.6 MK	1 MK
Cadence	15 sec	25 sec
Pixelsize	2.59" (~ 1860 km)	0.5" (~ 366 km)
starttime	17h31m50s	17h03m28s
endtime	18h29m07s	18h07m17s

Table 3.1: Characteristics of the JOP80 dataset produced by the EIT and TRACE instruments. The bandpasses of EIT Fe XII and TRACE Fe IX are narrow with a peak formation temperature of respectively 1.6 MK and 1 MK. The end time of the TRACE sequence is determined by the appearance of cosmic rays which damaged the images too much.

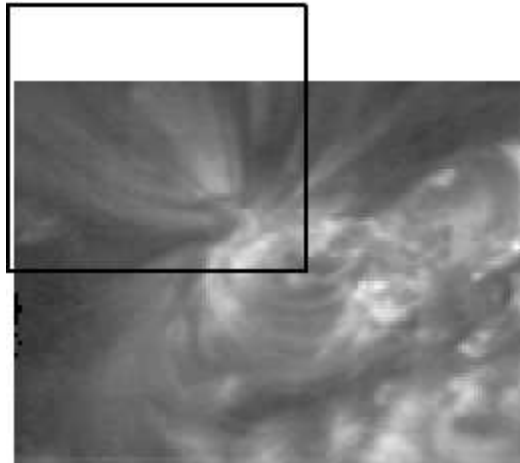


Figure 3.1: The field of view of EIT (195 Å), specified in the full disc in Fig. 3.3. The rectangle corresponds to the field of view of the TRACE observation which is shown in Fig. 3.2.

SUMER (Solar Ultraviolet Measurements of Emitted Radiation), as well as two ground based observatories (in La Palma and Sac Peak). In this analysis we only compare the EIT 195 Å data with the TRACE data in the 171 Å bandpass.

EIT data

EIT achieved an exceptional 15 s cadence in the Fe XII bandpass by leaving the instrument's shutter open for 1 hour and operating the CCD in frame transfer mode. EIT collected during the 1 hour JOP 80 run in total 229 images of 128×96 pixels (332×249

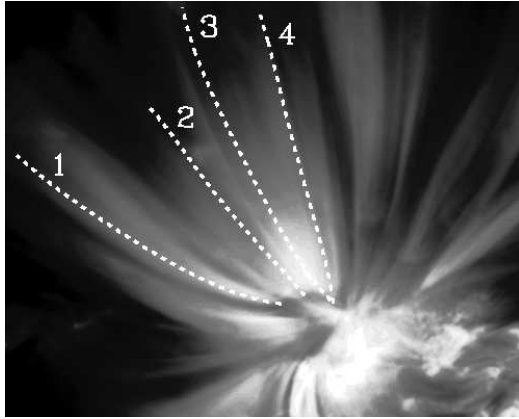


Figure 3.2: The field of view of TRACE (171 \AA), specified in Fig. 3.1. In Fig. 3.5 to Fig. 3.8 we give the characteristics of the 4 loops indicated here.

arcsec) starting at 17:31:50 UT and ending at 18:29:07 UT on 13 May 1998, yielding a time interval of 57 min and 17 s. Flat-field and grid pattern corrections have been applied to the images. In the EIT data, cosmic rays were identified as exceptional deviations (above the 5σ level) in the pixel's light curves that appear in one image only. Their values were restored by replacing the pixel's intensity with a linear interpolation from neighbouring images. See Delaboudinière et al. (1995) and Berghmans and Clette (1999) for more technical details. Due to the solar rotation, the active region shifts to the right of the field of view during the 1 hour observation campaign by less than 4 EIT pixels. This shift was compensated by determining the maximum of cross-correlation between the images.

TRACE data

The TRACE dataset consists of a datacube with a spatial size of 1024×1024 pixels and a temporal sequence of 147 images at a cadence of 26 s in the Fe IX bandpass. The image sequence starts at 17:03:28 UT and ends at 18:07:17 UT on 1998 May 13, with a total duration of 63 min and 49 s. A subregion of 400×355 pixels (200×177.5 arcsec) has been selected from the whole field of view. There is not a complete match (spatially nor temporally) between the EIT and the TRACE datasets (see Fig. 3.1 and Table 3.2.1. Due to contamination by cosmic rays, the last part of the TRACE sequence cannot be used and therefore there is only half an hour overlap between the two data sets. The TRACE images suffer substantially from noise due to the radiation belt passages. In the time period between 17h28 and 17h35 the cosmic rays are severe. The pixels hit by cosmic rays (exceeding the 6σ level) are replaced by a nearby pixel value. We removed the background diffraction pattern by applying a Fourier analysis on the data. The TRACE images were corrected for solar rotation and spacecraft jitter by determining the shift for maximum cross-correlation between the images. These preprocessing steps were performed

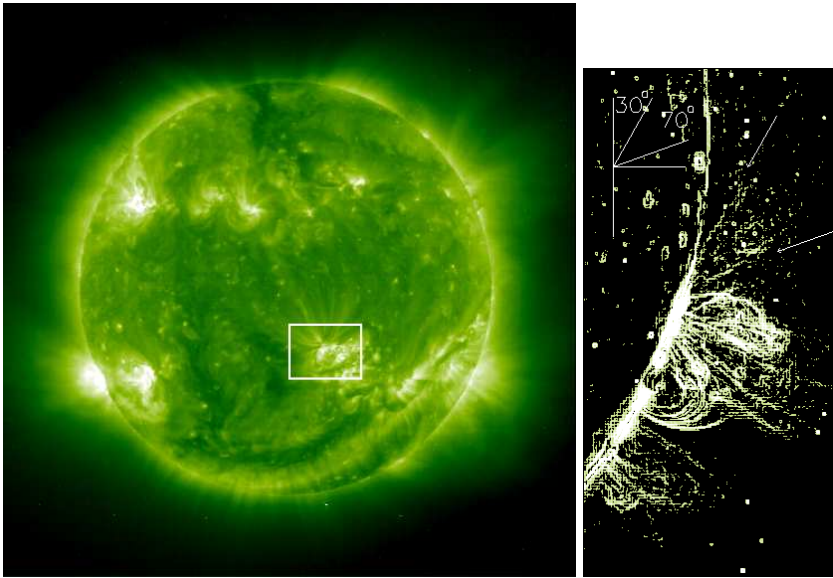


Figure 3.3: *Left*: An EIT full disc image in the Fe XII (195 Å) bandpass, taken at 18h34m UT. The rectangle indicates the active region AR 8218, it corresponds to the EIT field of view. *Right*: A side view on AR 8218 when crossing the western limb. This image has been processed to enhance the edges of the loop structure.

by using the standard calibration procedure which can be found in the SolarSoft TRACE analysis guide ¹. The internally co-aligned EIT and TRACE data cubes were then mutually co-aligned on the basis of the image headers pointing information. An improvement on this was achieved by visually identifying a relative large number (> 10) of distinctive features that could be recognized in both images. An optimal coordinate transformation is then constructed (least mean square basis) that maps the TRACE image to the EIT image and vice versa. All this results in an EIT-TRACE co-alignment better than 1-2 EIT pixels which is sufficient for the present study.

Active Region NOAA 8218

The target of the campaign was a relatively small but highly dynamical active region (NOAA 8218). It first appeared on the eastern limb on 8 May and produced several small C flares during its passage over the disk. According to the Mount Wilson magnetic classification it is defined as a beta-region. It was not visible during the previous solar rotation (~ 27 days) which indicates it is a relatively young region. In a first inventory of the dynamics of this active region during the high-cadence observation, a wide variety of transients was discovered, ranging from a B3.5 flare accompanied by a large plasma flow

¹http://www.lmsal.com/solarsoft/sswdoc/index_menu.html

along pre-existing loops to EUV versions of active region transient brightenings as previously observed by SXT on board YOHKOH (Berghmans and Clette 1999, Shimojo et al. 1998). In Fig. 3.3 (*left*), we show the overall structure of this active region. In Fig. 3.1 we focus on the bundle of long, magnetic flux tubes that emanates from it to the NE. The width of the EIT field of view is about 230 Mm ($0.34 R_{\odot}$). The bundle consists of transequatorial loops having one footpoint in the observed active region. The footpoints at the other edge of the flux tubes cannot be resolved, but seem not to be rooted in an active region. Taking profit of the solar rotation and assuming that the overall structure of this bundle remained unchanged over a period of a week, we obtained a side view of the active region when it crossed the western limb (Fig. 3.3, *right*). From this we estimate that the magnetic flux tubes in the bundle make an angle α with the plane of the sky that ranges from roughly 30° up to 70° near their footpoints. This angle will be used to estimate the effect of projection.

3.2.2 Analysis of the data

We focus on a new type of transients that was observed to propagate along the bundle of widely opening magnetic field lines to the NE of the active region. To illustrate the variability of the analyzed loop system we show in Fig. 3.4 a sequence of 4 running difference images at 171 Å and 195 Å. The pattern of diagonal lines in the TRACE sequence of difference images is an instrumental artifact. They are remains of the background diffraction pattern, which is enhanced by the differencing. Dark and bright features, outlining the whole length of a loop, suggest that the loops also experience transverse motions. In a difference movie, we see a continuous outflow of bright disturbances. After a sudden brightening at the footpoint of the fan of loops we detect a quasi-periodical radial outflow of disturbances along the loops. Fig. 3.4 illustrates the propagation of enhanced brightness by making running difference images. The propagating disturbances are indicated with a white arrow. Note that the sequences of TRACE and EIT do not correspond in time here.

We identified oscillations in several loops during the 1998 May 13 time sequence. Four paths were selected visually for detailed analysis (Fig. 3.2). We tracked the loops on the TRACE image, which has the higher resolution. We then applied a transformation to obtain the same path in the EIT data. (The transformation method is described in subsection 3.2.1, TRACE data). The width of the path is equal to the pixel size of the instrument. The path in the EIT data is generally shorter, since the field of view is smaller at the north of the active region, where the loops are tracked. By assuming a semi-circular loop, we visually estimate the length along an entire loop to be 800 Mm. The path length (projection onto the field of view) is estimated to be of the order of 100 Mm.

Slow magnetoacoustic wave interpretation

In Fig. 3.5 to Fig. 3.8 we show the temporal evolution (horizontal axis) along the four selected paths (vertical axis) in a [time,space] diagram. This type of diagram is very helpful in identifying variability (intensity and motion) along a given path. The method of placing vertical slices next to each other is also referred to as the stroboscopic method. A quadratic fit to each pixel's light curve was calculated. This quadratic fit is taken as

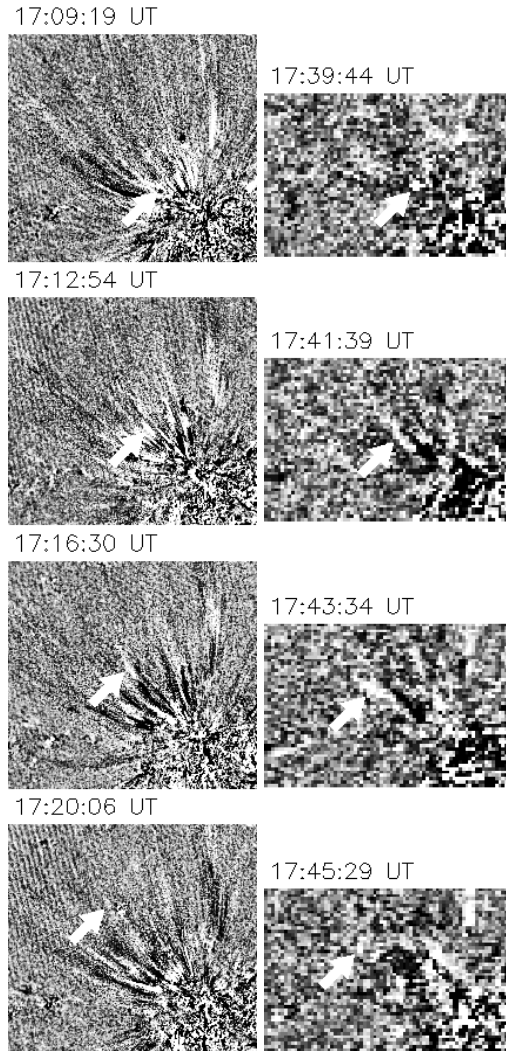


Figure 3.4: Two sequences of 4 ‘running time difference’ images are shown, extracted from TRACE 171 Å images (*left*) and from EIT 195 Å images (*right*). The difference images are created by subtracting an image taken 2m15s (for TRACE) and 1m54s (for EIT) earlier than the time mentioned in the upper left corner. We notice that there is no correspondence between the time of TRACE and EIT. White arrows indicate the propagation of a disturbance.

the slowly varying, EUV emission background. The relative variations with respect to

this background is shown. In this diagram we see propagating disturbances as bright and dark diagonal ridges. From this diagram, the apparent propagation speed v_p of each disturbance along the loop is deduced, by measuring the slope of the ridges. This is done by hand. The speed we measure is apparent because we only measure the component projected onto the plane of the sky. Since all these projected speeds are lower than the expected sound speed, it is possible that we see disturbances travelling at the sound speed. EIT (1.6 MK) measures at a higher temperature than TRACE (1 MK). The sound speed C_S can be expressed in function of temperature alone Priest (1984). This allows us to derive the following formal sound speeds:

$$\begin{aligned} C_S &= 152 \text{ T}^{1/2} \text{ m s}^{-1} (\text{T in } ^\circ \text{K}), \\ &= 152 \text{ km s}^{-1} \text{ in } 171 \text{ \AA} \text{ (TRACE)}, \end{aligned} \quad (3.1)$$

$$= 192 \text{ km s}^{-1} \text{ in } 195 \text{ \AA} \text{ (EIT)}. \quad (3.2)$$

The expected sound speed is higher for the EIT observations than for the TRACE observations (see Table 3.2.1). The apparent propagation speeds v_p which we list in the four tables, are of the order of, but never exceed this derived sound speed. Also systematically higher speeds are measured in the EIT data. This suggests that these propagating disturbances are sonic perturbations.

If we assume this, the difference between the measured speed and the sound speed is explained by the projection onto the plane of the sky. This means that we can derive from the difference between the apparent speed and the sound speed, the expected projection angle α_{exp} between the loop direction and the plane of the sky:

$$\alpha_{\text{exp}} = \arccos \left(\frac{v_p}{C_S} \right). \quad (3.3)$$

Speed measurements

For each of the four paths we have plotted the time-space diagram for TRACE and EIT, in such a way that the times correspond vertically (Fig. 3.5 to 3.8). The letters under the diagrams indicate the starting points of the ridges of which we measured the apparent speed. These letters are written in the tables in the column labeled 'I'. Some ridges show good correspondence and are assumed to trace the same feature. They are put on the same line in the tables. The tables describe the measured speeds quite in detail. We have measured the slope of each ridge several times to reduce the uncertainty on the measurement. From this we deduced v_p , the apparent speed. We measured this speed for each ridge at the bottom of the path (< 20 Mm starting from the footpoint of the loop which is not the same as the starting point of the path), at the top (> 20 Mm) and over the full length of the path. As the projection angle changes along the loop, we should measure an apparent acceleration from loop footpoint to loop top. Some ridges are not visible over the whole length and hence are only measured at the loop footpoint. The error is calculated as standard error of the mean and is defined as $\sigma_M = \sigma/\sqrt{n}$ where σ^2 is the variance and n the sample size (number of measurements per ridge). With each speed, there is a corresponding projection angle α_{exp} . This is calculated through formula 3.2.2. In the tables we list the interval $[\alpha_{\text{exp}}(v_p - \sigma_M), \alpha_{\text{exp}}(v_p + \sigma_M)]$. If this interval lies entirely in the interval $[30, 70]^\circ$, for both datasets, our measurements are not in contradiction with the slow magnetoacoustic wave interpretation.

We now briefly describe the four paths in detail. To simplify the description, we label the propagating disturbances (PDs) with the corresponding wavelength. For example B_{195} and B_{171} refer to the measurement of disturbance B respectively in the EIT (195 Å) and TRACE (171 Å) dataset.

Path 1

The loop footpoint lies at roughly 10 Mm above the starting point of path 1. In each diagram we can clearly distinguish two broad bright ridges, labelled C. They have apparent speeds of 105 km s^{-1} (171Å) and $124 \text{ (195Å) km s}^{-1}$ with an error of around 10%. The ridges are broad and diffuse, making speed determination difficult and also prone to systematic error. Assuming the speeds correspond to the respective sound speeds projected onto the plane of the sky, we can estimate the range of possible projection angles (see table) like described above. Both intervals are acceptable (i.e. lie in the range $[30,70]^\circ$ estimated from Fig. 3.3, *right*) and have a broad overlap $[45,52]^\circ$, which suggests disturbances *in the same loop*. Assuming that the ridges C in both datasets have the same physical origin, we could observe a period of around 30 min. Furthermore there are thinner ridges detectable; apart from ridge D_{171} they have roughly the same speed as the broad ridges, which again suggests propagation in the same flux tube.

Path 2

The footpoint of the loop again lies at roughly 10 Mm above the starting point of path 2. Note that the EIT frame was too small to contain the whole path. An overall clear diagonal structure is visible in both diagrams. The average (weighted) propagation speed in the TRACE frame is 95 km s^{-1} and 111 km s^{-1} in the EIT frame, inferring a projection angle of respectively $\alpha_{exp} = 51^\circ$ and $\alpha_{exp} = 55^\circ$. In the TRACE frame at height 20 Mm a periodicity of around 5 minutes starting at 17:28 UT is apparent. This is less clear in the EIT frame where only the ‘fattest’ ridges appear well. The expected projection angles of the corresponding ridges (i.e. they are on the same line in the table) in TRACE and EIT match well. In the EIT [time,space] plot two main speeds can be distinguished. Perhaps two loops at different angle are contained in the selected path. Also some ridges show signature of acceleration. This is ‘apparent’ and can be interpreted as due to the changing projection angle along the loop.

Path 3

The footpoint lies at 5 Mm of the chosen path. Clearly there are different speeds present in both diagrams. There is a good agreement of the two datasets during the half hour overlap, e.g. ridge E_{171} corresponds well to ridge D_{195} . They have the same ‘time-space’ structure, we can thus assume they have the same physical origin. Also the expected projection angles derived from it match well. The two disturbances labeled A are both broad and therefore difficult to measure. However, it seems possible that A_{195} is a periodical repetition of A_{171} . If this would be the case, we would measure a period of about 30 minutes, which we also have found in Path 1.

Path 4

The footpoint is at about 10 Mm of the starting point of the path. It is difficult to find similarities between the two diagrams. They seem to be different in nature. Only D_{171}

Path 1

TRACE					EIT				
l	$v_p (< 20 \text{ Mm})$	$v_p (> 20 \text{ Mm})$	v_p	α_{exp}	l	$v_p (< 20 \text{ Mm})$	$v_p (> 20 \text{ Mm})$	v_p	α_{exp}
	(in km s^{-1})					(in km s^{-1})			
A	71 ± 12	121 ± 13	88 ± 8	$50^\circ - 58^\circ$	-	-	-	-	-
B	74 ± 6	100 ± 25	88 ± 5	$52^\circ - 57^\circ$	-	-	-	-	-
C	114 ± 8	-	105 ± 11	$40^\circ - 52^\circ$	-	-	-	-	-
D	64 ± 11	-	75 ± 21	$50^\circ - 70^\circ$	A	125 ± 8	121 ± 21	134 ± 11	$41^\circ - 50^\circ$
E	74 ± 11	119 ± 23	94 ± 12	$46^\circ - 57^\circ$	-	-	-	-	-
F	104 ± 20	126 ± 27	119 ± 11	$31^\circ - 45^\circ$	-	-	-	-	-
	-	-	-	-	B	129 ± 29	128 ± 24	126 ± 14	$43^\circ - 54^\circ$
	-	-	-	-	C	151 ± 23	118 ± 16	124 ± 12	$45^\circ - 54^\circ$
	-	-	-	-	D	113 ± 24	-	126 ± 13	$43^\circ - 54^\circ$
	-	-	-	-	E	116 ± 10	-	124 ± 10	$45^\circ - 54^\circ$

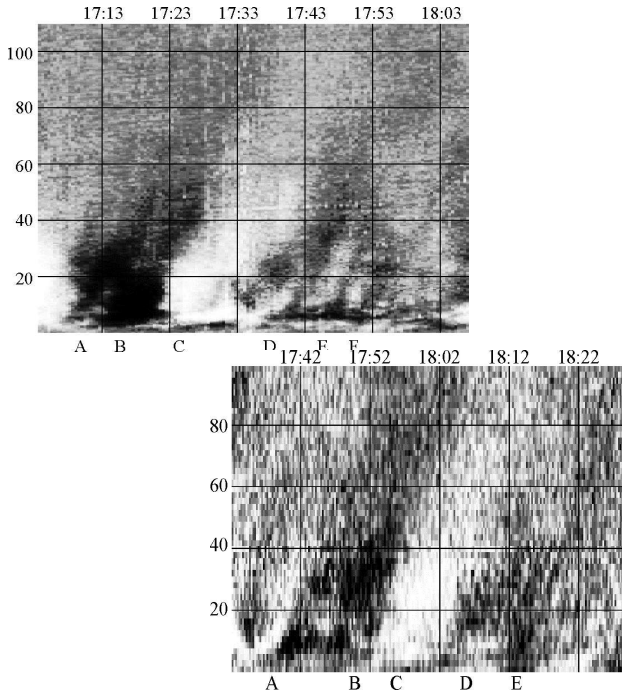


Figure 3.5: The EUV intensity along path 1 as a function of time (horizontal axis) and distance along the path (vertical axis) in the TRACE data (*upper*) and in the EIT data (*lower*) tracked in Fig. 3.2.

Path 2

TRACE					EIT				
l	$v_p (< 20 \text{ Mm})$	$v_p (> 20 \text{ Mm})$	v_p	α_{exp}	l	$v_p (< 20 \text{ Mm})$	$v_p (> 20 \text{ Mm})$	v_p	α_{exp}
	(in km s^{-1})					(in km s^{-1})			
A	-	64 ± 4	64 ± 4	$63^\circ - 67^\circ$	-	-	-	-	-
B	124 ± 19	113 ± 14	107 ± 4	$43^\circ - 47^\circ$	-	-	-	-	-
C	84 ± 5	105 ± 7	88.5 ± 3	$53^\circ - 56^\circ$	-	-	-	-	-
F	73 ± 6	96 ± 4	93 ± 15	$44^\circ - 59^\circ$	A	62 ± 7	139 ± 26	112 ± 6	$52^\circ - 57^\circ$
D	93 ± 8	111 ± 7	104 ± 5	$44^\circ - 50^\circ$	-	-	-	-	-
E	100 ± 13	115 ± 18	102 ± 4	$46^\circ - 50^\circ$	B	111 ± 14	141 ± 34	127 ± 5	$46^\circ - 51^\circ$
G	68 ± 9	97 ± 8	87 ± 5	$53^\circ - 57^\circ$	-	-	-	-	-
I	74 ± 3	-	83 ± 3	$56^\circ - 58^\circ$	C	70 ± 6	123 ± 13	97 ± 4	$58^\circ - 61^\circ$
H	81 ± 13	121 ± 18	83 ± 6	$54^\circ - 60^\circ$	-	-	-	-	-
-	-	-	-	-	D	63 ± 5	-	80 ± 14	$61^\circ - 70^\circ$
J	109 ± 8	-	117 ± 9	$34^\circ - 45^\circ$	-	-	-	-	-
-	-	-	-	-	E	112 ± 22	127 ± 21	110 ± 16	$49^\circ - 61^\circ$
-	-	-	-	-	F	100 ± 17	122 ± 36	107 ± 14	$51^\circ - 61^\circ$
-	-	-	-	-	G	101 ± 11	-	105 ± 13	$52^\circ - 61^\circ$

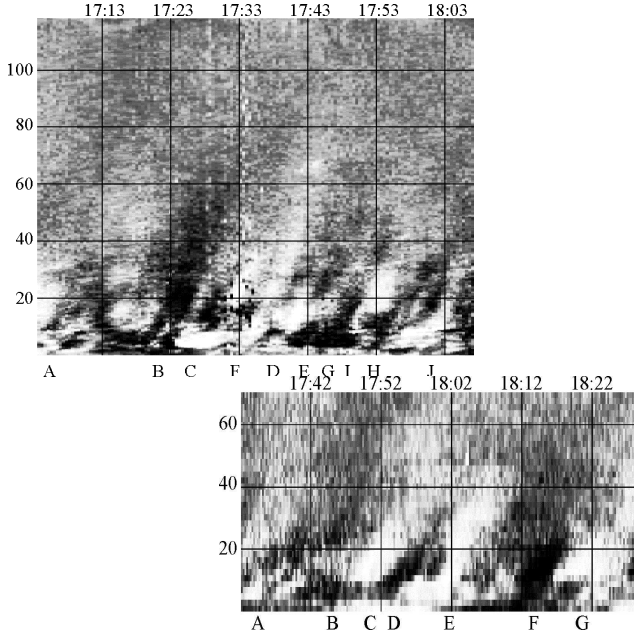


Figure 3.6: The EUV intensity along path 2 as a function of time (horizontal axis) and distance along the path (vertical axis) in the TRACE data (*upper*) and in the EIT data (*lower*) tracked in Fig. 3.2.

Path 3

TRACE					EIT				
l	$v_p (< 20 \text{ Mm})$	$v_p (> 20 \text{ Mm})$	v_p	α_{exp}	l	$v_p (< 20 \text{ Mm})$	$v_p (> 20 \text{ Mm})$	v_p	α_{exp}
	(in km s^{-1})					(in km s^{-1})			
A	54 ± 5	114 ± 14	87 ± 12	$49^\circ - 61^\circ$	-	-	-	-	-
B	58 ± 4	111 ± 10	86 ± 6	$52^\circ - 58^\circ$	-	-	-	-	-
-	-	-	-	-	A	124 ± 11	137 ± 19	124 ± 13	$44^\circ - 55^\circ$
C	92 ± 7	105 ± 5	86 ± 2	$54^\circ - 57^\circ$	B	104 ± 7	106 ± 12	106 ± 7	$54^\circ - 59^\circ$
D	89 ± 7	88 ± 7	86 ± 8	$52^\circ - 59^\circ$	C	111 ± 12	137 ± 5	112 ± 3	$53^\circ - 56^\circ$
E	83 ± 8	107 ± 13	93 ± 7	$48^\circ - 56^\circ$	D	118 ± 14	139 ± 27	126 ± 9	$45^\circ - 53^\circ$
-	-	-	-	-	E	129 ± 24	155 ± 20	124 ± 12	$45^\circ - 54^\circ$
-	-	-	-	-	F	59 ± 10	112 ± 4	79 ± 3	$64^\circ - 67^\circ$
-	-	-	-	-	G	46 ± 4	102 ± 12	70 ± 10	$65^\circ - 72^\circ$
-	-	-	-	-	H	114 ± 11	131 ± 10	120 ± 7	$48^\circ - 54^\circ$

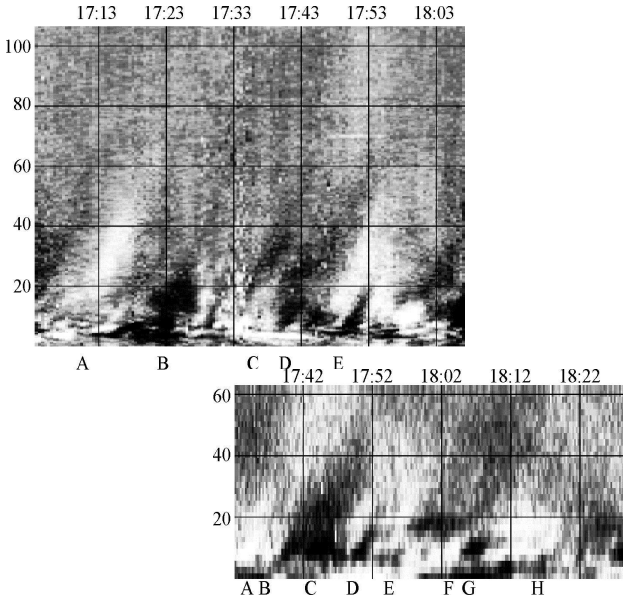


Figure 3.7: The EUV intensity along path 3 as a function of time (horizontal axis) and distance along the path (vertical axis) in the TRACE data (*upper*) and in the EIT data (*lower*) tracked in Fig. 3.2.

Path 4

TRACE					EIT				
l	$v_p (< 20 \text{ Mm})$	$v_p (> 20 \text{ Mm})$	v_p	α_{exp}	l	$v_p (< 20 \text{ Mm})$	$v_p (> 20 \text{ Mm})$	v_p	α_{exp}
	(in km s^{-1})					(in km s^{-1})			
A	78 ± 10	109 ± 9	93 ± 4	$50^\circ - 54^\circ$	-	-	-	-	-
B	96 ± 4	-	100 ± 7	$45^\circ - 52^\circ$	-	-	-	-	-
C	140 ± 24	100 ± 9	101 ± 10	$43^\circ - 53^\circ$	-	-	-	-	-
F	109 ± 9	145 ± 24	122 ± 8	$31^\circ - 42^\circ$	-	-	-	-	-
-	-	-	-	-	A	110 ± 11	165 ± 34	124 ± 12	$45^\circ - 54^\circ$
D	66 ± 3	97 ± 36	86 ± 3	$54^\circ - 57^\circ$	-	-	-	-	-
-	-	-	-	-	B	81 ± 11	101 ± 5	89 ± 5	$60^\circ - 64^\circ$
-	-	-	-	-	-	-	-	-	-
E	79 ± 3	89 ± 7	80 ± 3	$57^\circ - 60^\circ$	C	80 ± 11	105 ± 7	96 ± 12	$56^\circ - 64^\circ$
-	-	-	-	-	D	99 ± 11	106 ± 11	102 ± 10	$54^\circ - 62^\circ$
-	-	-	-	-	E	144 ± 17	131 ± 14	138 ± 14	$38^\circ - 50^\circ$
-	-	-	-	-	F	99 ± 28	124 ± 12	98 ± 17	$53^\circ - 65^\circ$

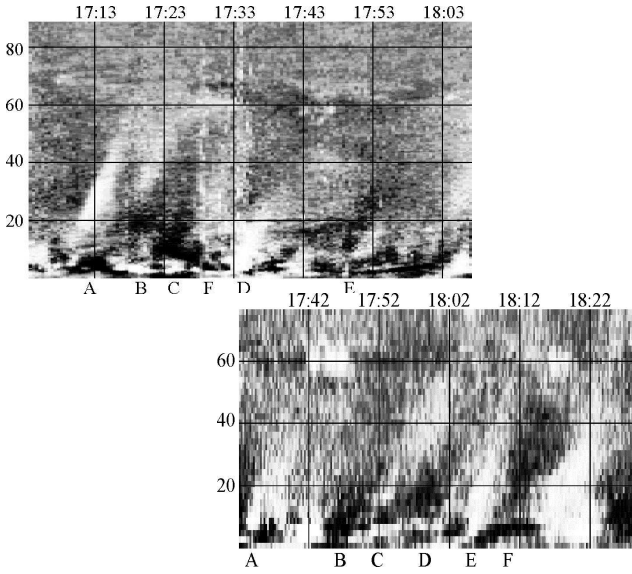


Figure 3.8: The EUV intensity along path 4 as a function of time (horizontal axis) and distance along the path (vertical axis) in the TRACE data (*upper*) and in the EIT data (*lower*) tracked in Fig. 3.2.

and A_{195} seem to correspond. While we find clearly distinct disturbances propagating in the EIT diagram, the TRACE diagram seems to contain less. After the cosmic snow at 17h28, speeds seem to be less than before. This is a trend seen in other paths as well. Maybe the nearby B flare shook the loop to a different position. A periodicity of ~ 11 min can be observed in the EIT plot.

Fig. 3.9 is an example of a horizontal cut through the time-space diagram of path 4. It shows the intensity during the whole sequence in a fixed point. From plots like these we can infer that the amplitude enhancements with respect to the background intensity are typically 8% for the 195 \AA wavelength and 12 % for the 171 \AA wavelength. An estimation of the background is obtained by measuring the intensity in that point just before

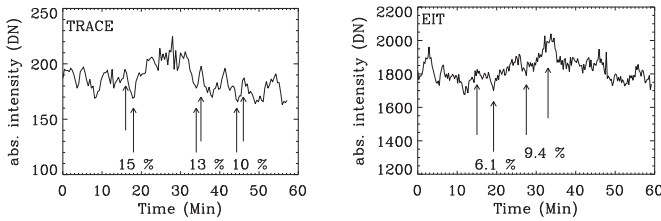


Figure 3.9: The temporal evolution near the footprint of path 4 in TRACE (*left*) and in EIT (*right*). The absolute intensity is plotted. The arrows point towards the intensities used to calculate the amplitude enhancement w.r.t. the background intensity due to a passing disturbance.

(or after) the PD passes. Fig. 3.9 can also be used to estimate the time a PD needs to cross a point, by measuring the width (in time) of a disturbance. The typical duration of a PD passing a point in the TRACE data is 169 s. This is not to be confused with the decay-time, which expresses the total life-time of a PD while traveling along the loop. As was already suggested by the time-space diagrams, the intensity variation in one point fluctuates on a timescale of about 5-6 min.

Variability

In order to quantify the variability in the loops, we define two different parameters for each pixel (x, y) :

1. $\sigma_a(x, y)$: the standard deviation with respect to the median image, expressed in DN. This quantity is a measure of the combined effect of various temporal variability components, such as slow background trends, rapid transients and oscillatory fluctuations, but also random variations due to instrumental noise.
2. $\sigma_n(x, y)$: the expected instrumental noise level also expressed in DN. The main contributions to the instrumental noise are the photon and thermal shot noise (Poisson statistics), here calculated as a function of intensity I , and the CCD readout noise:

$$\begin{aligned} \sigma_n &= \sqrt{0.25I + 2.7}, & \text{for EIT (195 \AA);} \\ &= \sqrt{0.08I + 2.8}, & \text{for TRACE (171 \AA);} \end{aligned} \quad (3.4)$$

with I the observed intensity expressed in DN. At times of cosmic snow, the noise from cosmic-ray removal dominates. This occurs mainly in the TRACE data between 17:28 UT and 17:35 UT. For a more elaborate calculation of noise see Berghmans and Clette (1999) for EIT and Aschwanden et al. (2000b) for TRACE.

The fractional variability σ_a/I is plotted in Fig. 3.10 for the 4 paths selected. We also plotted in dashed line the fractional instrumental noise σ_n/I , and as dotted line three times the fractional instrumental noise. As mentioned previously, σ_a includes various variability

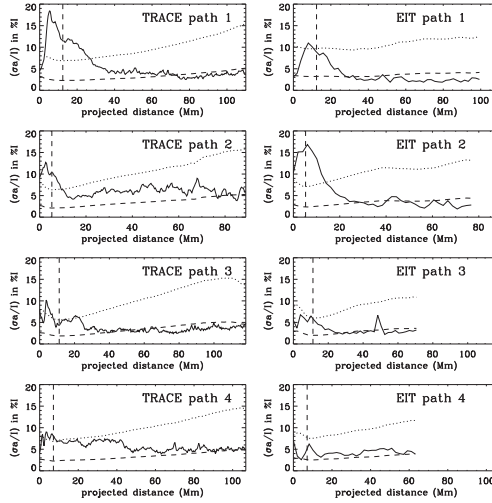


Figure 3.10: The fractional variability (σ_a/I) for the selected loops expressed in $\%I$. The vertical line indicates the position of the footpoint. The dashed line corresponds to the instrumental noise σ_n , the dotted line is three times the noise.

components. Hence it cannot be interpreted as a measure of the change in amplitude due to the disturbance only. For example, the peak present in the plots corresponding to path 3 (EIT) illustrates the contribution from a brightening to the variability. Other contributions to the variation of intensity are transverse loop oscillations. Their presence can be inferred from the difference images in Fig. 3.4. The places where field lines are sharply marked along the whole distance of the loop, indicate that the loops show a transverse motion.

3.2.3 Discussion

We find outward propagating disturbances (PDs) in virtually all loops within the opening bundle shown. We analyzed 4 different paths using [time,space] diagrams in which propagating disturbances appear as bright diagonal ridges. In all cases studied, the PDs are weak disturbances typically enhancing the loop background intensity with 8 and 12 % respectively in the 195 Å and 171 Å line. This corresponds to a change of 2.8 and 3.5 % of the background density, meaning they are only marginally detectable above the noise level. This typical amplitude is convolved with the varying throughput bandpass efficiency as a function of temperature. Although detailed temperature diagnostics are beyond the scope of the analysis presented here, it seems most likely that these disturbances are formed closely to the peak formation temperature of the instruments bandpass. Suppose that a PD at a temperature significantly deviating from this peak formation temperature was detected, with an amplitude of the order of 10 % of the background intensity. This would imply that another PD formed at the peak formation temperature, would have a significantly larger amplitude enhancement than 10 % amplitude. None of this has been

observed for many different PDs along many different loops neither in the present data set nor by other authors (e.g. De Moortel et al. 2000). The intensity perturbations measured in plumes by Deforest and Gurman (1998) amount to 10-20 % of the plumes' overall intensity. So, at least as a working hypothesis, it seems reasonable to assume that the PDs are formed at the peak formation temperature of the bandpass through which they are observed: 1.6 MK for EIT (195 Å) and 1 MK for TRACE (171 Å).

Waves or flows?

We can, in most cases, clearly distinguish a dominant direction of diagonal structure in all time-space diagrams indicating that a dominant speed of propagation is present inside the loops. However, due to bad loop-tracking or perhaps the superposition of loops, we sometimes measure more than one speed along a given path. Projected speeds found are typically 120 km s^{-1} for the 195 Å line and 85 km s^{-1} for the 171 Å line with a typical error of 10 km s^{-1} . The formal sound speeds corresponding to these temperatures are of the order of, but always higher than the observed propagation speeds: 192 km s^{-1} for EIT and 152 km s^{-1} for TRACE. By interpreting the difference between the derived sound speed and the observed propagation speed as exclusively due to a projection effect, we derive a projection angle of typically $51 \sim 56^\circ$. This is consistent with the observed range of angles $[30, 70]^\circ$ when the bundle of loops crossed the western limb a few days later (see Fig. 3.3, *right*). In addition, the apparent acceleration measured in several ridges can be explained by a larger effect of projection closer to the loop footpoints. Systematically we measure a higher speed in the hotter plasma ($\sim 1.6 \text{ MK}$) emitting at 195 Å as compared to the 'cooler' plasma ($\sim 1 \text{ MK}$) at 171 Å. These findings suggest that the intensity disturbances are caused by propagating compressional waves. The smallest speeds measured are of the order of 60 km s^{-1} for TRACE and 70 km s^{-1} for EIT. In order to match these to the sound speed the projection angle should be around $67 - 69^\circ$, which lies just in the estimated range of $[30, 70]^\circ$. As these lowest speeds principally are observed near the loop footpoints this is quite possible.

An alternative interpretation of the PDs as compared to the slow mode view is the hypothesis of plasma flows along the loop. Aschwanden et al. (2000a) concluded from the properties of extensive loop systems as observed by TRACE, that they cannot be in static equilibrium, but instead harbour continual chromospheric upflows. The flow accelerates with height and may even become supersonic. The observation we have presented here show no systematic acceleration of disturbances along the loop (besides the acceleration due to a changing projection angle). Supportive to the slow wave interpretation, Nightingale et al. (1999) find that the propagating brightenings do not show temperature increases like the EUV nano-flares do. As such they cannot be associated with the upflows of heated plasma by chromospheric evaporation like in flares.

Coronal seismology

Interpreting a propagating disturbance as a slow mode wave traveling simultaneously at different speeds, indicates temperature gradients across the selected paths. EUV loops generally outline the coronal magnetic field, primarily because heat conduction and mass transport across the field is strongly suppressed. Hence temperature and density contrasts

exist primarily across, not along the field lines. It is however difficult if not impossible to distinguish the ‘edges’ of a loop. Simultaneous observations in EUV and Soft X-rays show that coronal structures are existing at different coronal temperatures (1-2 MK versus 3-5 MK) and support the picture of loops with a hot interior and a cooler shell (e.g. Schrijver et al. 1999). Either the loops consist of concentric shells at different temperatures (e.g. Foukal 1976) or each ‘observed loop’ consists of a bundle of thin loop threads each at a different temperature (e.g. Aschwanden et al. 2000a).

High resolution images from recent missions (mainly EIT and TRACE) support the idea of loop strands, also called loop threads, which have been observed down to the limit of the TRACE instrument resolution ($\sim 1''$). The question arises if there ultimately exists an elementary strand that is homogeneous in temperature and density. In a recent Letter, Aschwanden (2005) concludes that the smallest strands with cross-section less than 2 Mm detected with TRACE represent elementary nearly isothermal loop strands. As a consequence, every loop structure with larger diameters (> 2 Mm) necessarily consists of a heterogeneous composite structure that emits in a broad temperature range. This has to be taken into account when interpreting imaging data. The loops studied in this chapter appear to be quite broad. It is thus reasonable to assume they are composed of different loop strands. This together with the big difference in spatial resolution of EIT (2.5'') and TRACE (0.5'') didn't allow us to study the correlation between the [time,space] diagrams in detail. King et al. (2003) performed a multi-wavelength wave study based on 171 Å and 195Å data, both acquired by the TRACE instrument. Their analysis shows a good correlation between the signal in the two bandpasses, which decreases systematically further away from the loop footpoint. This is in agreement with the above idea of simultaneously excited waves propagating with different speeds at different temperatures.

The driver(s)

The simultaneous occurrence of the intensity disturbances in both wavelengths suggests they are generated by the same mechanism. However, how the oscillations are triggered is still poorly understood. As in previous studies (e.g. Svestka 1994) we find evidence of quasi-periodical triggering at the loop footpoints. Our observations show waves which appear in the form of wave packets (2-8 cycles) with periods of the order of 5 min, 11 min and 30 min. Shorter periods and longer cycles are related to narrow ridges, i.e. to waves with small wavelengths. Contrary to kink oscillations which seem to be always triggered by a flare or filament eruption (Schrijver et al. 2002), this seems improbable for the slow waves. In a first inventory of this active region, based on the EIT data, there are only one strong brightening and several small brightenings detected around the footpoints of the loops here discussed (see Berghmans and Clette 1999). The widely observed time periods of 5-min and 3-min by several authors (e.g. De Moortel et al. 2002, Banerjee et al. 2002, King et al. 2003) strongly suggest that slow waves are a constant coronal phenomenon driven photospherically, rather than flare-excited transient events. 3-min periods which are found in loops rooted in sunspot umbra (De Moortel et al. 2002) coincide with the 3-min p-mode oscillations in sunspots, while 5-min periods that are more frequently observed further away from sunspots coincide with the global 5-min p-mode photospheric oscillations. In a recent paper, Marsh and Walsh (2006) present observations which confirm directly the connectivity between the 3-min umbral oscillations in

the transition region and the 3-min slow waves propagating along coronal loops.

The question then arises how p-modes could propagate through the chromosphere and transition region into the corona. Traditionally they are considered evanescent in the upper photosphere. In a numerical model De Pontieu et al. (2005) show that photospheric oscillations with periods around 5 minutes can actually propagate into the corona as long as they are guided along an *inclined* magnetic flux tube. They propose a chain of events, where leakage of photospheric oscillations into the chromosphere leads to shock formation, which drives periodical spicular flows and finally propagation of shocks into the corona. The fact that we also observe longer periods simultaneously in the same loop could indicate the presence of 2nd harmonics due to non-linear steepening.

Slow waves contributing to coronal heating?

At the end of the 40ies, it was suggested that the corona could be heated by sound waves driven by the p-mode oscillations in the convection zone. While traveling upwards, these waves steepen into shocks dissipating their energy at the shock front. However, this option was ruled out when Athay and White (1978) showed with their analysis of UV spectroscopic data from OSO-8 (launched in June 1975) that the acoustic wave flux is 2-3 orders of magnitude below the coronal heating requirement. They concluded that ‘the low chromosphere may be still heated by short period sound waves but that a different mechanism heats the upper chromosphere, transition region, and corona.’ That this different mechanism should be magnetic in origin was proposed, after the discovery that the corona had much higher concentrations of magnetic field (kG) than was generally accepted. The most popular mechanisms for coronal heating are dissipation of magnetic energy in ‘alternating currents’ (AC) meaning heating by Alfvén waves, and in ‘direct current’ (DC) i.e. by reconnection. At the beginning of the new millennium, after the discovery of magnetoacoustic waves in coronal loops, it is again questioned if sound waves can significantly contribute to coronal heating. In any case, the energy flux of the magnetoacoustic waves was estimated to be of the order of 0.35 W/m^2 (De Moortel et al. 2000), which is far below the energy required for coronal heating.

The question remains why these waves disappear so quickly. They hardly reach the loop apex. Many mechanisms have been proposed. Even with the knowledge that it will not solve the long-standing coronal heating problem, it is still an interesting question. Nakariakov et al. (1999) proposed viscous dissipation, but that would require viscosity coefficients much larger than generally accepted. Later papers disagree with this conclusion and suggest alternative mechanisms (e.g. Goossens et al. 2002).

3.3 Conclusion and future outlook

Overlapping multi-wavelength observations of longer duration and improved data-analysis techniques are desirable. The future Atmospheric Imaging Assembly (AIA) onboard SDO (Solar Dynamics Observatory) and the EUV package onboard STEREO are in this respect very promising. On AIA seven EUV channels will image simultaneously the different layers of the solar atmosphere with high temporal (10 s) and spatial (0.6" pixel) resolution. Additionally, new image processing techniques (e.g. Gissot and Hochedez 2007)

will make it possible to track the loop while moving e.g. due to spatial oscillations. Since the resolution of the loop threads are predicted to be below the TRACE resolution, higher angular resolution will be necessary to study in detail the propagation of waves along loop threads. Also their high cadence is needed for the observation of slow waves.

In most of the observed cases the spectroscopic information is missed, leading to the ambiguity of interpretation in terms of mass flows or propagating compressional waves. To solve this ambiguity would be of primary importance in understanding the nature of these waves and loop. Many papers have proven the success and necessity of Joint Operation Programmes (JOPs), such as are currently organised for SOHO and TRACE. We believe thus that these have to be an ongoing project linking data from future missions. The high spatial resolution of Solar Orbiter will allow the identification and study of intensity fluctuations over the fine structure of loops. The spectroscopic information through the detection of Doppler shift, in combination with imaging data, will allow untangling wave propagation from mass flow (Eriksen and Maltby 1967). Besides it will also reduce the uncertainties introduced by the projection effects. At present mostly only one component of the propagation speed is reported for these waves (only the plane of sky speed). This introduces a large uncertainty on the speed estimation. In the early phase of the mission, also STEREO will enable us to eliminate projection effects by using multiple viewpoints. Secondly it would also allow us to test the hypothesis of De Pontieu et al. (2004) that the period of oscillation is depending on the inclination angle of the loop (i.e. their deviation from the vertical).

Part II

Coronal mass ejections

Chapter 4

The automated detection and characterization of coronal mass ejections in coronagraphic data

This chapter deals with the problem of detection of coronal mass ejections (CMEs) in coronagraphic white light data. A CME is observationally defined as a new bright feature moving radially outward. To test the validity of the observational CME definition we have translated this definition in parameters which are measurable in LASCO data (see Chapter 1). This resulted in a software package named CACTus (Computer Aided CME Tracking). The aim of the software is to detect the appearance of a CME in a sequence of white light images acquired by LASCO. During the course of the thesis CACTus has been improved in both the preprocessing and the detection module. The CACTus software is now incorporated in the daily Space Weather services of the Solar Influences Data Analysis Center (SIDC - Royal Observatory of Belgium) running in near-real time. We describe the inner machinery of the software and illustrate its performance on a dataset of 6 days comparing the CACTus parameters with manual detection. This chapter contains material published in Robbrecht and Berghmans (2004).

4.1 Introduction to coronal mass ejections

Coronal mass ejections (CMEs) are episodic expulsions of mass and magnetic field from the solar corona into the interplanetary medium. A classical CME carries away some 10^{15} g of coronal mass and can liberate energies of $10^{23} - 10^{25}$ J (Howard et al. 1985, Vourlidas et al. 2002). Since their discovery in the seventies in coronagraphic observations on the OSO-7 satellite (Tousey 1973) and the Skylab mission (Gosling et al. 1974) coronal mass ejections have been subject to numerous studies. The LASCO era (Brueckner et al. 1995) introduced an explosion of literature on coronal mass ejections. Recent reviews on their observational properties, initiation, physical nature, simulations and their relation to the heliosphere can be found in Howard (2006), Gopalswamy (2004b), Kahler (2006), Moore and Sterling (2006), Forbes (2000) and Low (2001) and references therein. CMEs are the most energetic eruptions on the Sun. They can accelerate energetic particles (SEP, Gosling et al. 1990, von Rosenvinge and Cane 2006) and are the primary cause of major disturbances in the Earth's magnetic field (termed 'geomagnetic storm') which highly affect radio HF communication throughout the polar region (no other communication is

possible above 82 degrees latitude, e.g. for polar flights), the reliability of power systems (voltage control problems, blackout or collapse of grid, damage to transformers), induce currents on pipelines and cause spacecraft surface charging. Hence, to guarantee the reliability of many technologically dependent systems and activities, timely and accurate monitoring and forecasting of these energetic space weather events - CMEs - have become indispensable.

4.1.1 CME observation and dynamics

The majority of our knowledge on CMEs comes from coronagraphic observations. Over the past 10 years CMEs have been successfully detected by eye in LASCO data, available in near-real time. In a sequence of coronagraphic white light images, a CME appears as a bright bubble of plasma moving away from the occulter into interplanetary space. A 'typical' CME travels at 300-400 km/s, having an angular width of 45° around the occulter and erupting from near the equator (Yashiro et al. 2004). The excess brightness is photospheric light reflected by electrons, and thus represents mass ejected from below the occulter into the heliosphere. The prototypical CME was first observed on 18 Aug 1980 (Illing and Hundhausen 1983). In this event the three part structure was identified in which the front is followed by a cavity of reduced density and a bright core. The bright core is likely to be the prominence material. Although a large fraction of CMEs shows this three part structure, many different structures have been observed. The question whether in reality this actually corresponds to different types of ejection is not resolved yet. To shed light on this question, analysis of the physical conditions of these different types observed in white light is needed, mainly by using spectral observations (Kahler 2006). Cremades and Bothmer (2004) have studied the relationship between white light topology and source region for a set of 'structured' CMEs. They deduced a generic scheme of 3D configuration, according to which the projected white light topology depends primarily on the heliographic latitude and orientation of the source region's underlying neutral line. The cylindrical geometry found in the structured CMEs implies that they are organized along an axial direction.

The next mission with a coronagraph is the NASA STEREO mission (Solar Terrestrial Relations Observatory), launched on 26 Oct. 2006. The coronagraphs onboard the dual STEREO spacecraft (one flying ahead and one behind the earth at the same radial distance from the Sun) are hoped to shed light on the 3D nature of CMEs, their initiation and propagation. This spacecraft will take simultaneously pictures from two viewpoints as if it were two eyes observing a CME. By combining these images, the 3D structure of a CME can be studied. This combining is not an easy task, since the corona is optically thin, and the two separate images are each a result of integration of intensity along their respective lines of sight. The spacecraft will drift away from the Earth at an average rate of about 22° per year resulting in varying science objectives. At the end of the two year nominal mission the spacecraft will be 90° apart. In this orientation the coronagraphs (COR1, COR2) from one spacecraft will observe the solar corona above the EUV disk observed by the EUV imager (EUVI) on the other spacecraft.

CMEs have strong associations with flares and eruptive prominences at the 50% and 75% levels respectively, with many CMEs associated with both (Munro et al. 1979). CMEs originating from active regions and accompanied by flares tend to have speeds

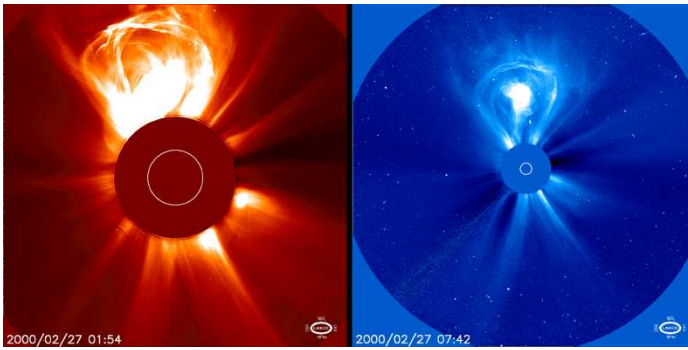


Figure 4.1: Example of a ‘lightbulb’ CME. It shows the typical three-part structure consisting of a bright leading edge, dark void and bright core. The event was observed by LASCO C2 (*left*) and C3 (*right*) on 27 Feb 2000. The two images have their background subtracted. The red and the blue color is artificial. Although the CME travels towards the north, inspection of EIT images shows that the source region was a filament situated at the limb in the north east quadrant. It is thus an illustration of non-radial CME propagation.

above the median speed in the lower corona and are seen to decelerate throughout the C2 FOV. CMEs originating away from active regions and accompanied by prominence eruptions are initially slower and show gradual accelerations. These observations lead to the hypothesis of the existence of two dynamical types of coronal mass ejections (MacQueen and Fisher 1983, Moon et al. 2002). However the above mentioned association is arguable; all CMEs together exhibit speed-height profiles forming a continuous spectrum between these two characteristic types and other theories are proposed (e.g. Low and Zhang 2002). The fact that a significant number of CMEs initially travel below the escape velocity of the corona suggests a continuous driving process.

This chapter focuses on the appearance of CMEs in coronagraphic white light data, where they first have been observed. Nevertheless, these ejections of mass are linked to a variety of phenomena, which can be detected remotely at many wavelengths across the electromagnetic spectrum (e.g. X-ray, EUV, $H\alpha$ and radio). Also the plasma, particle and magnetic properties of ejected material can be measured in situ in the heliosphere. In EUV observations of the lower corona (on disk), a CME can appear as a ‘dimming’, accompanied by an EIT wave (Thompson et al. 1998, Biesecker and Thompson 2002, Zhukov and Auchère 2004). A dimming resembles a transient coronal hole and is interpreted as an evacuation of mass around the eruption center. Although EIT waves and dimmings are strongly associated with CMEs, a one-to-one relationship has not been proven. ‘Post-eruption arcades’ (also called ‘post-flare-loops’) seen in EUV (e.g. Tripathi et al. 2004) are also a signature of CME occurrence. On their turn these bright arcades cause enhanced X-ray radiation recorded e.g. by the GOES satellite as a long duration ‘flare’ in time series. Other remote sensing signatures of CMEs are sudden disappearances of filaments/prominences, but a disappearance doesn’t necessarily infer the ejection of mass into space. There is the possibility that a prominence disappears in the $H\alpha$ channel because it is heated temporarily, but once cooled it reappears (Mouradian et al. 1995). The avail-

able automated detection schemes of CME signatures in the lower corona are reviewed in chapter 6.

4.1.2 Observational limitations

There are several limitations to coronagraphic CME observations. First, a CME can be missed, simply due to a data gap lasting for several hours/days. Being located at the L1 point, the LASCO daily operations can be interrupted due to spacecraft activities or anomalies. Alternatively a CME can be too fast to be captured at nominal cadence. For LASCO, this risk is quasi non-existing, since it has a large combined C2/C3 FOV and the image cadence of C2 and C3 have well been chosen to observe even the fastest CMEs. For example, a fast CME traveling at 2000 km/s needs about 23 minutes (1 image) to cross the C2 FOV and 2 hours (4 images) for the C3 FOV.

Secondly, the nature of the electron Thomson scattering (Billing 1966) which forms the image of the corona, puts a more severe constraint on the observability of CMEs. The scattering is maximal in the direction perpendicular to the direction of the electromagnetic radiation, which is radially away from the Sun. Therefore, CMEs erupting from the limb (90 degrees longitude) are brightest and CMEs towards or away from the observer appear faint or are even invisible. An important subset of these CMEs are halo CMEs (Howard et al. 1982), which appear as a gradually expanding, sun-centered disk of excess brightness, giving its typical halo shape. As a rule of thumb, all CMEs erupting within an angle of 60° of the plane of the sky are regarded as visible. Additional to the aforementioned reasons, narrow CMEs towards the observer would be missed, even if the electrons would scatter 100% of the incoming light, simply because their angular extent would not exceed the size of the occulting disk.

4.1.3 Conceptual models of CME initiation

The possible initiation mechanisms of CMEs are still a matter of discussion, they have been reviewed by Forbes (2000), Klimchuk (2001), Low (2001) and Linker et al. (2003). Klimchuk (2001) distinguished 5 different classes of models and described them in terms of simple mechanical analogues involving springs, ropes and weights. According to their energy source he organized them in two groups labeled ‘storage and release models’ and ‘directly driven models’. *Storage* refers to the slow buildup of magnetic free energy from the gradual stressing of the field by mass accumulation (mass loading) or by footpoint motions (tether release and tether straining). *Release* refers to the highly dynamic phase when rapid energy conversion and eruption take place. The second category of CME models behaves entirely different. They bypass the intermediate state and go directly to the eruption without slow energy buildup. It includes the thermal blast model and the dynamo model.

The **thermal blast model** (e.g. Dryer 1982, Wu et al. 1982) supposes a sudden release of thermal energy conferred by a flare which literally blows open the corona. This was the first explanation given for CMEs and was inspired by the fact that many CMEs occur in conjunction with solar flares. In the **dynamo models** (e.g. Chen 1989) the ejection is directly driven by a fast injection of magnetic energy (about 10^{25} J), e.g. by the fast displacement of footpoints. Due to observational contradictions regarding the photospheric

magnetic field and the small number (and timing) of large flares these two models seem less probable, at least for the majority of cases.

Most recent theoretical work is based on the concept of storage and release. **Mass loading models** suppose a meta-stable field such that mass loading can buildup sufficient free energy, e.g. in the form of a growing prominence before the system destressed (e.g. Low and Zhang 2002). A crucial criterion is the mass of the prominence. The mechanical analogue is a string compressed by heavy weight. If the weight is shifted to the side, the string uncoils and part of the stored energy is catapulted upwards. Mass plays no significant role in the two other models in this category. They assume magnetic energy buildup by stressing the field lines, responsible for the downward-directed force of magnetic tension. The **tether release models** (e.g. van Ballegoijen and Martens 1989) assume that the field lines, sometimes called tethers, are released one after the other e.g. by flux cancelation. The tension on the remaining tethers increases and eventually causes them to break. **Tether straining models** differ from the previous type because the strain on all the arcades increases gradually until they break. A popular model of this type is the magnetic breakout model (Antiochos et al. 1999) which involves a quadrupolar structure, opened up at the X-point by magnetic reconnection. A similar breakout effect can be achieved in a bipolar magnetic field with the normal/inverse prominence configuration described by Low and Zhang (2002).

4.2 Motivation for automated detection

As is visible in Fig. 4.2 a CME is not always a *discrete* bright structure with its edges well defined and thus subject to interpretation. It is doubtful whether visual CME detection is stable over a solar cycle, as an operator gains experience or personnel is replaced. There is probably not much confusion for big, well-structured events, but small and/or weak events might be arbitrarily detected or not. An additional constraint on human detection is manpower. Visual detection of CMEs in the flood of incoming new data is a labor intensive task. Future missions like STEREO (launched Oct. 26), SOLAR-B (launched Sept. 2006) and SDO (launch in 2008) will overwhelm us with data, with higher space-time resolutions than ever. E.g. EUV instruments (AIA) onboard the Solar Dynamics Observatory (SDO) will produce 1 Tb of data per day! Although there will be no coronagraph on SDO, the challenge is equal for detecting all other solar features and events. Data management and feature cataloging necessarily become an integral part of observational solar physics research.

4.3 Detailed description of the method

Early versions of the CACTus package were discussed in Berghmans et al. (2002) and Berghmans (2002). The improved version is described in Robbrecht and Berghmans (2004). The preprocessing module merges the C2 and C3 images, cleans, rebins and reformats them with every step optimized for improving the CME contrast. This merging of C2 and C3 images is a delicate exercise in which attention should be drawn to the different spatial and temporal resolutions. We next describe the CME extraction from the

manipulated dataset. This is done in two steps: (1) detection of bright features moving radially outward and (2) clustering detections into CMEs. Unique for our detection method is that we use the condition ‘moving radially outward’ as part of the detection criterion. The fact that CMEs can occur close to each other in time or space makes it a challenge to correctly cluster different detections into several events. To test the performance of CACTus, we have applied it on a quicklook LASCO data-set of 6 days (mid November 2003) and compared its output with the list of CMEs manually detected by the LASCO operators.

4.3.1 Data

The images obtained by the LASCO C2 and C3 coronagraphs are the starting point for our CME detection scheme. These images show the solar corona in broadband white light. It would be a misunderstanding to think that the brightness we see resembles true emission of light by the coronal gas. Although this spectral line emission due to highly ionized atoms exists, the so-called E-corona only contributes a very small portion to the white light corona. Illustrated in Fig. 4.2 the main contributors are the K- (Kontinuerlich) and F- (Fraunhofer) corona. They arise out of photospheric light that is Thomson scattered by the free electrons (K) and reflected by dust particles (F)¹ in the corona. The dust particles originate from comets and asteroids and are spiralling into the inner solar system, concentrated in the ecliptic plane. The F-corona is thus actually unrelated to the corona and can be compared to the beam of light falling into the window of a dusty room. The K-corona, at the other hand, depends on the presence of free electrons in the corona and its intensity is directly related to the electron density. It is thus the K-corona we are interested in, and more specifically the portion that brightens up when a CME passes through the image. The K-corona dominates up to a height of about $2 R_{\odot}$, where the density is around $10^{-12} \text{ kg m}^{-3}$, beyond this distance the F-corona is brightest. Because of the nature of Thomson scattering the K-corona is highly polarized, contrary to the F-corona.

In order to see any coronal dynamics in a LASCO white light movie the F-corona has to be removed from the original images. This problem is referred to as the ‘separation of the coronas’.

4.3.2 Preprocessing

The default processing of LASCO images consists of removing a background light model, computed over two weeks of data. It consists of instrumental stray light as well as coronal light (including the full F-corona) and contains about 99% (!) of the light received by the CCD. This default processing allows observing CMEs by eye very well, but it is not optimized for *automated* CME detection. The main reason is that bright features moving on timescales less than two weeks, typically streamers, are kept in the image. To overcome this problem, we take running difference images in which each image is subtracted from the next image. By doing so, we can enhance the image contrast well enough for CME detection. Moreover, all relatively stable bright features are removed from the image.

¹This emission is called F-corona because it shows the same dark absorption lines that Fraunhofer found in the on-disk spectrum.

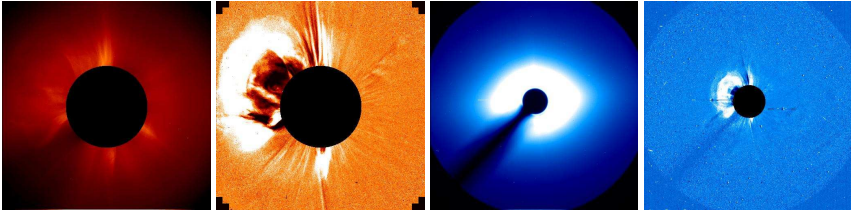


Figure 4.2: *Red*: Example of a raw C2 image (left) and a contrast enhanced image (right) which was produced by taking the relative running difference. A large CME erupting from the east becomes visible (solar east is on the left). Note that since we didn't clean the images in beforehand, stars and cosmic rays show up bright/dark in the running difference image. *Blue*: Example of a raw C3 image (left) and a contrast enhanced image (right) as for the C2 image. The bright egg-shaped area resembles the F-corona which is completely removed in the right image. Also the pylon, holding the occulter at the entrance of the instrument, is clearly visible in the south-east of the raw blue image.

The images are relatively large with a spatial resolution far beyond what is needed for CME detection. A typical CME is only a relatively weak variation in intensity and only visible in a few subsequent images. Straight application of image recognition techniques on the usual 1024×1024 images would therefore result in a very large computational overhead.

Below we describe the preprocessing steps undertaken to encompass the above mentioned problems. In addition, the data is transformed into a different format, on which the detection algorithm can be applied.

- For automated detection, it is important to first clean the images from all bright features (cosmic rays, stars and planets) that otherwise could trigger detections. This is done in the original images by applying a median filter. For the running difference to make sense, we perform an exposure time normalization. A C2 image is typically exposed for 25 seconds and a C3 image for 19 seconds.
- A polar transformation is applied to each image: the $[x, y]$ FOV becomes a $[\theta, r]$ FOV, with θ the poloidal angle around the Sun and r the radial distance measured from the limb. By choosing the r -range appropriately, the dark occulter and corner regions are easily avoided. While transforming, we also rebin, from 1024×1024 pixels for the $[x, y]$ FOV to 180×34 pixels for the C2 $[\theta, r]$ FOV and to 180×197 pixels for the C3 $[\theta, r]$ FOV. Preliminary studies (Jeanquart 2003) showed that this lower spatial resolution is still sufficient to distinguish CMEs. This rebinning speeds up the program and increases the signal-to-noise ratio significantly, especially far away from the disc, as the area $r\Delta\theta\Delta r$ of the 'footprint' of a $[\theta, r]$ -pixel in $[x, y]$ -images grows linearly with r . By doing so, we limit the angular resolution to 2° , which is far below the measurement uncertainty of the CACTus method relative to manual detection, as illustrated in Fig.4.8. The relative uncertainty between the two methods is partly due to the ambiguity of the CME definition which is discussed in chapter 5.

- For each $[\theta, r]$ pixel a CME passage results in a short-lived positive deviation from the average. The contrast of a CME is frequently described in terms of a $\Delta B/B_{\text{bg}}$ ratio, defined as the maximum change in coronal brightness ΔB compared to the background corona B_{bg} (St. Cyr et al. 2000). Sime and Hundhausen (1987) noted that the $\Delta B/B_{\text{bg}}$ ratio ranged from a few percent for the faintest CMEs up to unity for the brightest events. Instead of using a background image, we take a running difference image and scale this to the preceding image (pixel-by-pixel). This ratio is taken to further enhance the contrast towards the edges of the field of view (FOV). This contrast enhancement technique is illustrated in Fig.4.2. By doing so, we can enhance the image contrast well enough for CME detection. Moreover, all relatively stable bright features are removed from the image. The final intensity B'_t of a pixel is thus

$$B'_t = \frac{\Delta B}{B_{t-1}},$$

where ΔB in fact is $\delta B/\delta t$, since the images are not necessarily equidistant in time. This is the relative deviation of the original intensity B_t of the pixel as a function of time.

- The $[\theta, r]$ ‘ratio’ images originating from C2 and C3 are combined in a single composite image by re-scaling and matching the different spatial and temporal resolution of the two coronagraphs. They are chronologically ordered one image after the other in a 3D cube (with time being the third independent variable). No interpolation in the time direction is performed. The unequal temporal spacing is taken into account when detecting the CMEs. Since the LASCO C2 FOV is much smaller than that of C3, this step essentially comes down to adding a small C2 strip at the bottom of the $[\theta, r]$ C3 images. We then obtain a series of 180×215 pixel images.

The output of this procedure is a $[\theta, r, t]$ datacube that is much smaller than the total of the original input data, and in which most of the non-CME signal is removed or strongly attenuated.

The aims of CACTus are (1) detect CME occurrence (2) measure its radial direction and angular extent and (3) estimate the speed of CME propagation. The preprocessing stage influences the CACTus results only for the first two aims; the uncertainty on speed is mostly a matter of image cadence. The detection of CME occurrence, which is a boolean value (hit/miss), should become more reliable by the contrast enhancement and signal-to-noise ratio improvement. The error introduced by the reduction in angular resolution propagates into an error in the angular output parameters of CACTus, which is estimated to be small.

4.3.3 Detection

In what follows we have implemented a synthesis of existing CME definitions, as how they are observed in coronagraphic white light images (e.g. Hundhausen et al. 1984, Munro et al. 1979, Schwenn 1995). A CME is defined as the appearance of a ‘new, discrete, bright, white-light feature in the coronagraph field-of-view moving radially outward.’ The discussion whether this is also a sufficient condition is postponed to sec-

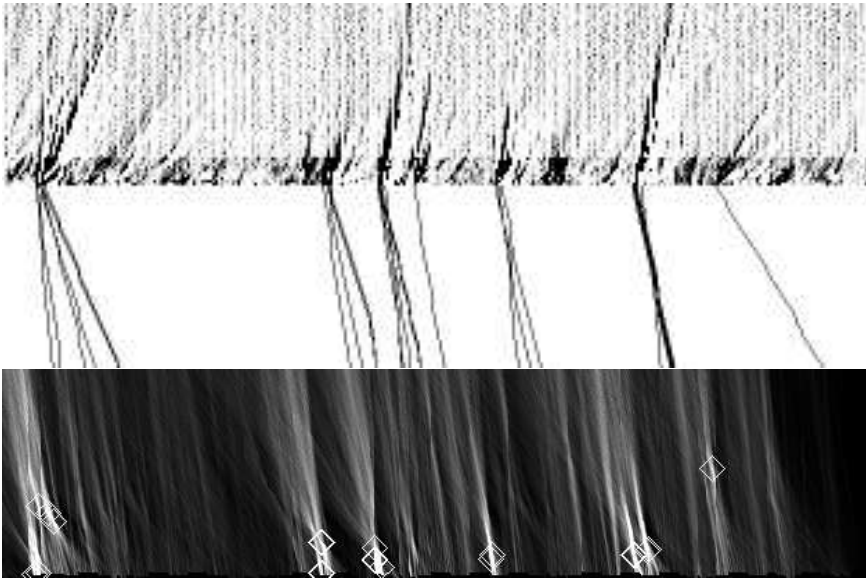


Figure 4.3: Illustration of the CACTus detection mechanism. The first 20 iterations are shown. *Top*: Example of a [time,height] slice through the datacube at a given angle. Time runs horizontally from 9 to 14 November 2003. The vertical range corresponds to the combined C2/C3 field of view (FOV). *Bottom*: Hough transform of the [time,height] diagram. Time runs horizontally (same scale as above). The vertical axis represents speed decreasing from down to up. Each diamond indicates a detection and can be transformed back into a line. *Middle*: The corresponding ridges are shown upside down. The inclination angle of the ridges corresponds to the propagation velocity.

tion 6.6. Utilizing this definition implies that we have not assumed any physical model while detecting CMEs.

CMEs are very variable in appearance, they are often too weak to identify their extension and they might erroneously be merged with one another. Instead of trying to detect CMEs in each polar transformed image we use the characteristic ‘radially moving outward’ as a necessary condition for detection. Detecting radial motion is possible in $[t, r]$ slices (Fig. 4.3, top) which are obtained by slicing the $[\theta, r, t]$ data cube along the θ -direction. If a $[t, r]$ slice at an angle θ cuts through a CME, an inclined bright ridge is seen in the $[t, r]$ slice. Detecting CMEs in $[t, r]$ slices was first introduced by Sheeley et al. (1999). Thanks to the preprocessing module however, our $[t, r]$ slices, and the CME ridges in them, have a much better contrast and contain less noise. Working with $[t, r]$ slices has the advantage that all CMEs have the same appearance (inclined ridges), that even weak CMEs show up with a clear signature and that the detection of inclined ridges naturally satisfies the above specified necessary condition of radially outward moving features. Finally, as a bonus, a radial speed-profile can be determined for each CME by measuring the inclination angle of all ridges contained in the CME.

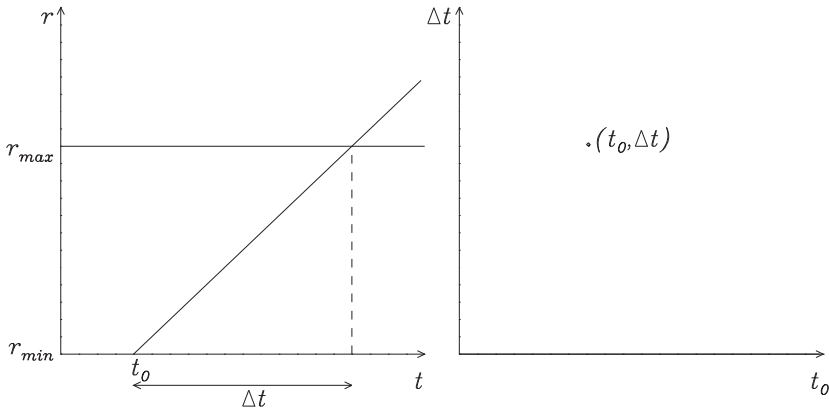


Figure 4.4: Illustration of the modified Hough transform. Left: Each line can be characterized by t_0 and Δt . Right: $(t_0, \Delta t)$ is its corresponding point in the Hough space. r_{min} and r_{max} correspond to the edges of the FOV in the radial direction. Δt is the time the CME spends in the FOV.

A well known technique for detecting straight lines in noisy data is the Hough transform (see Jahne 2005). The same transform has been used e.g. by Llebaria and Lamy (1999) to detect polar plumes in LASCO/C2 data. Every straight line in the $[t, r]$ space as drawn in Fig.4.4 can be parameterized by two variables t_0 and Δt , t_0 being the coordinate of the intersection point with the time-axis and Δt being the distance along the t -axis, corresponding to a distance $r_{max} - r_{min}$ in the r -direction. The equation describing the line is then

$$r = \frac{r_{max} - r_{min}}{\Delta t} (t - t_0) + r_{min}.$$

The modified Hough transform of this line is a point in the $[t_0, \Delta t]$ plane (the so-called accumulator space) with the intensity being the integral of the intensity along the corresponding line in the original image. Then local maxima in the $[t_0, \Delta t]$ space give the different straight lines present in the original image.

The drawback of the Hough transform method for line detection is the high computational effort. For every point $t = t_0$ in the image, we must compute a vertical line in the parameter space and increment each point in the Hough space through which the line passes. By limiting the parametrization to lines with a slope corresponding to an acceptable CME velocity, we can reduce the computation time heavily. This can be understood by interpreting the vertical dimension of the Hough space (Δt) as the width of an imaginary time window sliding over the [time, height] plot (Fig. 4.3, top) in the horizontal direction. For example a slow CME of 100 km/s needs about 100 images to cross the combined C2-C3 field of view, while a CME of only 50 km/s needs approximately twice that amount (200 images). Allowing the detection of very slow CMEs, would heavily slow down the algorithm. The maximal speed is limited for another reason. The leading edge of a fast CME with speed 2100 km/s is only visible in 1 C2 image and 4 C3 images.

Faster CMEs might thus be missed by the C2 instrument. Moreover, with a nominal cadence of 3 C2 images and 2 C3 images per hour, the precision on velocity measurement decreases dramatically for these high speeds. One image more or less has a significant influence on speed measurement for fast CMEs. For these reasons we have set the minimal CME velocity on 100 km/s and the maximal speed on 2100 km/s. Using the CACTus catalog, described in the next chapter, we can confirm that this upper speed limit did not exclude any of the 27 CMEs which were listed by CDAW with a speed above 2100 km/s; 26 of these were halo or partial halo.

We make a modified Hough transform of every $[t, r]$ slice. During this step we take into account the unequal spacing in time of the images, such that the ridge would look like a straight line if the images were equidistant in time. From Hough transformed space, we extract most significant signals as illustrated in Fig. 4.3 (*bottom*), which after inversion correspond to the bright ridges (Fig. 4.3, *middle*). Each ridge R in a $[t, r]$ slice at an angle θ_R is characterized by its onset time t_R , its linear velocity v_R ($\sim \frac{1}{\Delta t}$) and its intensity I_R . We can now build up a datacube $[v, \theta, t]$ by setting for each detected ridge $[v_R, \theta_R, t_R] = I_R$. We limit the detections to peaks in the Hough space with an intensity I_R above a fixed threshold.

Since a CME is a large scale structure, the onset time and velocity will differ only slightly from angle to angle. This means that a CME is represented in the $[v, \theta, t]$ datacube as a dense cluster of data points. The problem of detecting CMEs has thus been reduced to identifying clusters in a 3D scatter plot. We simply integrate the $[v, \theta, t]$ cube along the v -direction and identify the location of clusters in the resulting $[\theta, t]$ CME overview map as the time of occurrence and angular span of CMEs. Only clusters of points wider than 8° in the θ dimension are allowed. The result of this is shown in Fig. 4.5. The colors are randomly chosen and are used to distinguish between different CMEs. The length of the ‘blob’ in the vertical direction indicates how long the outflow of the CME takes. Fig. 4.6 is an illustration of how the CACTus output looks like. A sequence of 3 running difference $[\theta, r]$ -images is shown (top panel), containing 2 CMEs on 11 November 2003. The bottom panel shows the same information with the CACTus CME detections superimposed on it in green (CME nr 22) and in blue (CME nr 23).

4.4 Validation of the method

We applied the above scheme to real-time data from a period from 9 to 14 November 2003. This period just follows the period of the giant X17 and X25 flares on 28 October and 4 November. The dataset is limited to 6 days for practical reasons. We compared our results with the CDAW LASCO CME CATALOG (Yashiro et al. 2004) available online (<http://lasco-www.nrl.navy.mil/cmelist.html>). This catalog contains CMEs which have been identified manually in the LASCO C2/C3 data. From this list we extract for each CME the time of appearance in the inner C2 coronagraph, the central position angle (PA) of the CME, the angular width and the CME velocity. The velocity is measured by clicking the leading edge of the CME along the direction of the fastest moving feature. This direction does not necessarily coincide with the PA. The CDAW catalog lists 16 CMEs in the period considered.

The time series of November 2003 consists of 372 C2 and 246 C3 images. The median

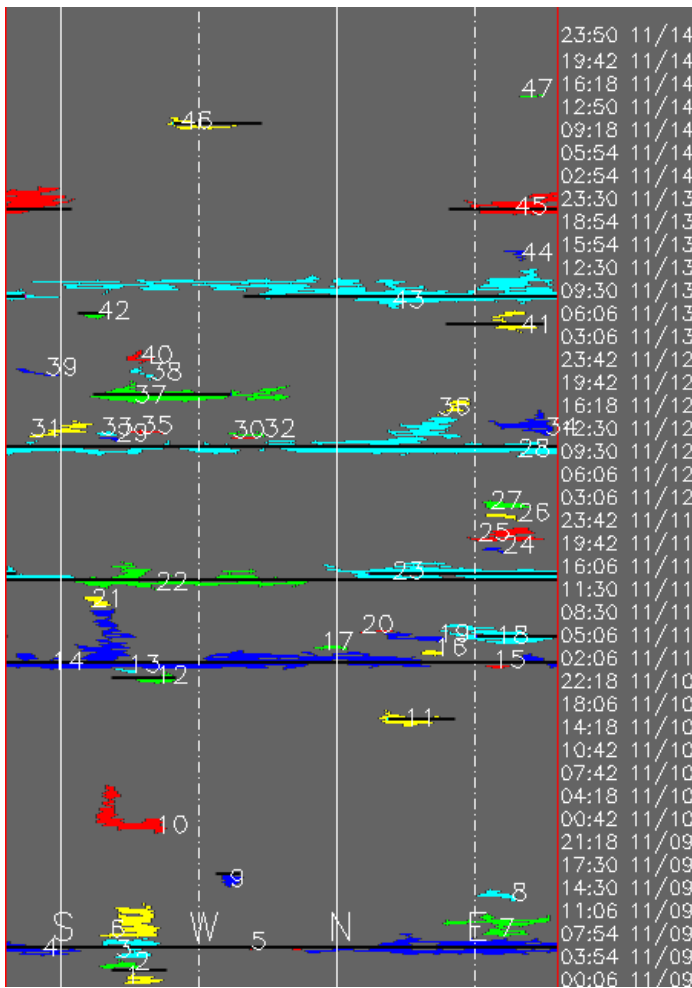


Figure 4.5: CME overview map comparing the CDAW CMEs (black lines) and those found by CACTus (colored shapes). The colors have no meaning by themselves but are used to distinguish between different CMEs. Time runs vertically from 9 to 14 November 2003. The poloidal angle runs counterclockwise from left (near the pylon holding the occulter) to right. The CDAW time of appearance corresponds to the bottom of the black lines. The thickness of the lines is arbitrarily set to 30 minutes.

C2-cadence is 24 minutes and for C3 this is 36 min. This period is particularly useful as a test-case as it contains four halo CMEs.

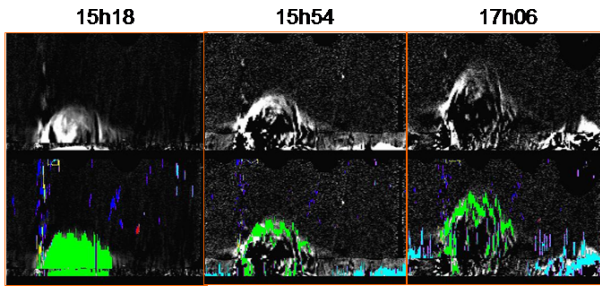


Figure 4.6: Illustration of detection of two CMEs. A sequence of 3 running difference $[\theta, r]$ -images is shown (top panel), containing 2 CMEs on 2003/11/11. The bottom panel shows the same information with the CACTus CME detections superimposed on it in green (CME nr 22) and in blue (CME nr 23).

4.4.1 General results

In total the CACTus software detected 47 events. They are shown as colored elongated regions in Fig. 4.5. The black lines indicate the corresponding CMEs listed in the CDAW catalog. The thickness of the lines is arbitrarily set to 30 minutes. The overall distribution in the (angle, time) space is very similar. Comparing the two sets in more detail is a delicate exercise. The ‘success rate’ of our software obviously depends on the tolerance allowed on the deviations. In Appendix B, an overview is given of the correspondence of the CDAW CMEs with the CACTus CMEs. In the next chapter we perform a broader comparison based on 4 months of data to obtain a more general view on the differences in measurement and their influences on statistical distributions. For space weather applications it is important to note that all 4 halo CMEs listed in the catalog have been detected, three of them with an angular width larger than 200° . Halo CMEs are particularly difficult to detect in white light images due to the nature of Thomson scattering (Hundhausen 1993).

Of the 16 CDAW CMEs, 15 CMEs are reproduced with nearly identical time of appearance and angular location. The CACTus software found 47 events whereas there are only 16 CME entries in the CDAW catalog. Part of the difference between the two numbers can be explained by the cases in which subsequent parts of a CME are detected as separate events. Unfortunately the CME definition (see section 4.3.3) does not give a clear view on when one CME is finished and the next one starts. The definition only requires a CME to be a ‘new’ feature. However, when these events appear too close in the time-angle space, also CACTus is unable to distinguish them. An example is shown in Fig. 4.10 (*right*). A new small bright feature is visible in the second frame in the SE (around 120°), but both CDAW and CACTus include this in CME nr 43. If this new event is the result of e.g. post eruption reconnection, it should be regarded as a new CME. Cases in which CACTus did split a CME in subsequent events while CDAW only lists the occurrence of the first, main event occur frequently (e.g. CME nr 23, followed by 24, 25, 26, 27). In the LASCO quicklook CME catalog (<http://lasco-www.nrl.navy.mil/cmelist.html>), which

is based on the daily observations of the operators, events nr 24-25-26-27 are described as ‘a ragged loop front with some gusty outflow, possible residual to some previous event’. Their detection by CACTus proves however that they do satisfy the CME definition as stated in section 4.3.3. Again this highlights the shortcoming of the definition.

We also found small events that are ‘far from’ any CDAW CME, but that do satisfy the CME definition. Some of these are generated by fast streamer evolution and streamer deflections. Whether these are classified as CMEs or not, they are without doubt an indication of coronal activity. In at least some cases, our software has found ‘unreported CMEs’. An example of such a case is shown in Fig. 4.7. This demonstrates that also the manually assembled catalogs do not have a 100 % success rate.

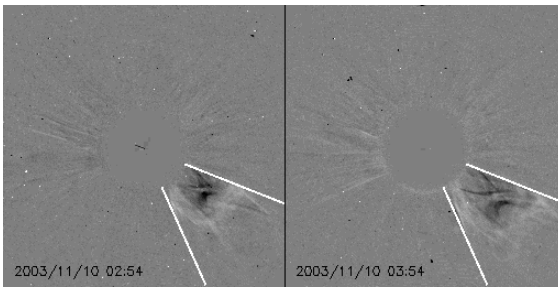


Figure 4.7: The unreported CME nr 10, lifting off at 02h06 on 2003/11/10 is visible in the south-west of the C2 FOV. Two C2 difference images are shown, 1 hour apart from each other. The straight lines limit the angular span given by CACTus.

4.4.2 Measurement of spatial CME parameters

In Fig. 4.8 (*left*) the CDAW principal angle (vertical) is plotted versus the CACTus principal angle (horizontal). Halo CMEs are not included since no principal angle is measured for them. All non-halo CMEs have a CACTus principal angle within 18° of the CDAW equivalent. The mean difference in principal angle between the CDAW and the CACTus values for all non-halo CMEs is 7.80° .

Similarly, the comparison of the CME width is plotted in Fig. 4.8 (*right*). In contrast to the principal angle, this graph reveals clear discrepancies between the CDAW and the CACTus measurement. For CMEs with a width smaller than 180° there is still a relatively good correspondence between the catalog and the CACTus output. This is re-assuring as 94 % of all CMEs listed between 1996 and 2003 in the CDAW catalog belong to this category. For wider CMEs the difference is larger. Let us take a closer look at CMEs nr 37, 23, 43, 22, 4 and 14 which show the strongest deviations.

In the case of CME nr 37 (Fig. 4.9) CACTus measures the same southern edge as CDAW, but at the north it includes more outflow than only the bright core. The corresponding speed profile is shown in Fig. 4.11 (*right*). In this plot we can indeed distinguish two different parts: a dense part at the left, which corresponds to the brightest feature of the CME and a somewhat detached, scattered part at the right (= north). The only argument in favor of not including the northern extension is of morphological nature: the excess coronal mass in Fig. 4.9 forms a suggestive nice round bow to which the detached side-outflows detected by CACTus do not ‘seem to belong’. The fact that the streamers seem to be pushed aside by the CME indicates that its angular ‘cone of influence’ at least reaches further than the obvious bright arch. Since no explicit morphological requirement

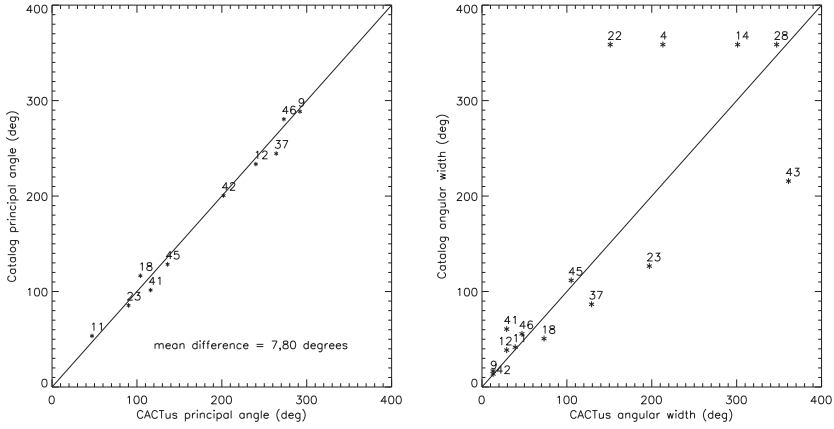


Figure 4.8: *left*: Plot comparing the principal angles. No halo CMEs are plotted since no principal angle can be measured for these CMEs. The mean difference in principal angle between the catalog and the CACTus values for all non-halo CMEs is 7.80° . *Right*: Plot comparing the angular widths. The four CMEs at the top (22,4,14 and 28) are all listed as halo CME in the catalog. At the contrary, CME 43 is detected as halo by CACTus, but not so listed in the catalog (see Fig. 4.10(*right*)).

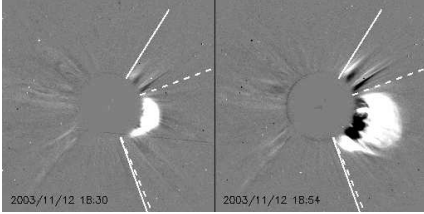


Figure 4.9: LASCO C2 running difference images showing CME nr 37. The solid lines limit the angular span given by CACTus, the dashed lines shows the CDAW detection. The corresponding CACTus speed profile is plotted in Fig. 4.11 (*right*).

has been programmed in CACTus, the software does include all the side-outflows or other signatures. The underlying problem is that it is not at all obvious what is meant with the word ‘discrete’ in the CME definition in section 4.3. The operator assembling the CDAW catalog has interpreted that the CME extension corresponds to the discrete region covered by the bright bow in Fig. 4.9, while CACTus has determined the CME extension to be the discrete region showing a clear velocity signal. A point to mention here is that due to the running difference, features outside the ejecta i.e. the compressed and deflected material around the real CME are overemphasized. That makes the measurements of angular extensions and even position angles dubious.

What makes CME nr 43 to deviate so much? CACTus found this CME to be halo, but CDAW only mentions an angular width of 217° . Looking at two difference images (Fig. 4.10, *right*) the leading edge indeed seems to cover only a partial halo CME in the east. CACTus however also detected outflow with higher speeds appearing some time later at the west. These data points indicate small features blown away along and in between the two streamers present.

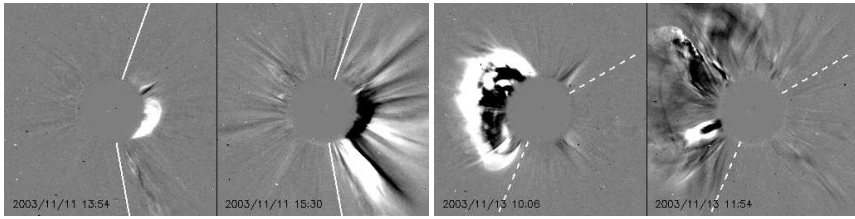


Figure 4.10: *Left*: C2 running difference images showing CME nr 22. The full lines limit the angular span given by CACTus. CDAW listed this CME as a halo. *Right*: C2 running difference images showing CME nr 43. The dashed lines limit the angular span given by CDAW. CACTus found this CME to be halo.

It is striking that in the case of CME nr 22, the discrepancy between the CDAW catalog and CACTus is reversed: CDAW list it as a full halo CME while CACTus found an angular width of only 150° . Fig. 4.10 (*left*) shows that it is indeed very difficult to define the edges of the CME. Fig. 4.11 (*left*) shows the velocity profile of the CME over the angular range where the CME was well detected by CACTus. Why did CACTus miss the rest of the CME? A similar problem occurs with halo CMEs 4, 14 and 28: CACTus found no sufficient signal of outflow velocities to conclude that these events were 360° -halo CMEs. However, it is instructive to note that between 1996 and 2004, the CDAW catalog lists 298 CMEs with an angular width larger than 270° , of which 281 (94% !) are listed as halo CMEs. This indicates that the word ‘halo’ is not used in the strict 360° sense but that the halo-label is (almost always) given as soon as the angular width exceeds 270° (or even less). In this sense, we conclude that CACTus did find CMEs nr 14 and 28 to be halo CMEs.

4.4.3 Velocity measurement

The CDAW catalog attributes to each CME a single velocity value called the ‘primary speed’ of the CME. This primary speed is typically derived from tracking the leading edge. In contrast, our software determines a velocity in each direction θ within the angular span of the CME, resulting in velocity profiles as shown in Fig. 4.11. From these plots it is clear that describing a CME with only one speed does not reveal the complete picture: structure can be seen in the figures hinting at the internal configuration and velocity distribution of the CMEs. CACTus calculates a reference velocity value for the CME as a whole by taking the median value of all detected speeds within the CME. Although we are aware of the fact that the median speed has no physical meaning itself, it is a proxy for the overall CME speed. This median CACTus speed is listed in the output table (see Appendix B) and differs significantly from the CDAW speed. Since the leading edge speed is usually the highest speed present in a CME CACTus measures systematically a lower speed than CDAW (Fig. 4.11 illustrate this effect).

Fig. 4.12 is a comparative plot of the measured speeds, CDAW (vertical) versus CACTus (horizontal). For each common CME we have drawn a boxplot. The horizontal box contains the central 50% of the measured speeds. The vertical line in the box is the median speed, given in the CACTus output list. The whiskers at both ends indicate respectively

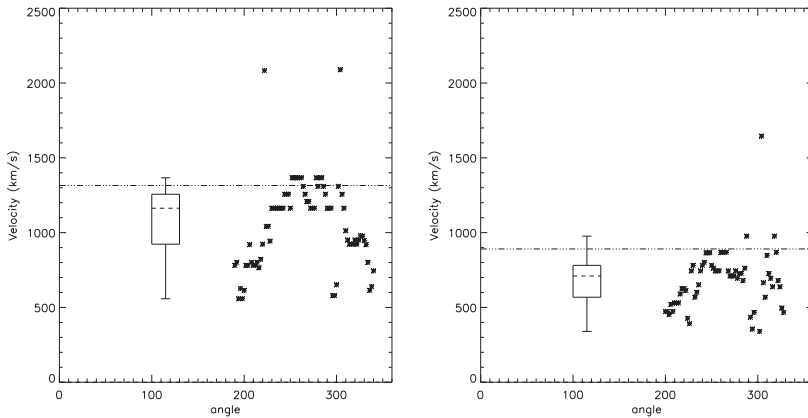


Figure 4.11: CACTus velocity profile of CMEs nr 22 (*left*) and CME nr 37 (*right*) as a function of the angle, measured counterclockwise from the north. The dashed line represents the CDAW speed. On the left the boxplot is drawn: the vertical box contains the middle 50% of the measured speeds. The horizontal line in the box is the median speed, given in the CACTus output list. The whiskers at both ends indicate respectively the minimal and maximal detected speeds within 1.5 times the box length from the edge of the box, speeds further away are disregarded as outliers. (see appendix C for a more detailed description of the boxplot.)

the minimal and maximal detected speeds within 1.5 times the box length from the edges of the box; speeds further away are disregarded as outliers. See appendix C for a broader explanation of the boxplot. Note that, apart from CME nr 9 (which has a ‘poor quality’ label in the CDAW catalog, see Appendix B), every boxplot crosses the diagonal. This indicates that the primary speed in the CDAW catalog is indeed found by CACTus *somewhere* along the CME.

The CDAW CME catalog also contains the acceleration of the CME. At present, it is not possible to measure this parameter with the CACTus software since the Hough transform detects ridges in the $[t, r]$ slices as straight lines. This implicitly assumes constant velocity CMEs. To better estimate the final CME-speed, we could apply the Hough transform to higher radial distances ($> 3 R_{\odot}$) only, since from this point on CMEs are expected to have relatively constant speeds or alternatively apply a second order version transforming each $[t, r]$ slice in a 3D Hough space.

4.5 Discussion

We have shown that it is possible to fully automatically detect CMEs in coronagraphic image sequences, estimate its main characteristics (time, principal angle, angular width, velocity) and produce a CME catalog just as human operators do it. 15 of the 16 CMEs in the test data set were recovered with nearly identical starting time and principal angle. The angular width and speed measurements deviate most from manual detection.

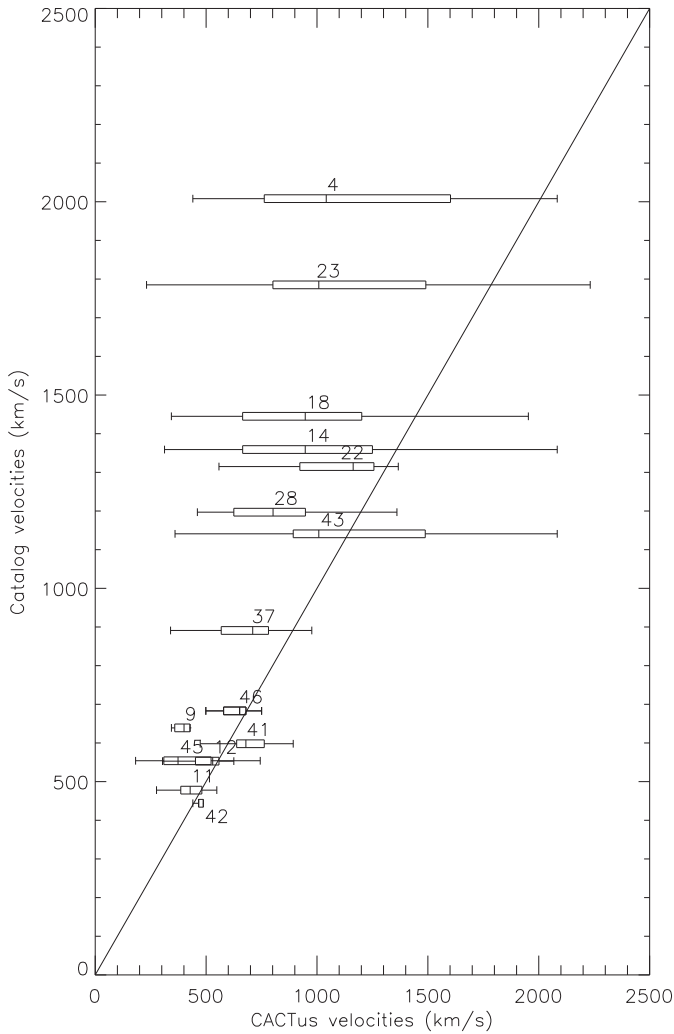


Figure 4.12: Comparative plot of the measured speeds. For each CME we have drawn a 'box and whisker plot' (or 'boxplot'). The horizontal box contains the central 50% of the measured speeds. The vertical line inside the box is the median speed. The whiskers at both ends indicate respectively the minimal and maximal detected speeds within $1.5 \times$ the box length from the edge of the box. See Appendix C for a more detailed description of the boxplot.

CACTus found nearly 3 times as many CMEs as there were listed in the CDAW catalog (in 2004). In some cases, CACTus included a range of weak transients not included in the CDAW CME catalog because they were regarded as only ‘gusty outflow’. However they do satisfy the definition of a CME as given in section 4.3. In some cases, CACTus has split a CME in separate events where the catalog has only listed the main event. While this might seem only a matter of CME-bookkeeping, the statistical analysis in chapter 5 shows significant differences in CME width and latitude distributions. Finally, there were also moving features in which the software did detect indisputable CMEs that were missing in the CDAW catalog. This means that the (up till now) reference catalog also does not have a 100 % success rate.

By carefully studying the discrepancies between the CDAW catalog and the output of CACTus we found out that the differences were usually not generated by imperfections in our software or by inattentive human operators, but instead by the vagueness of the concept ‘CME’ itself. It is, for example, basically undefined what the temporal and spatial extension of a CME is. When one CME follows immediately after another, it is hard to come up with observational criteria that define the split between the two CMEs. When does a CME end and when does the next one start? Also in the spatial domain ambiguity rules: is a CME limited to the region characterized by excess brightness, to the region showing clear outflow velocities or does it include the whole ‘cone of influence’ including wave or shock signatures driven by the CME? In a theoretical framework, the extension of a CME could be defined in terms of magnetic separatrix surfaces but, when having access to coronagraphic data only, such concepts are not applicable. A refinement of the concept of ‘CME’ is thus needed and an understanding of the 3D structure is required for this. A good prospect for this is the STEREO mission, where the coronagraphic images of the same CME will be viewed from 2 viewpoints and be combined with MHD simulations.

Chapter 5

Statistical analysis of coronal mass ejections during cycle 23

In this chapter we present the first ‘objective’ LASCO CME catalog, a result of the large scale application of the CACTus software on the entire LASCO archive. The purpose of this chapter is to study the solar cycle behaviour of coronal mass ejections during the interval September 1997 - June 2006. Our study is based on observations obtained nearly continuously by LASCO, the first instrument in space observing the white light corona over an entire solar cycle (cycle 23). We studied the evolution of the CME characteristics over the solar cycle and compared them with similar results obtained by manual detection. Pre-LASCO studies have revealed the basic properties of CMEs and can be found in Howard et al. (1985), Hundhausen (1993) and references therein. The first study to provide a statistical view of the properties of CMEs observed by LASCO during 1996-1998 is given by St. Cyr et al. (2000) followed by Yashiro et al. (2004), for the period 1996-2002. These studies are based on the manual detection of CMEs and are therefore possibly biased by interpretation.

5.1 Composition of the catalog

We have applied a stable version of the CACTus code to the available data from the LASCO C2 and C3 instruments. Prior to preprocessing, the images are tested for their reliability. This step is performed in order to limit the amount of false detections due to corrupt images. They arise e.g. from dust particles or small debris flying in front of the telescope just at the time an image was taken, from highly deviating exposure times and from errors in data acquisition, transmission and reconstruction. To limit the computation time, the validity of the image is only tested by verifying meta data contained in the FITS file headers. A set of parameters evolved through real-time application and rejects the majority of corrupt images, known to trigger a false CME detection. Only images satisfying the conditions summarized in table 5.1 are accepted. This approach is not 100 % foolproof but only few bad images for which nothing unusual is reflected in the image header pass the test. Three examples of such images are shown in Fig. 5.1. The LASCO coronagraphs are very sensitive to dust particles that pass through the field of view. Very small dust particles, at small angles from the Sun, get illuminated by the bright Sun and are easily seen. Usually the space environment is very clean, but sometimes a streak is observed in the images. Since the instrument is focused at infinity the particles appear out

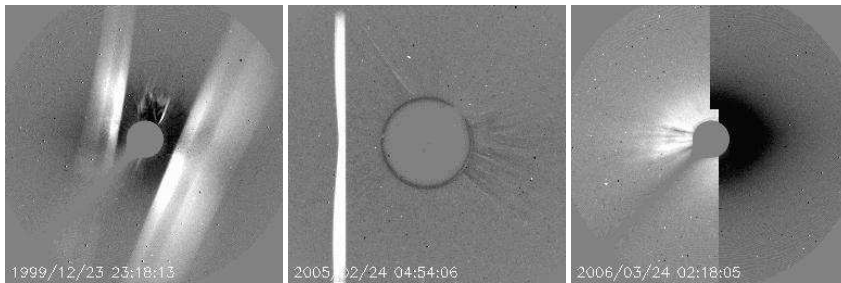


Figure 5.1: Three examples of bad LASCO images that passed the CACTus ‘sanity check’ are shown. The two first images contain light scattered from dust particles or larger debris passing through the field of view. The image on the right is due to technical data acquisition problems. This is a standard problem when working with real-time images.

of focus and thus broad. Hence they are not removed by our denoising technique in the preprocessing step.

For practical reasons we have organized the detections per month. To avoid wrong or incomplete detections of CMEs which occur near the beginning or end of a month, we have added to each month the last day of previous month and the first day of the next month. For example, a CME which first appears in C2 on the 31 of March at 22 UT is still visible in the C2 field of view on April 1. Without adding March 31 at the beginning of the April sequence, this CME would seem to appear on the 1st of April and thus it would be detected wrongly.

Instrument	C2	C3
Image size	1024 × 1024	1024 × 1024
filter wheel	Orange	Clear
polar wheel	Clear	Clear
lp_num	Normal	Normal
Minimal exposure time	25 sec	18 sec
Maximum number of zero pixels	186 368	186 368
Minimal average value	2350	1800
Ratio (average / exposure time)	-	[87,118]

Table 5.1: Table summarizing the header parameters required for image selection (top) and image quality verification (bottom). As can be deduced from the table, only unpolarized, full-size images are used for our CME detection.

During the first months of the mission, most LASCO images had their top and bottom chopped off for telemetry optimization. This style of image compression was gradually decreased and abandoned in September 1997. Moreover, the nominal cadence of both C2 and C3 was only 1 image per hour (compared to resp. 3 and 2 per hour in the extended phase of the mission). For these reasons the current data set used for our long-term analysis runs from September 1997 until June 2006. Nominal observations have

been interrupted as a consequence of exceptional satellite problems. A 3 months data gap occurred in 1998 from 24 June to 22 October due to an unexpected loss of contact with the spacecraft. Subsequent failure of all three gyroscopes caused an interruption from 21 December 1998 to 6 February 1999. A third crisis occurred in June 2003, when SOHO's main antenna became stuck. Using the secondary antenna this problem was overcome and nominal observations resumed on July 10. Further, regular gaps of a few days through the whole mission's lifetime occur during the SOHO keyhole periods. This chapter describes the first results of the CACTus CME catalog and gives hints for future analysis and program improvements.

5.2 CME rate during cycle 23

Figure 5.2 shows the monthly CACTus CME rate for cycle 23, with the sunspot number superimposed. We have also plotted the CDAW CME rates, obtained by manual detection at NASA-Goddard Space Flight Center (Coordinated Data Analysis Workshop Yashiro et al. 2004). It is available online and is widely used by the solar community as a reference LASCO CME catalog. None of the CME-rates have been corrected for instrument duty cycle or visibility function. Since the CDAW detection rates have also not been corrected, we can directly compare the 'raw' numbers with the CACTus rates. Given the very stable LASCO operations starting after February 1999, we believe that a correction would not significantly alter the conclusions on the CME rate described in this chapter. We have applied a smoothing function on the monthly CME and sunspot rates A_i by computing a boxcar average over a smoothing window of 13 months. This means for every value i in the range 0 to N , we substitute A_i with R_i as

$$R_i = \frac{1}{13} \sum_{j=-6}^6 A_{i+j}, \text{ setting } A_{i+j} = \begin{cases} A_0 & \text{if } i+j < 0 \text{ and} \\ A_N & \text{if } i+j > N \end{cases}$$

where N is the number of elements in A .

In this section, we focus on the CACTus CME rate properties and its connection to the solar cycle. Summarized, our findings are that [1] there is a great discrepancy between the CACTus and CDAW curves both in shape and in amplitude. [2] the CME rate follows the solar cycle and increases from 2.5 CMEs per day during minimum to 7.5 CMEs during maximum, nearly half of them are narrow events ($< 20^\circ$); [3] during the ascending phase the CME rate increases less steeply as compared to the previous cycle, this is consistent with the lower sunspot maximum of this cycle; [4] the CME cycle lags behind the sunspot cycle with a delay of 6 to 12 months and [5] the Gnevyshev gap (GG Gnevyshev 1967), the dip in the maximum phase of solar activity, is well retrieved in the CACTus CME curve.

[1] The large discrepancy between the two CME curves is very remarkable. It is most pronounced during solar maximum years, but is small during the first half of 1998 and from July 2005 onwards. The 'third peak' (~ 2005) in the CDAW CME rate is surprising. Since CACTus measures a systematic decrease from maximum to minimum and also the sunspot number decreases continuously we do not interpret the CDAW peak as solely due to physical effects. Instead, a better personnel training after years of LASCO CME

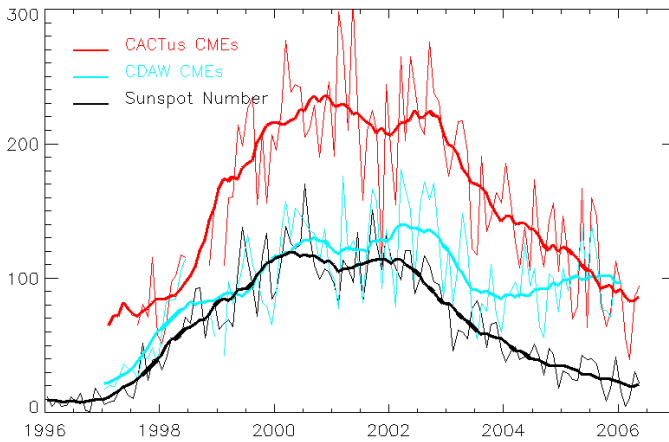


Figure 5.2: The monthly and monthly smoothed CME rates for cycle 23 from September 1997 through June 2006, extracted from the CACTus (red) and the CDAW (blue) CME catalog. As a reference we have overplotted the monthly and monthly smoothed sunspot number (black) produced at SIDC - Royal Observatory of Belgium. Because of the large data gaps in 1998-1999 the values are only reliable from Feb 1999 onwards.

observation could be the cause of better observation of faint and/or small events (Gopalswamy, private communication). This shows the need for a more objective measurement of CME-activity in the corona. As is illustrated in Fig. 5.3 the divergence is mostly due to the inclusion of events with small angular extent in CACTus. In these 4 graphs we have plotted the CDAW and CACTus CME rates versus the sunspot number for different CME sizes. The upper two plots show this curve for (a) ‘narrow events’ (CME width $< 20^\circ$) and for (b) small events ($20^\circ < \text{CME width} < 40^\circ$), the lower plots show this curve for (c) the remaining CMEs (CME width $> 40^\circ$) and for (d) the total curve. Curve (c) distinguishes itself from the other 3 curves in two aspects: (1) it shows the best correlation and (2) the CACTus CME rate is below the CDAW CME rate. In the next paragraph we show that this lower CACTus CME rate is not because the CMEs are not detected, but because CACTus measures often a smaller CME-width than CDAW. The two upper curves indicate that the CACTus-CDAW distance changes over the solar cycle due to the (not) inclusion of smaller events. Narrow/small events, do not form one separate category, but are a combination of several phenomena. This leads to a discussion on the ‘freedom of definition’ of what a CME is. Small discrete outflow is often seen during times of high CME activity, but it also occurs independently. They are often neglected or interpreted as being part of a larger eruption. We will give a counter example to illustrate that this is not always the case.

[2] The CME occurrence rate is an index of solar activity. It has long been known to track the sunspot number and other indices of solar activity (Kahler 2006). The CACTus CME rate increases roughly with a factor 3 from minimum to maximum (see Table 5.2). This factor is more or less stable for the different sizes of CMEs. In total there are around

LASCO CME rate				SMM CME rate		
Year	CACTus			total	Year	total
	width < 20°	width > 20°	total			
1997	1.2	1.4	2.6	1.4	1986	0.3
1998	1.4	2.0	3.4	2.7	1987	0.7
1999	2.6	3.5	6.1	3.0	1988	1.7
2000	3.2	4.4	7.6	4.3	1989	2.8
2001	3.2	4.2	7.4	4.0		
2002	3.3	4.2	7.5	4.5		
2003	2.8	2.8	5.6	3.0		
2004	2.2	2.3	4.5	3.0		
2005	1.7	1.9	3.6	3.3		
2006	1.4	1.1	2.5			

Table 5.2: *Left:* Table summarizing the daily LASCO CME rate throughout the solar cycle. The first three columns contain CME rates retrieved by CACTus, the last column is the daily CDAW CME rate. For CACTus we have shown the rates for narrow CMEs separately from other CMEs. The daily CACTus CME rate increases roughly with a factor 3 from solar minimum to solar maximum. It is computed from the yearly CME rate divided by the number of months for which these rates were available. The rates are not corrected for other data gaps (e.g. due to keyhole periods). They are thus a lower limit. *Right:* For comparison we have also plotted the available daily CME rates for the previous cycle, extracted from SMM data as reported by Webb and Howard (1994).

2.5 events per day during solar minimum and 7.5 events during solar maximum, nearly half of them being narrow (CME width < 20°).

[3] As a reference we have added in Table 5.2 the corrected daily CME rate of the previous cycle for the years 1986 - 1989 reported by Webb and Howard (1994). It is extracted from SMM (Solar Maximum Mission) data and was corrected for instrumental visibility and duty cycle (number of effective observation days). The absolute rates for this cycle are much higher than those reported for the previous cycle. This is due to the better instrument sensitivity, the enormous dynamic range of LASCO, the much larger field of view and the more uniform coverage of data over a long period of time. On the other hand, the daily rate increases more sharply towards solar maximum for the previous cycle, i.e. from 0.3 events during 1986 to 2.8 event during 1989. The SMM data was only available until then, but the maximum was achieved some months later. This much steeper rise is consistent with the higher peak in the sunspot curve for previous cycle. From this comparison we estimate that the CME-activity was much lower during the current cycle compared to the previous cycle.

[4] CME activity shows a significant peak delay w.r.t the sunspot cycle (see Fig. 5.2). Focussing on the monthly averaged curves, we find a lag-time varying from 6 months (max peaks) to 1 year (GG). This is in contradiction with the CME statistics of cycle 21-22 described by Webb and Howard (1994) who state that the CME rate tends to track the solar activity cycle in both amplitude and *phase*. This phenomenon of time-delay, often referred to as hysteresis, has been observed in several activity indicators. Chromospheric and coronal emission lines show delays of 1 to 4 months w.r.t. the sunspot index (Don-

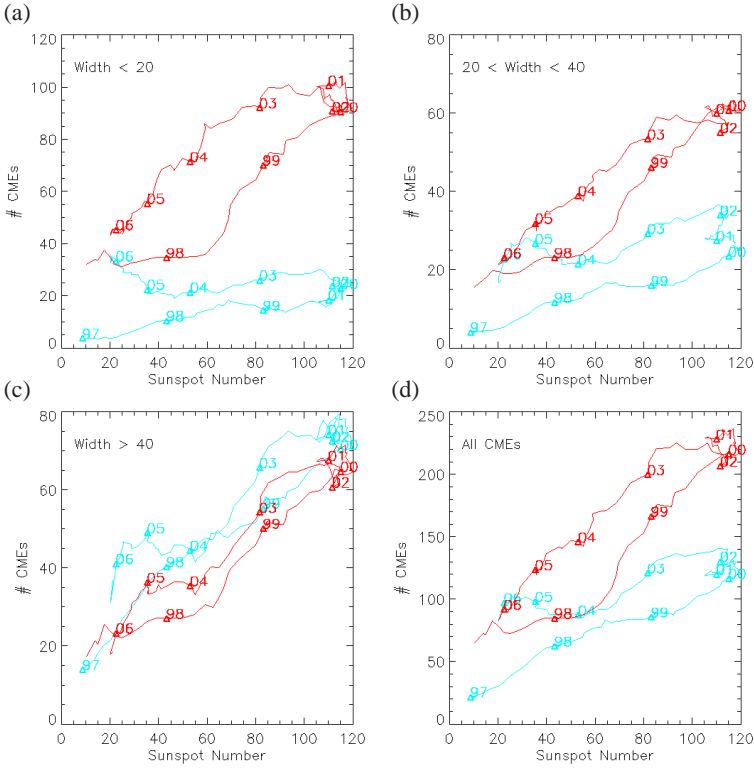


Figure 5.3: Plots showing the correlation between the CME rates (smoothed) and the sunspot number (smoothed). The red curve represents the CACTus CME rate and the blue curve the CDAW CME rate. The numbers in the plot refer to the years. The plots correspond to different CME-widths. The upper two plots show this curve for (a) ‘narrow events’ (CME width < 20°) and for (b) small events ($20^\circ <$ CME width < 40°), the lower left plot (c) show this curve for the remaining CMEs (CME width > 40°) and the graph at the bottom right (d) contains all CMEs.

nelly et al. 1983, Bachmann and White 1994) and time-lags of 10 to 15 months are found for flare rates (Özgüç and Ataç 2001, Temmer et al. 2003). What causes this time delay? On time-scales of the order of one month, local oscillations in the sunspot curve are possible due to the emergence and decay of active regions as well as regions rotating in/out view (rotation period ≈ 27 days). The convolution of these two effects leads to the sharply oscillating monthly sunspot index. The second effect (rotating sun) is almost totally eliminated from the monthly CME rate, since also back-sided CMEs are captured by LASCO. The spiky CME rate is thus true variation in CME-activity originating from the whole Sun. The monthly smoothed curves on the other hand have these local effects eliminated and we are left with a delay of more than 6 months. The mechanism leading to these

and similar delays is not understood and several solutions have been proposed. Gopal-swamy (2004b) attributes this delay to the fact that CMEs not only erupt from sunspot regions, but also from non-sunspot regions (quiescent filaments). However, the fact that a significant time-delay is also observed in flare-rates might point towards an additional mechanism causing a delay between flux injection (sunspot formation) and flux expulsion (energy release) in the corona. As we shall see in the next section (Fig. 5.15), the latitudinal distribution of CME occurrence, indicates that during solar minimum (1997) CMEs erupt mainly from within 20° of the solar equator. These latitudes are linked to the ‘old’ sunspot groups (see butterfly diagram in Fig. 5.16) and not to the regions belonging to the new cycle which appear at higher latitudes ($20 - 40^\circ$).

5.3 Illustrations of the CME definition ambiguities

In the next section we present the statistical results of the CACTus CME parameters and compare them with the CDAW CME statistics. The discussed parameters are the CME width, the latitude and the speed. They are all measured in projection in the plane of the sky and therefore, they are labelled ‘apparent’. In this section we give a few examples of typical effects that cause uncertainties in the CME parameters. They help us to understand why the same data can sometimes be interpreted differently, by humans or by a detection program. The identification of CMEs in white light is based on the detection of excess brightness, moving radially away from the occulter in a coherent way. Any other associated features that cause brightness enhancements in the white light images and that move radially away from the Sun, can thus also be interpreted as a part of the coronal mass ejection. We want to argue that the appearance of CMEs in white light images is still not well defined. Every observer interprets the observation in his or her own way and this creates ambiguities in the parameters listed. This is not such a problem when only one CME catalog exists, utilizing a consistent interpretation, but the current evolution is towards more catalogs, generated by different systems and institutes. A converging definition is thus appropriate. We show several examples of features that introduce ambiguities and propose additions to the classical observational CME definition. The list given below is not intended to cover all ambiguity-issues. In this section we do not discuss the issue of the narrow events, which are not granted the status of ‘CME’ in the classical CDAW catalogue. These events are discussed in section 5.4.2.

As illustration we discuss the appearance of shocks in white light images, the detection of halo CMEs and the white light signature of loop openings. These three features cause confusions, mostly in the measurement of the CME width and CME speed parameters.

5.3.1 Shocks

In the white light corona, the high quality LASCO images provide an excellent data set for locating possible white light signatures of shocks. Observations of distant streamer deflections are considered to offer the best evidence of shocks in the corona (Sheeley et al. 2000). Thanks to the increased instrument sensitivity of LASCO these have been numerous observed (Vourlidas et al. 2003). Also bright sharp fronts, moving ahead of ejected mass (the so-called forerunners) and tapering off to the sides (like a bow shock) are

interpreted as direct evidence of shocks in the corona. Nevertheless their identification and interpretation is still ambiguous. Intensity in white light images is directly related to the electron density (integrated along the line of sight) and hence, an intensity enhancement can occur as a consequence of wave or shock formation. Fast CMEs with speeds in excess of the ambient solar wind drive shocks ahead of them as they propagate from the Sun. As an example, Sime and Hundhausen (1987) observed a fast (1070 km/s) bright loop at the front of a CME which they identified as a coronal shock. Although the existence of CME associated shocks is now supported by a large amount of direct and indirect evidence, their imaging remains an observational challenge. Historically, the most important evidence comes from radio type II observations, caused by shock waves moving outward through the corona (?). However, it has to be mentioned that the relationship between type II bursts and CMEs remains unclear.

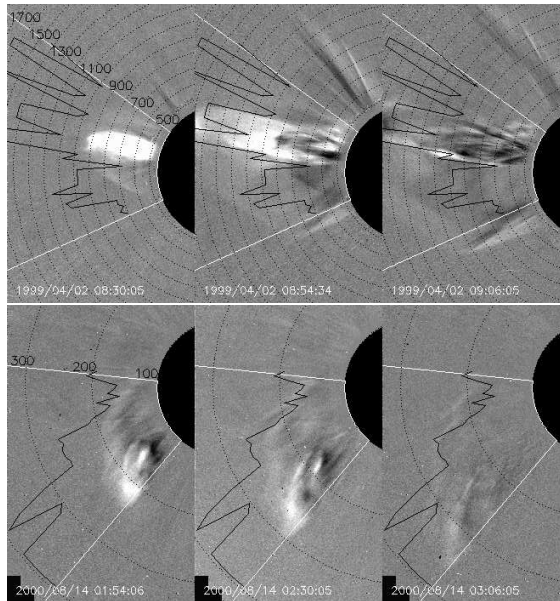


Figure 5.4: Two examples of possible indication of CME driven shocks are shown in running difference. The top event (April 1999) was simulated by Vourlidis et al. (1999). The sharp southern flank was interpreted as the white-light counterpart of a fast-MHD shock. The event at the bottom (August 2000) shows a slow CME accompanied by a faint feature traveling at low speed towards the east (this is left). The CACTus detection is marked by the two white lines. The black curve indicates the fastest speed measured in each radial direction. The velocity scale is given by the concentric circles (in km/s).

The existing CME catalogs make no distinction between the ejected plasma and the shock waves, while measuring the CME properties. Streamer deflections are classically not included when measuring the CME width, but a bright shock front is usually included. As a consequence, several CMEs are listed as ‘halo’ whereas in reality, it is often the

shock front that makes it halo. The CME width parameter is thus heavily biased for fast CMEs showing shock signatures. Two examples of possible indication of CME driven shocks are shown in Fig.5.4. The top event was simulated by Vourlidis et al. (2003). Their simulation confirmed that the sharp southern flank could be interpreted as the white light counterpart of a fast MHD shock. It was detected by CACTus to move at high speed (900 - 1300 km/s). At the bottom we show another example of a faint outward moving feature, which in this case is moving at slow speeds. Given the fact that the CME itself has a speed of 400 km/s, comparable to the ambient solar wind speed, and the not sharp edge, this feature is probably not a shock signature. An alternative hypothesis is that this feature is part of the overlying coronal structure and appears faint due to projection effects. This example shows that the measurement of CME width is a delicate exercise.

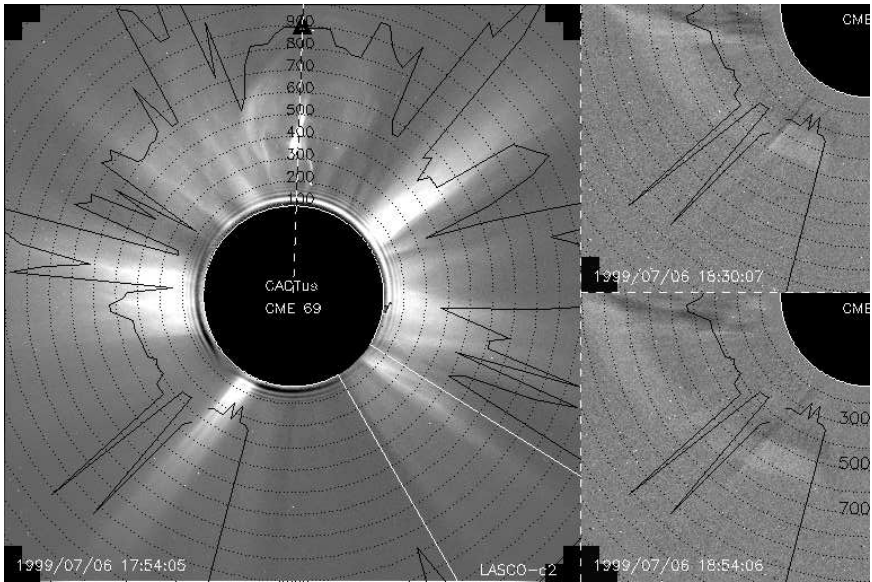


Figure 5.5: Example of the CACTus speed measurement of a halo CME and its associated shock. At the left, a background subtracted image is shown to illustrate the ambient corona. The ejected coronal mass and flux rope can be seen in the north. The CDAW linear speed is indicated by a black triangle (north). The two panels at the right show a zoom of the SE corner in running difference. A sharp bright front is observed to move at about 400 km/s. The sharpness of the front suggests that this feature is a shockwave, driven by the CME. The CACTus parameters are indicated as in Fig. 5.4.

Figure 5.5 shows a CME event, listed as ‘halo’ by CDAW and CACTus (i.e. the angular width exceeds 270°). It was thoroughly studied by Sheeley et al. (2000). The ejected coronal mass and flux rope itself can be seen in the north and appears as a ‘lightbulb’. In this direction the CDAW observer has measured a propagation speed of 900 km/s (indicated by the black triangle) which is listed as *the* CME speed. This speed corresponds well to the speed of CACTus in this direction. However, the CACTus profile reveals a

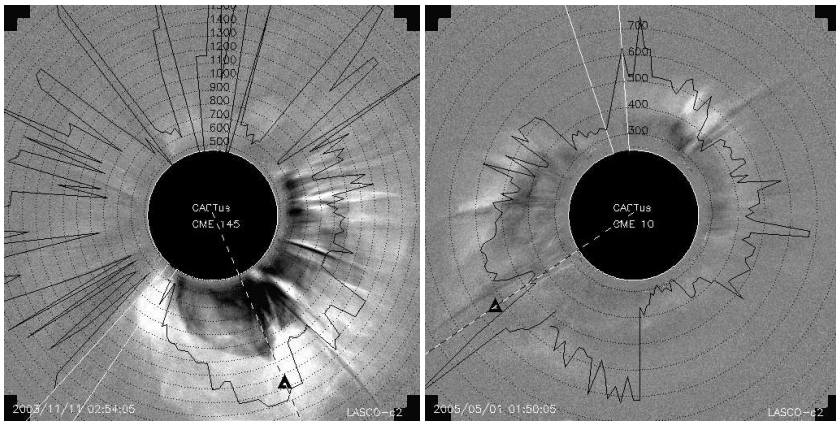


Figure 5.6: Two examples of CACTus speed measurement of halo CMEs and their associated shock. The black line indicates the CACTus speed (km/s) measured in radial direction. The triangle on the dashed line indicates the CDAW speed which was measured in this direction.

more complex speed profile. The two panels at the right show a zoom of the SE corner in running difference. A sharp bright front is observed to move at about 400 km/s. The sharpness of the front suggests that this feature is a shockwave driven by the CME. Contrary to many other examples, the front moves quite uniformly. This suggests that the underlying plasma is uniform. At the top of the two smaller frames a streamer deflection can also be seen to propagate outwards. This is generally accepted to be caused by an MHD wave or shock. The CACTus speed profile is not at all uniform with respect to the angle around the occulter. Although we connected the speed measurements in each radial direction, it should not be interpreted as the profile of *one* coherent structure. Instead, it is a collection of speeds from different features moving simultaneously with the CME.

Since an associated shock is a different feature than the erupting plasma ‘blob’, it is difficult to draw statistical conclusions on the basis of one measurement alone. The speed measurement in the classical CDAW CME list is consistently measured along the principal direction of eruption. This means it is less biased than the CACTus CME speed, which is calculated as the median speed of all speeds measured. At the other hand, shocks are a substantial part of CMEs and should thus not be left out in the CME description. CACTus offers a way to systematically measure CME shock speeds and link it to the plasma speed. The shock is not only interesting from scientific point of view, but is important for estimating the space weather impact of the CME, if directed to the Earth. We propose to separate the shock signature from the plasma blob while measuring the CME parameters and to measure both features separately. The current list of CME parameters can then be extended with a list of CME shock parameters. For CACTus, this would imply splitting the speed profile in a two parts. The fact that shocks have been numerous detected by CACTus illustrates that our software is sensitive enough to detect them. However, the challenge now is to automatically separate the shock from the bulk plasma.

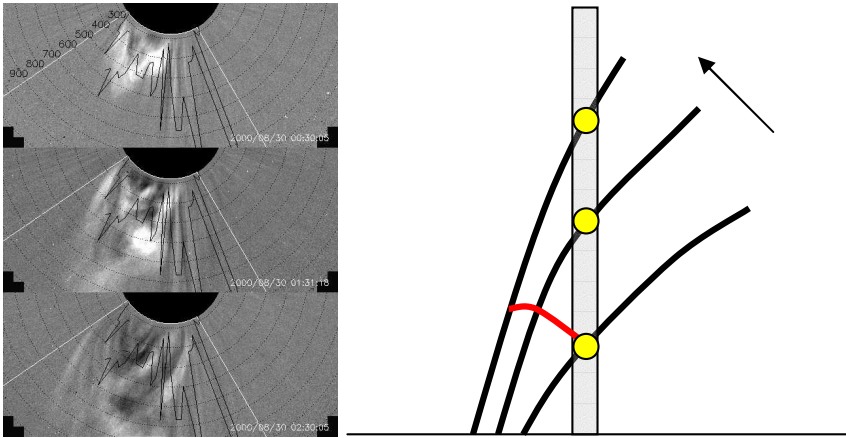


Figure 5.7: *Left*: Illustration of the detection of loop openings accompanying a CME eruption. *Right*: A cartoon which explains the ‘false’ impression of fast radial motion in a height time plot, caused by a loop opening.

5.3.2 Halo CMEs

The classical (observational) interpretation of the CME width, is the angle of a circular cone, having its vertex on the solar disk and the cone oriented in the direction of CME propagation (a more thorough explanation is given in Section 5.4.2). This description fails when the CME propagates close to the Sun-Earth direction. In that case, the base of the cone surrounds the occulter (or only partly) which means we cannot measure the angle of the cone itself. Also the propagation speed is subject to severe projection effect.

In Fig.5.6 we show two CMEs, both detected as halo by CACTus and CDAW. The first halo CME (*left*) is quite asymmetric in shape. The second example shows an almost symmetric elliptical speed profile, suggesting that its central axis of propagation is close to the line of sight direction. Zhao et al. (2002) exploited the cone model for halo CMEs appearing as ellipses around the occulter. The main idea is that in projection, an expanding circle is seen as an ellipse. By determining the parameters of the ellipse, the direction of propagation can be deduced and hence, the real CME parameters can be estimated. Cremades and Bothmer (2005) showed that the *circular* cone model could not fit a substantial number of halo CMEs and suggested the existence of real *elliptical* halos, observed as such, not only because of the effect of projection. Michalek (2006) used this idea and measured radial speeds in different radial directions to reconstruct the elliptical cone. Our detection program would be very much suited to do so, however, it would have to be adapted specifically for this application. For example, the CME speed profile would have to be separated from the associated shock speed profile as discussed above. We note that the elliptical cone model does not take into account the effect of the ambient corona on the CME propagation, and hence provides only a highly idealized empirical approach.

We comment additionally on the heavily varying speed profile in the left example. Such a highly oscillating speed is not realistic, and we stress that this speed profile is

not to be interpreted as such. Only the fastest speed detected in each radial direction is shown. We might thus simply have linked speeds of fronts which are moving independently. This phenomenon exactly occurs at places where the CME signal is at the level of the noise(north-east). This examples illustrates thus the present limit of our CACTus detection scheme.

5.3.3 Loop opening

Finally, Fig. 5.7 (*left*) illustrates the detection of loop openings during a CME passage. In the [time,height] diagram they show up as bright features moving outward at high speed. This ‘fast’ propagation is only apparent, as is illustrated in the cartoon (*right*). Since CACTus observes the brightness evolution along radial slits (vertical direction in the cartoon), a higher speed is measured: the yellow dots seem to move at high speed, while in reality the loop is expanding laterally. If CACTus would be able to recognize this pattern as loop opening, it could be used to automatically classify these features.

5.4 Statistics of CME parameters

We revisited the properties of coronal mass ejections using our new catalog generated by automated detection. In this section we discuss the evolution of CME parameters in the course of the solar cycle and compare the CACTus and CDAW statistics. In order to estimate the effect of measurement method on the different CME parameters (starting time, principal angle, angular width, speed), we have manually selected a sample of 336 CMEs belonging to both catalogs. It was impossible to *automatically* combine the two catalogs, since not one set of parameters was found to be best correlated (for example, timing or principal angle). An automatic procedure, would bias the results towards better correlation: Imagine a CME which is very differently parameterized in the two catalogs. An automated procedure would categorize these as different events and thus remove them from the correlation study. For these reasons we decided to study only a sample of joint CMEs, selected manually.

This sample was chosen large enough, such that the results are statistically significant and expandable towards the whole catalog. There are several approaches to select a good sample. As we have seen in the previous sections and as was already reported by other authors, CME parameters and occurrence depend on the solar cycle. Therefore, we have selected two different sub-samples, one representing solar minimum and the other solar maximum. We have chosen 1998 February and May as sample for solar minimum and 2000 April and August for solar maximum. For each day in each month we have plotted the detections on an angle-time map and have visually inspected the LASCO movies in order to decide which entries are describing the same event. This lead to 114 common events for the minimum sample and 222 common events for the maximum. Figure 5.8 gives an overview of the CACTus-CDAW correspondence for the two selected periods. During solar maximum, 80% of the CDAW CMEs could be connected to a CACTus CME detection, but only 60% during solar minimum. We attribute this lower value to the lower average intensity of the running difference images during solar minimum. At present the free parameters in our software do not scale with the solar cycle. It might

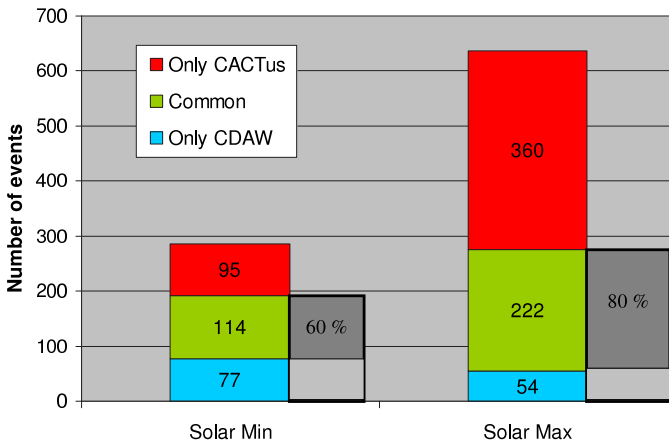


Figure 5.8: Graph illustrating the CACTus-CDAW correspondence for two selected samples. It is based on two months during solar minimum (1998) and two months during solar maximum (2000). The grey boxes only cover the CDAW CMEs. Only 60% during solar minimum and 80 % during solar maximum of these particular events could be connected to a CACTus CME detection (green). Beside these, CACTus has detected many more other events, which are not present in the CDAW catalog (red).

prove useful to study this issue to improve the hit-rate during solar minimum. One could e.g. investigate the dependency of background variability on the solar cycle. Apart from this general trend, there is an additional effect in our 1998 sample due to the larger time spacing between the images (30 min in 1998 versus 23 min in 2000). In the preprocessing step, we do normalize for this time difference, but this correction could introduce a lower average intensity for long periods of larger time spacing (low cadence) (see section 4.3, preprocessing). Beside the common events (green box), CACTus has detected many more other events, which are not present in the CDAW catalog (red box). In what follows, we try to reveal general characteristics of this large group of transients, left out by the classical CDAW CME catalogue.

5.4.1 Detection of first appearance

Figure 5.9 shows a histogram of time differences (CDAW-CACTus) of first detection. The binsize was set to 10 minutes. The histogram is heavily biased by the time-spacing between the LASCO C2-images. This peaks at 23 minutes in 2000, and around 30 minutes in 1998. From the histogram we deduce that during solar max, 77 % of the first detections differed maximal 1 image and during solar min the corresponding number is 64 %. This is a good result given the fact that CACTus approximates the CME trajectory linearly (i.e. no acceleration). Both physical and technical reasons account for a difference in detection of first appearance, we list three of them below.

[1] Fast CMEs can drive shocks ahead of them, and their ‘nose’ is observed as a bright (but faint) area about 30 min to 1 hour prior to the bulk CME eruption. Jackson

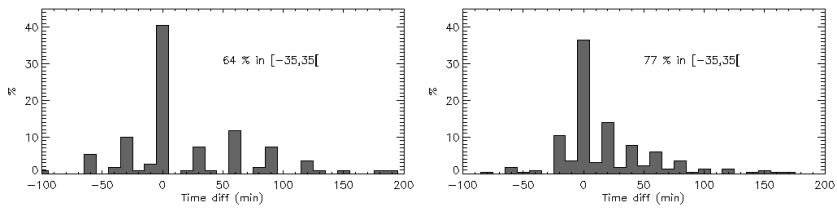


Figure 5.9: Histogram of CDAW-CACTus time differences of first detection for the 1998 sample (left) and the 2000 sample (right). The binsize was set to 10 minutes. The histogram is heavily biased by the time-spacing between the LASCO C2-images. The nominal time spacing is peaks around 23 minutes in 2000, and around 30 minutes in 1998.

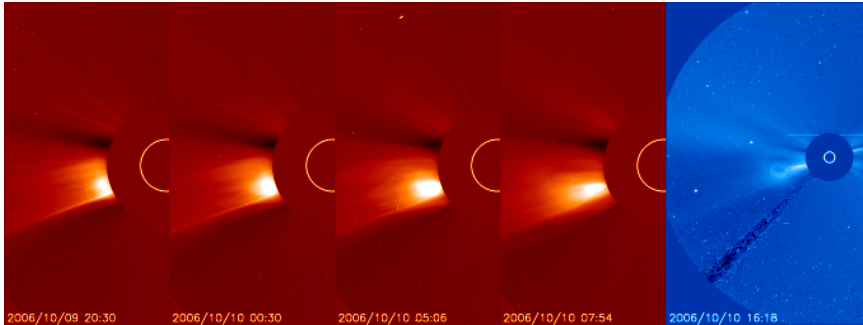


Figure 5.10: The first appearance of a CME is not always well defined. Here we show a sequence of C2 background subtracted images (red) and one C3 image (blue). A CME is seen erupting from the east limb, the CACTus speed measured was around 150 km/s. It is impossible to distinguish the background intensity prior to the event (streamer) and the erupting CME.

and Hildner (1978) have labelled them ‘forerunners’, and they are described as a region where the corona is slightly more dense than its pre-transient state. Depending on its intensity it will be detected as ‘first appearance of the CME’ by the observer/detection scheme.

[2] Another underlying mechanism causing a not sharp transition in intensity from background to CME is the pre-existence of bright material or the very slow rise of a bright structure, prior to the eruption. This is the case, e.g. for the so-called ‘streamer blowouts’ in which the streamer material is blown away as part of the CME (see Fig. 5.10).

[3] From Fig. 5.9 we can deduce that CACTus has a preference to detect CMEs more often early than late with respect to CDAW. This is a consequence of erroneously linking two sequential detections into one event. This is a typical example where the human interpretation *does* prove to be useful. CACTus detects motion in each (radial) direction independently. The information on morphology of the CME (e.g. light bulb) is thus not used. Whereas CACTus will detect 2 sequential CMEs as one bright moving blob, the observer will notice that it comprises of two events. This biases the CACTus timing

towards earlier appearance.

5.4.2 Apparent width of CMEs

The angular width of a CME is a measure of the volume in the corona that is ‘blown out’. The ‘apparent’ widths, generally derived from coronagraphic data, indicate the angular size of this volume projected onto the plane of the sky. This angular size, measured as the angular span around the occulter, remains quasi-constant while the CME is propagating outwards, which suggests that CMEs expand radially in a self-similar manner (Low 1982, 1984). A popular way to envision a CME geometrically is a circular cone, having its vertex in the source region on the solar disk and the cone oriented in the direction of CME propagation. In case of a limb CME, the cone angle corresponds to the angular span measured in projection onto the plane of the sky. However, the angular width (and latitude) derived from projected images, is only an apparent quantity that depends on the CMEs orientation with respect to the observer. A CME launched in a direction close to the Sun-Earth direction appears as a ‘halo’ or partial halo around the occulter. In this case the angular width derived from the coronagraphic observation does not have a geometrical meaning. Moreover, the ‘cone model’ is a too simplified picture. Often a flux-rope structure can be discerned and depending on the viewing angle, the CME will have a different angular width. Measurements of spatial parameters like CME width and latitude are thus only proxies for CME ‘volume’ and radial direction respectively.

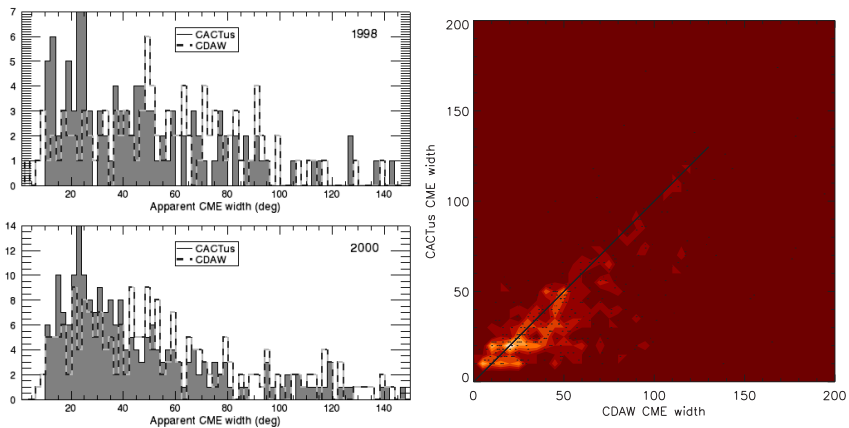


Figure 5.11: Comparison of the CME widths for the two test-samples. *Left*: In each graph a histogram of the CME widths is plotted, with a binsize of 2° . The upper panel is based on a sample of 114 CMEs selected in the year 1998 (Solar minimum) and the lower panel is based on a sample of 222 CMEs selected in the year 2000 (Solar maximum). As compared to larger statistics described in this chapter, these histograms appear quite ‘noisy’. This is due to the limited sample size. *Right*: Contour plot illustrating the correspondence between the CDAW and CACTus width measurements. The line $y = x$ is plotted in black.

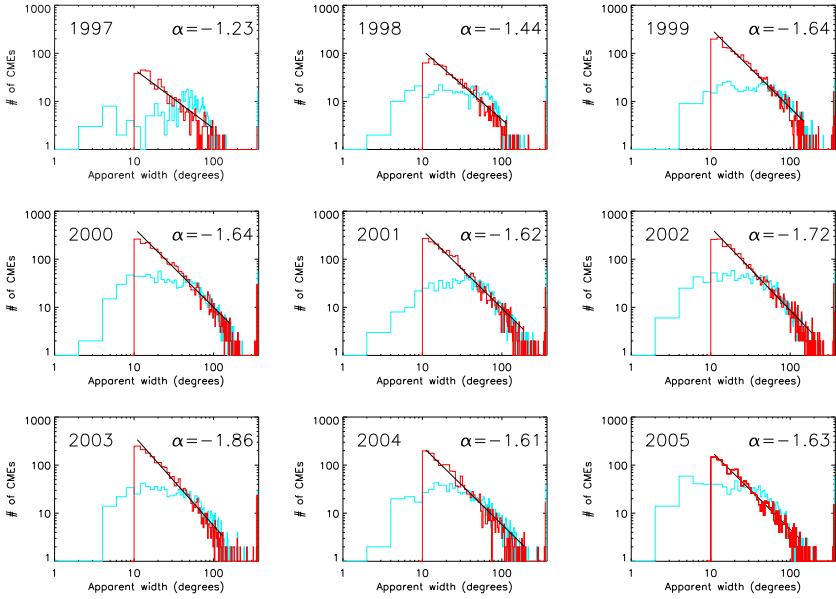


Figure 5.12: Apparent CME width distributions, displayed per year in log-log scale. The CACTus distribution corresponds to the red curve, the CDAW distribution is represented by the light blue curve. The distributions are not corrected for observing time.

In order to quantify how much the CME width distribution depends on the measurement method we first compare the CME widths for the selected group of *common* events, as described at the beginning of this section. In Fig. 5.11 (*left*) we have plotted the CME width histograms of the 2 samples in bins of 2° , which is the CACTus accuracy. The CACTus width distribution is peaked around $20\text{--}25^\circ$. CDAW at the other hand shows a much flatter distribution and measures systematically wider CMEs. At the *right* a contour plot of the CACTus versus CDAW CME widths is shown in the range $[0,200]^\circ$. The general direction of the bright contours match well the $y = x$ line. This confirms, at least for events smaller than 120° , that the CME width indeed is a good parameter for estimating the angular size and hence the volume of a CME. However, the large scatter of points indicates that the width is only vaguely defined, which leaves space for interpretation. For example should CME wave or shock signatures be included when measuring the angular extent of the CME or not? This is not merely a definition issue, the question is rather if an observer is capable to make the distinction between a wave or shock pileup and a ‘real’ CME only based on coronagraphic white light data. Our sample study showed that the CME width is particularly not well defined for CMEs exceeding 120° , especially halo-CMEs. Out of the 9 CACTus halo CMEs (from the sample) only 2 of them were also labeled ‘halo’ by CDAW. Inversely CDAW lists 4 halo CMEs which are not labeled halo in CACTus. As a consequence, care has to be taken when interpreting this parameter, especially for large CMEs.

In section 5.2 we showed that CACTus measures far more events than the observer lists and that this deviation is mostly due to events, having a width smaller than 40° . In Fig. 5.12 we have plotted the yearly CME width distributions, which reveal remarkable differences between the two catalogs. The CDAW CME widths are log-normally distributed, broadly peaked around 30° (e.g. Yurchyshyn et al. 2005) while the CACTus CME widths display a power law behavior, meaning the CME widths θ are distributed according

$$N(\theta) = N_0\theta^\alpha \text{ with power } \alpha \approx -1.6,$$

where $N(\theta)$ is the number of events with angular extent θ and N_0 a constant. In all the years plotted, the power law was achieved over one order of magnitude in the CME widths in the range $[10, 100]^\circ$. The minimal CACTus CME width was set on 10° , meaning that smaller events were discarded. Allowing detection of narrower CMEs can be done in the future to confirm the power law behavior at smaller scales. The power law of Fig. 5.12 indicate that eruptions and restructuring of the coronal magnetic field is a scale invariant process: There is no typical size of a CME. For CMEs this is an important new result, but for other types of coronal magnetic field restructuring it is well-known. For flares, for example, Crosby et al. (1993) has shown that a power law of ~ -1.6 characterizes the flare energy over 3 orders of magnitude. The fact that exactly the same power law applies for CME widths is intriguing. Possibly this is merely coincidence, possibly this hints at common physics of the flare and CME process. Further study is required here.

The fact that the CACTus CME width distribution does not saturate at small scales indicates that we did not detect the smallest scale yet. This suggests that towards progressively smaller angular widths, an increasing number of ejections was refused by the human (CDAW) operator, e.g. because no clear structure could be discerned in the transient. CACTus is fundamentally different since no morphological assumptions are made. Therefore we speculate that the criterion implicitly applied by the human is morphology. In other words, the smaller events do not fulfill the picture of a coronal mass ejection in the ‘classical’ sense, but are instead considered as ‘jets’, ‘gusty outflow’, ‘puffs’, ‘blobs’, etc. However, the continuous power law distributions down to 10° of the CACTus population suggests that this exclusion of smaller events might be inappropriate. Possibly the different appearance of small events in white light coronagraphic data is caused by projection effects (smaller events have more chance to be seen edge on and thus their structure is less apparent), instrumental effects (narrow CMEs appear fainter because the line-of-sight integration reaches much lower values than for larger CMEs), overlooking (during solar maximum, it is just not possible to manually select each separate small outflow), ...

Narrow transients

A discussion on narrow events, necessarily leads to a discussion on the definition of ‘coronal mass ejection’. Narrow transients are interesting, since they indicate the boundary of our knowledge and physical understanding. Many questions arise: Is there a continuum from large coronal mass ejections down to narrow ejections representing the continuous coronal wind outflow? Can we introduce the term micro- or nano-CMEs, cfr. nano-flares (Parker 1983)? Are narrow ejections a subset of ‘normal’ coronal mass ejections? Or do they form a separate class of events for which the pre-eruptive state is different from the ‘classical’ CME scenario? What can these events, which sometimes occur prior to a

larger CME, teach us on the CME initiation mechanism? If CMEs in general contribute to the reorganization of the large-scale magnetic field, does this also apply to these narrow events? If yes, they might act as ‘lilliputters’ gradually untying the magnetic field lines which finally leads to unstable configurations. Too many questions to answer here, and probably several scenarios apply. In what follows we will try to show how our software can contribute to the understanding of small events. We stress, that CACTus was designed to detect bright transients moving radially away from the Sun. From this point it is possible to tune the software for various applications: space weather forecasting will require another approach than the study of small events.

Not all of the many small events that CACTus has detected are ‘independent’ ejections. Some of them appear in a quasi-regular sequence. During times of higher solar activity, it is very difficult to trace the origin of every single eruption seen in LASCO. The only way to do so is by studying on-disk signatures, e.g. in EIT image sequences. Moreover, the event might be backside, appear just in between two EIT images, or originate higher up in the corona such that there *is* just no low-coronal evidence available. We should thus be very careful in interpreting and linking events.

Narrow events have been studied before by several authors. Howard et al. (1985) included these events as a separate class (spikes) in their CME statistics. Yashiro et al. (2003) have studied the statistical properties of CMEs smaller than 20° . They investigated 806 narrow CMEs from the CDAW CME catalog and found that (1) the fraction of narrow CMEs increases from 12% to 22% towards solar maximum, (2) during the solar maximum, the narrow CMEs are generally faster than normal ones and (3) the maximum speed of narrow CMEs (1141 km/s) is much smaller than that of the normal CMEs (2604 km/s). Therefore they concluded that narrow CMEs do not form a subset of and have a different acceleration mechanism from normal CMEs.

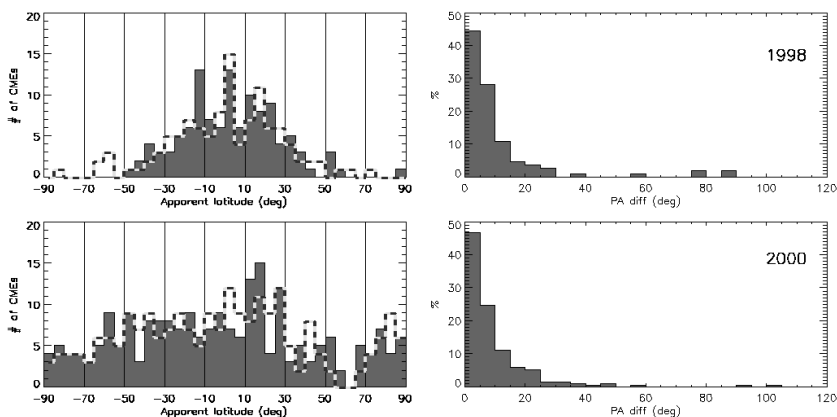


Figure 5.13: *Left*: Sample comparison of the apparent latitude distribution. The CACTus latitudes correspond to the filled graph, while the CDAW latitude distribution is shown in dashed line. *Right*: Histogram of the difference in principal angle CACTus-CDAW is plotted, we used a binsize of 5° .

Two (of the many) interesting problems related to small outflow are (1) the formation of the slow solar wind and (2) the initiation of coronal mass ejections. It is generally believed that the solar wind has two distinct components, ‘fast’ (> 550 km/s) and ‘slow’ (< 450 km/s), which differ in their physical nature and region of origin (e.g. Kohl and Cranmer 1999). Simply stated, they are the outer coronal counterpart of the two different magnetic field configurations: open and closed. However, *how* the slow solar wind originates from the closed field region, concentrated around the heliospheric current sheet remains unresolved. The most direct observation of the slow solar wind in the inner corona was first obtained by Sheeley et al. (1997) using the SOHO/LASCO observations of small density enhancements. Based on their small sizes, low intensities, radial motions, slow (100-400 km/s) but increasing speeds and location in the streamer belt they postulated that these so-called ‘blobs’ are passively tracing the slow solar wind, like ‘leaves in the wind’. This is in contrast to coronal mass ejections, which in general tend to have their own dynamic speed profiles. Moreover, no corresponding features were observed in the lower corona (LASCO C1). This suggested that these features seemed to be born high in the corona above the cusps of helmet streamers and not near the surface of the sun. Bemporad et al. (2005) at the other hand, found cases where narrow events resulted from open-closed field line interaction, connected to compact ejective flares. Post-eruptive ‘jets’ were simulated by Riley et al. (2002). They found cases where narrow closed field regions originate from post eruptive reconnection.

The occurrence rate of small events follows the solar cycle variation (Fig. 5.3). This supports the idea that small transients witness the continuous small-scale reorganization of the magnetic carpet, as revealed in EIT images. To understand the dynamics of the slow dynamic evolution process, Wu et al. (2000) have performed an MHD simulation of the formation and propagation of the plasma blobs observed in streamers. They found that plasma blobs are formed in small-scale reconnection processes among low-lying multipolar loops and their overlying coronal streamers. As such, they concluded that the blobs contribute to the evolution of the global scale magnetic field and feed plasma in the higher coronal structures and eventually in the solar wind. In our CACTus CME catalog, we find often small outflows prior to a ‘proper’ coronal mass ejection. At the same time many transients appear not to be accompanied by any larger expulsion of mass. This indicates that the eruption of a larger CME is not causally related to the occurrence of small coronal transients, but depends on pre-eruption conditions, like the amount of free energy or coronal helicity stored (e.g. Démoulin et al. 2002). For example, if the global structure contains a prominence, the prominence will erupt as part of the general loss of equilibrium. As such, these recurrent small blobs, being the result of local destabilization, can introduce a major instability that develops into a large-scale coronal mass ejection (Low 1984).

5.4.3 Apparent latitude of CMEs

The CME latitudes are obtained from the principal direction of CME eruption, assuming that CMEs propagate radially away from the source regions. This is not always the case. Cremades et al. (2004) showed that the CME trajectory is influenced by nearby coronal holes, causing a deflection in the trajectory before the CME is visible in the C2 field of view. A second effect is the projection onto the plane of the sky. This effect makes that

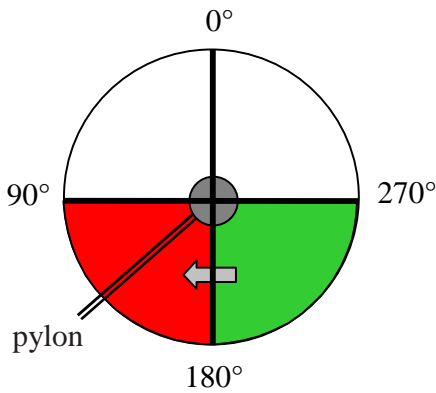


Figure 5.14: Cartoon illustrating the correction we applied to the latitudinal distributions. The angles indicated are the principal angles, according to convention running counter clockwise from solar north. The plot applies when SOHO is in its normal position. The pylon holding the occulter is then positioned in the south-east. The histogram in the red area is replaced with that from the green area.

measured CME latitudes are always an upper limit of the true direction of propagation.

In an attempt to deconvolve the latitudinal distributions from measurement effects, we study the latitudinal differences between the two catalogs, based on our 2 samples of common events. Fig. 5.13 (*right*) shows the histogram of absolute differences in latitudinal measurement. Interpreting these latitudinal differences in terms of measurement uncertainty, we can deduce that measurement errors of (at most) 10° and 20° apply respectively to 70% and 90% of the events for both samples. In the left figure we compare the latitudinal distributions for the two samples (CACTus results corresponds to the filled curve). The only peculiar difference is the peak at -10° latitude in the 1998 histogram (*upper left*). We verified the origin of this peak, but did not find a specific reason why CACTus would favour this latitude. All events in this peak, except one, differed less than 20° from the CDAW value. Hence, we conclude that, the CACTus-CDAW differences in apparent latitude of $\sim 10^\circ$ have no significant effect on the latitudinal distributions.

Fig. 5.15 (*top*) shows the latitudinal distribution for CACTus (red) and CDAW CMEs (blue) separated for each calendar year of LASCO observations. The C2 and C3 coronagraphs are both externally occulted. This means a circular occulting disk is placed in front of the entrance aperture (see Chapter 1 for more details). Hence, no direct sunlight falls into the instrument, reducing the stray light significantly. But, as a consequence, the region around the pylon holding the occulter has a smaller signal to noise ratio (this effect is clearly visible in any LASCO C3 image). As a consequence it is possible that less CMEs are detected along this direction. This creates a bias in the latitudinal histograms in the region around the pylon. The pylon always used to be directed to the south east. However, with the high gain antenna parked in a fixed position since the July 9th 2003, SOHO has to turn upside down during half of its halo orbit, in order to send data to Earth through the high gain antenna. The nominal roll switches between 0 and 180 degrees every 3 months. To remove this artificial bias from our statistics, we have corrected the latitudinal distributions in the south-east. Assuming that eastern and western statistics are similar, due to the Sun's rotation, we applied a correction function to the data, as illustrated in Fig. 5.14. Let θ be an angle running from 0° to 90° , and $N(\theta)$ the number of CME with principal angle θ , then, $N(90^\circ + \theta) \equiv N(270^\circ - \theta)$. We have applied this correction to the CACTus and CDAW datasets over the whole period.

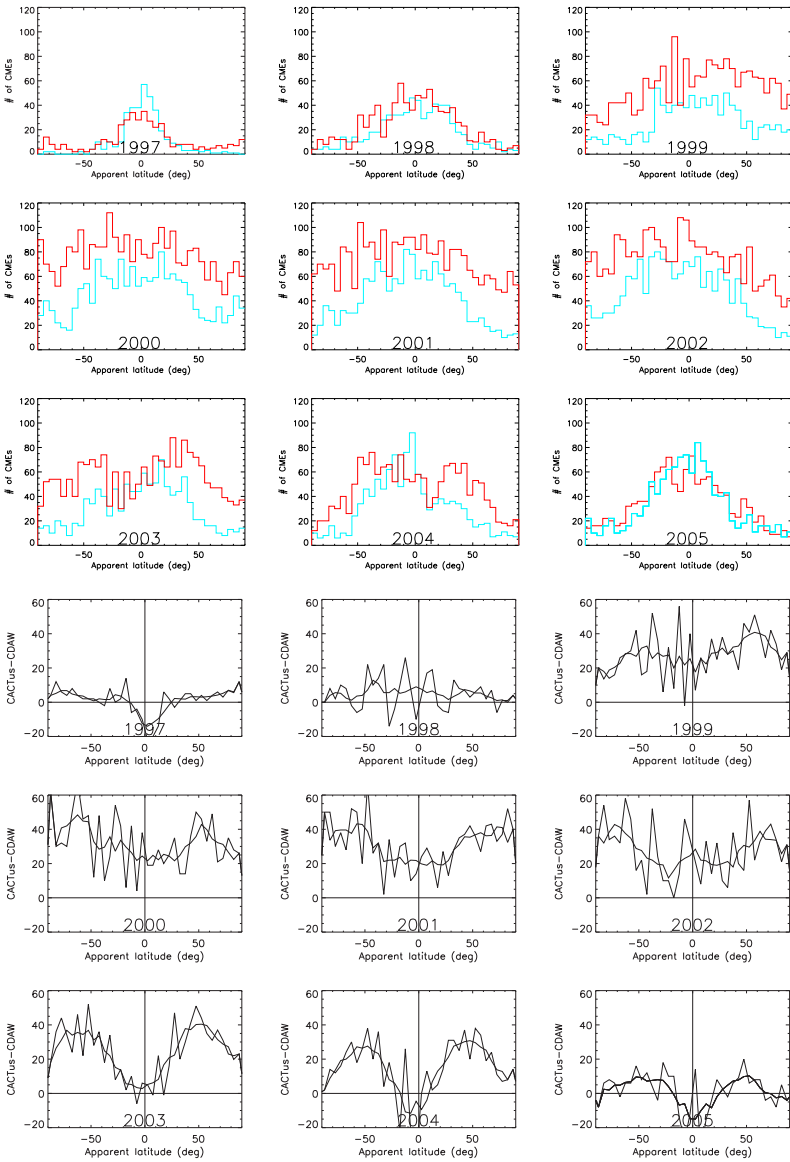


Figure 5.15: *Top*: Yearly histograms of apparent latitudes of coronal mass ejections. The latitudes run from 0 at the equator to ± 90 at the north/south pole. The CACTus distribution corresponds to the red curve, the CDAW distribution is represented by the light blue curve. *Bottom*: Difference of latitude histograms, the thick line is the smoothed curve. Positive values correspond to more CACTus CMEs.

Contrary to what was found for the CME widths (power law), the type of the latitudinal distribution does evolve with the solar cycle. During solar minimum years (1997, 1998 and 2005), the CMEs principal directions are distributed quasi-normally around the equator in the range $[-20,20]^\circ$. They are thus mainly connected to the ‘old’ active regions, since the new cycle regions appear at higher latitudes (around $\pm 40^\circ$). During solar active years, CMEs erupt almost uniformly at all latitudes, even at higher apparent latitudes (70°) in both hemispheres. The impression arises that the distribution is multi-modal during years of higher solar activity. These findings are consistent with earlier observations from past cycles (Hundhausen 1993, Howard et al. 1986) and earlier observations of current cycle Gopalswamy (2004b).

This is not a surprising result as it is generally accepted that CMEs erupt from closed field regions. Two types of magnetic configurations are possible on the solar sphere: open and closed. The open regions are linked to coronal holes and the position of the closed regions can be derived from the location of helmet streamers, visible in LASCO C2. Helmet streamers are positioned above the neutral lines. During solar minimum helmet streamers are located near the equator below 30° latitude. As the magnetic field becomes more complex towards solar maximum, the neutral line meanders over the solar sphere, reaching latitudes as high as 60° . Likewise, streamers are seen at all latitudes, an effect that is enhanced due to projection (as explained above).

According to the above paragraph there is a good correspondence between the global latitudinal properties of CMEs derived from CACTus and CDAW. However, there is a systematic difference. While analyzing the differences in CME width distribution between CACTus and CDAW, we discovered that the systematic higher CME rate, produced by CACTus, is mainly due to small events. Fig. 5.15 (*bottom half*) shows us where these extra events are coming from. In the ascending phase (1998-2002) the picture is unclear, the extra events seem to come from all directions. In the descending phase (2003-2005) however, the extra events are strongly restricted to two broad bands around ± 50 deg latitude, bordered by the polar coronal holes at the pole-side and by active regions at the equator-side. No extra events (or even a small deficiency) are observed in the CACTus output *in* the active region band ($<30^\circ$) as can be seen in Fig. 5.16. The fact that they are not just randomly distributed, but clearly structured, indicates they are driven by an underlying

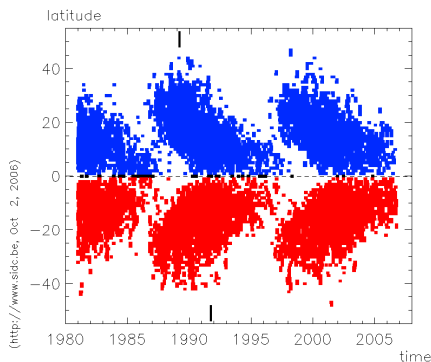


Figure 5.16: This ‘butterfly diagram’ shows the slow drift of the active regions on the disk from high to low latitudes during the solar cycle. [Image credit: SIDC, Royal Observatory of Belgium]

large-scale process. This process must be time dependent, or in other words, solar cycle dependent. CACTus has demonstrated that this region produces small events that are traditionally not recognized as ‘CMEs’, probably on morphological grounds, yet they are bright and outflowing, as required by the formal CME definition. Further research will be required to study this new subpopulation of CME-alikes and their precise source regions on the disc.

5.4.4 Apparent speed of CMEs

Finally, we give an overview of the speed measurements and distributions shown in Fig. 5.18. The CACTus CME speeds remain lognormally distributed, just like the CDAW speeds (e.g. Yurchyshyn et al. 2005). However, the CACTus CME speed distribution shows a much higher peak, which lies in the range 200-400 km/s.

In the validation section of the previous chapter (subsection 4.4) we have already pointed at the difference in CME speed measurement between the CDAW and the CACTus catalog. I recall that CACTus measures a speed profile as a function of the angle around the occulter, while the CDAW observer only tracks the fastest moving feature of the leading edge. Our CACTus software has revealed that for most CME events, several front speeds are distinguishable in the LASCO white light data and as a result, measuring only one speed is not sufficient to describe an event. In Fig. 5.17 we compare the speed measurement for the two samples of common events. At the left the two histograms are shown and at the right the difference CDAW-CACTus is plotted. For both periods, the difference curve is slightly skewed towards positive difference values inferring a higher CDAW speed is favored. During solar minimum a maximal uncertainty of 175 km/s applies for more than 80% of the events, during solar maximum the uncertainty is larger. This indicates that speed measurement is a difficult task and that CMEs have much speed variability, for example as a consequence of interaction with different background solar wind structures. In the discussion section we discuss different examples of speed measurements.

Our earlier hypothesis that CACTus (median) speeds are systematically lower than the CDAW speeds, is only supported by the speed histogram during solar max (Fig. 5.17, *bottom left*). Contrary to what might be expected, the majority of large speed-differences (CDAW-CACTus) occur for narrow CMEs. Possibly, this is because errors on individual measurements are averaged out better for more data points. The CACTus listed speed is the median of all measured speeds in the CME, the more data points, the more reliable this value is.

As example, we show two limb-CMEs (i.e. we verified that the source was located near the solar limb) in running difference and their speed-measurement in Fig. 5.19 (*top*). The radial speed profile measured by CACTus is shown in black and the CDAW speed is indicated with the black triangle. The velocity scale is indicated in black concentric circles in km/s. The CACTus speed profiles are quite uniform at the leading edge. For the majority of CMEs there is a large uncertainty on the speed measurement, simply because the ‘front’ of the outward moving feature is not clearly outlined. Even for the rather well observed front of the first CME (erupting to the NE) CACTus and CDAW linear speeds deviate still 100 km/s. The profiles are both distorted towards the edges of the CMEs, indicating that a CME is not a vast object propagating outwards. The magnetic

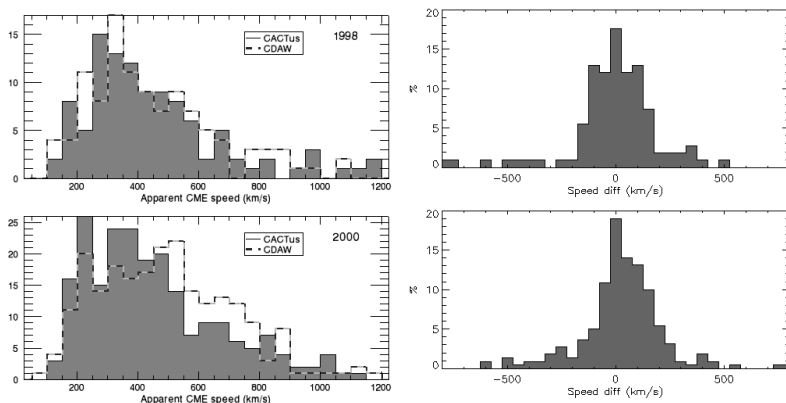


Figure 5.17: *Left*: CME speed distributions compared for both samples. The CACTus speeds correspond to the filled graph, the CDAW speed to the dashed line. *Right*: CDAW-CACTus speed differences.

and density structure of the ambient corona plays a not unimportant role in the outward evolution of CMEs (e.g. Jacobs et al. 2005) and vice versa. To illustrate this interaction, we have also plotted background subtracted images for these two events. For the first event (left) a pre- and a post-CME image are shown. It can be seen that the brightest streamer is shifted down due to the interaction with the CME. For the second event (right) we show a pre-CME image and an image containing the CME. The helmet streamer at the north was pushed aside during the event, but adapted its original position after the CME had left. The disturbance is traveling outward through the streamer, and the radial component of its speed is captured by CACTus.

5.5 Conclusion

We have compared the statistics of the CACTus CME catalog with that from the CDAW CME catalog, from September 1997 until December 2005 (Solar Cycle 23). In section 5.2 we have studied the CME rate and its evolution as compared to the sunspot cycle. The CACTus daily CME rate increased from 2.6 during solar minimum towards 7.5 during solar maximum and nearly half of them are narrow events (width $< 20^\circ$). The CACTus CME cycle lags behind the sunspot cycle with a delay of 6 to 12 months. Part of it can be explained by the eruption of polar crown filaments, which mark the boundary of the polar coronal holes. We believe however, that an additional mechanism is responsible for this time delay, since also significant time-delay has been observed for flare-rates. We support the idea that this time-delay reflects a lag between flux-injection (sunspot formation) and flux expulsion (magnetic energy release) in the corona. To estimate the uncertainty on the measured CME parameters we have compared these for a sample of 336 common events (i.e. present in both catalogs). We found that

- during solar maximum (minimum) around 77% (64%) of the events were detected

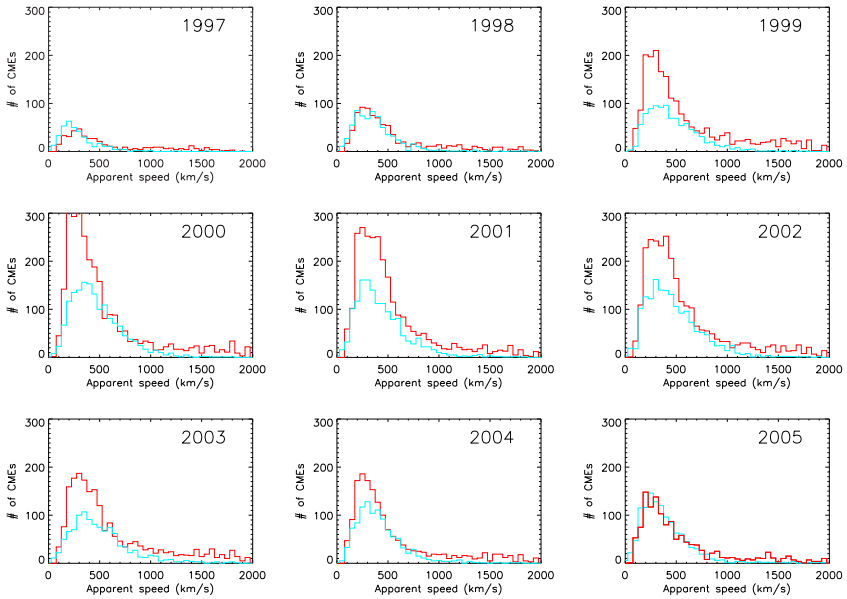


Figure 5.18: Yearly histograms of average radial speeds of coronal mass ejections. The speeds are derived from linear measurements and do not take into account acceleration or deceleration. We remind that we can only measure the speed component parallel to the plane of the sky. The CACTus distribution corresponds to the red curve, the CDAW distribution is represented by the blue curve.

within 23 minutes (~ 1 LASCO C2 image) of the CDAW detection.

- the CME width is only vaguely defined for coronagraphic images. This leads to a rather high uncertainty on the CME width parameter. Examples given in section 5.3 on the detection of shocks and halo CMEs are illustrative. Overall we can state that CACTus tends to measure the CMEs with smaller width as compared to CDAW.
- a maximal difference of 10° (20°) exists between CACTus and CDAW CME latitudes for 70% (90%) of the events.
- during solar minimum, a difference in velocity smaller than 175 km/s was measured for more than 80% of the events, during solar maximum the uncertainty is larger. Having said this, we recall that the CACTus and CDAW speeds have a different definition. Hence, care should be taken when comparing them.

We have observed significant differences in the CME parameters deduced from the CACTus CME catalog as compared to the CDAW CME catalog. We stress that these are not just a consequence of differently measuring the CME parameters, but mainly due to the inclusion of many small events which are discarded by the human observer.

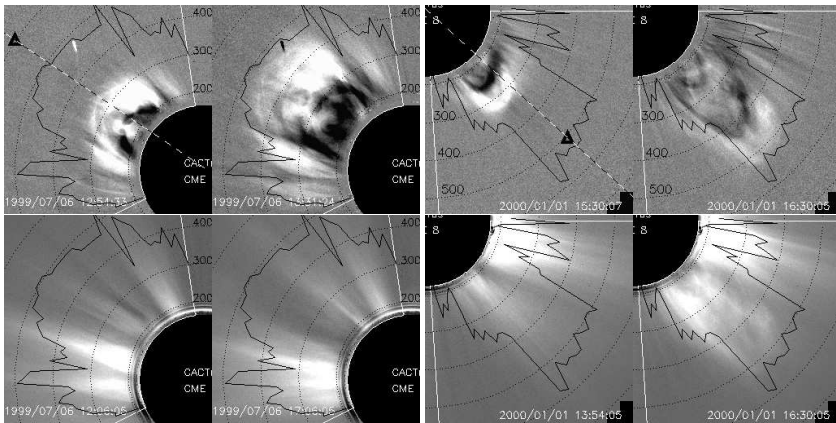


Figure 5.19: Illustration of two limb CME detections in running difference (top). The speed profile measured by CACTus is shown in black and the CDAW speed is indicated with the black triangle. The CACTus speed profile is quite uniform for both events. At the bottom we show background subtracted images. For the left event a pre- and a post-CME image are shown. It can be seen that the brightest streamer is shifted down due to the interaction with the CME. At the right we show a pre-CME image and an image containing the CME. The helmet streamer to the north had not changed position after the event, but the streamer was pushed aside during the event.

The CACTus CME widths reveal a power law distribution, with power around 1.6. This suggests that the CME process is scale-invariant, or in other words, that a ‘typical’ CME size, does not exist. For CMEs this is an important new result, but for other types of coronal magnetic field restructuring (e.g. flares) it is well-known. In the descending phase (2003-2005), the extra events are strongly restricted to two broad bands around $\pm 50^\circ$ latitude, bordered by the polar coronal holes at the pole-side and by active regions at the equator-side. CACTus has demonstrated that this region produces small events that are traditionally not recognized as ‘CMEs’, probably on morphological grounds, yet they are bright and outflowing, as required by the formal CME definition. Further research will be required to study this new subpopulation of CME-alikes and their precise source regions on the disc.

Chapter 6

Solar Image Processing and CMEs

Automated detection of solar features and events in general has gained increasing importance within the field of solar and space physics and it seems that this trend will be extended in the future. This new field is termed Solar Image Processing (SIP) and is the central subject of this chapter. At present an extensive set of automated recognition tools exists for a number of CME-related phenomena occurring in the lower corona. We review state-of-the-art techniques in a variety of data - disappearing filaments in $H\alpha$ images, dimmings and EIT waves in EUV images and erupting prominences in radio data - and discuss their possibility to deliver the CME parameters required for the space weather forecasting process. We believe that incorporating all automatically generated alerts into one CME report can provide valuable CME information, especially when no coronagraphic images are available. This chapter is thus a quest to reach a maximal success rate with the help of an integrated system of tools acting on a variety of data. The contents of this chapter is mainly based on the findings presented in Robbrecht and Berghmans (2005) and Robbrecht and Berghmans (2006).

6.1 Introduction

Coronal mass ejections (CMEs, e.g. Gopalswamy 2004a) are regarded as the solar events causing the most hazardous space weather conditions on earth (Gosling et al. 1990, Kahler 1992, Richardson et al. 2001, Zhukov 2004). They can trigger geomagnetic storms which affect the terrestrial communication and the reliability of power systems. Therefore good and reliable messages reporting on the occurrence of CMEs are an indispensable need for several communities vulnerable to space weather effects. The detection of CMEs has traditionally been addressed by visually checking coronagraph data for outward moving features. Such manual work is in fact quite successful: the human brain is an excellent pattern recognizer and a human operator is capable of intelligent interpretation of e.g. partially corrupted images. A lot of experience in observing CMEs and measuring its different characteristics is gathered at NASA's Goddard Space Flight Center. Since the launch of SOHO (Brueckner et al. 1995) CMEs have been tracked manually and reported on daily.

However, the Space Weather Community needs near-real-time alerts for (partial) halo CMEs, allowing sufficient time to run 3D MHD simulations to estimate their geoeffectiveness. This makes manual work labor intensive and thus costly. Moreover, with the advent of new coronagraphs onboard STEREO this would become a big strain on manpower. This realization stimulated the development of routines (available in the Solar Soft

Library) and software automating the different steps in the CME detection procedure. Automating the CME detection process is not easy, given their large variety in morphology and intensity. It requires objective criteria defining the CME. Following Hundhausen et al. (1984) and Schwenn (1995) coronal mass ejections are seen as *new discrete bright features with a radially outward velocity in a white-light coronagraph field of view*. In chapter 4 we discuss the validity and the limitations of this definition, showing especially that gusty outflows and other LASCO events can respect it, while not being proper CMEs. In addition to coronagraphs a wide variety of other instruments provide independent observations of CMEs, in regimes ranging from the chromosphere to interplanetary space. Hudson and Cliver (2001) have listed 18 important non-coronagraphic signatures of CMEs. More recently Hochedez et al. (2005) overviewed our current monitoring capabilities of solar events (including CMEs and associated events) in the perspective of space weather. At present a lot of observational evidence is gathered to allow the occurrence of some of these phenomena to be ‘a sufficient condition’ for CME initiation, not necessarily referring to the same structure as seen in white light. Hence in the attempt of breaking the waiting-time record (i.e. the time interval between the event and the alert) and developing the geomagnetic storm predictions, we can benefit from early manifestations of CMEs. The increasing power of computers and the advances in image processing and feature recognition made it possible to develop automatic detection techniques for these signatures. Among these associated features we discuss: disappearing filaments (observed in $H\alpha$ images), erupting prominences (seen in Radio data), EIT-waves and dimmings. Several advantages of including other instruments in the automatic detection scheme for CMEs are:

- When no coronagraphic data are available, CME warnings can still be sent out by using other instruments. Also ground-based instruments offer several advantages compared to space-borne instruments: faster data-transfer and thus faster detections; they offer a cheaper alternative. Ironically, space-borne instruments are subjected to the space weather that they are supposed to observe. Monitoring of halo CMEs with LASCO (Brueckner et al. 1995) for example, is often degraded by ‘snow storms’ of solar energetic particles originating from the same event on the sun. In such cases ground-based instruments can provide a valuable alternative source of information.
- Earth-directed CMEs are the most difficult to disentangle from coronagraphic images: they are very faint and involve a variety of transverse phenomena. Delannée et al. (2000) report on a study including 4 CMEs missed by the human observer. Only a comparison with the lower corona (on the disk or just above the limb) could indicate the existence of these CMEs. This illustrates the value of on-disk counterparts. Dimmings and coronal waves are among the best evidence of the large-scale reorganization of coronal magnetic fields associated with the onset of CMEs.
- The helicity of some CMEs can be derived from the chirality of the pre-eruption $H\alpha$ filament (Yurchyshyn et al. 2001). This is particularly important in forecasting the geoeffectiveness of the CME.
- Sometimes the associated phenomena precede the CME and are thus true precursors. In other cases, the observation of the associated phenomena (e.g. $H\alpha$ filament

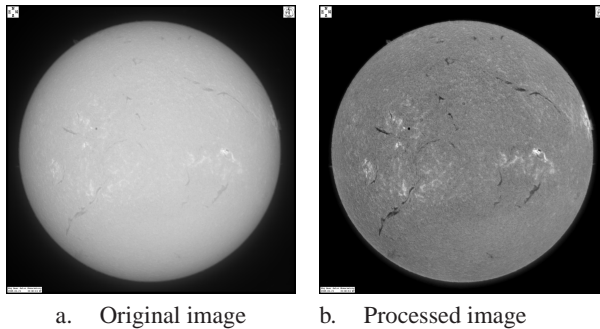


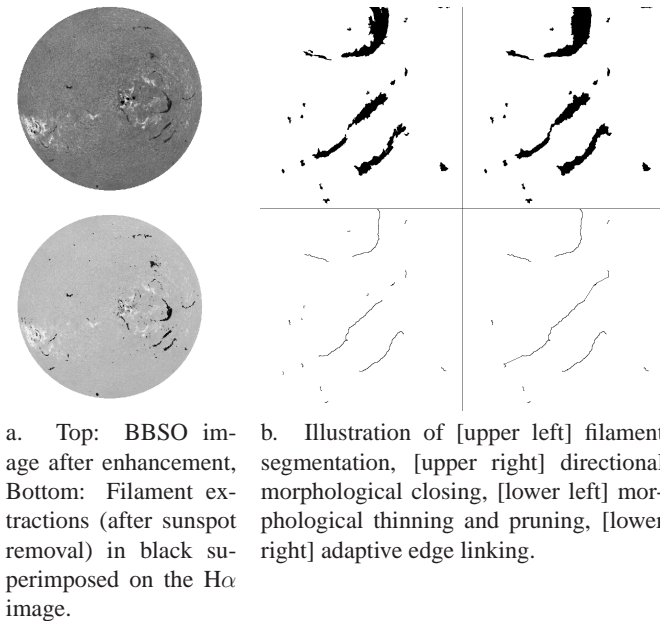
Figure 6.1: Example of an $H\alpha$ image from the Big Bear Solar Observatory (BBSO). Standard BBSO processing includes dark current and flat field correction, contrast enhancement and limb darkening removal. [Image credit: BBSO]

eruption) can be processed faster than coronagraphic images (e.g. because less images are needed for a detection). Observations of associated phenomena might thus improve greatly the timeliness of CME warnings.

Apart from the low-corona events mentioned above, several other phenomena can indicate the presence of a CME, the most important ones are radio type II bursts and long duration events (LDE). Radio type II bursts are already incorporated in the flare event list from SEC (Space Environment Center). A long duration ‘flare’ is the radiation send out by post eruption arcades, which form as a consequence of magnetic reconnection processes in the course of solar eruptions. According to a statistical study of Tripathi et al. (2004) it seems plausible to assume that post eruption arcades (PEA) are definite indicators of CMEs. For 98% of 236 selected events he has found an accompanied CME (or filament eruption). In space weather perspective they would thus complement superbly to the coronagraphic CME. Since the emphasis is on image recognition, we did not include these events in this paper. However, we believe that automatic alerts for these events would greatly enhance the ‘CME event list’.

6.2 Disappearing filaments in $H\alpha$ images

Filaments are formed along magnetic polarity inversion lines in evolving large-scale bipolar magnetic fields or in active regions. They may last for multiple days, changing their manifestation, but they vanish eventually. Not all filament disappearances have an associated CME. Quiescent filaments can disappear in two ways: thermally or dynamically. Mouradian et al. (1995) showed that only dynamical disappearances are associated with CMEs. Earth-directed CMEs do not always generate geomagnetic storms. The most important parameter deciding on this is B_z , the north-south component of the interplanetary magnetic field (IMF). Hence we are not only interested in detecting a CME, but also in defining its magnetic helicity (or that of the corresponding filament). Observational studies have pointed out that the helicity of a filament is closely related to its chirality, a geometrical concept defining the left-right handedness of an object. For filaments it can



a. Top: BBSO image after enhancement, Bottom: Filament extractions (after sunspot removal) in black superimposed on the $H\alpha$ image.

b. Illustration of [upper left] filament segmentation, [upper right] directional morphological closing, [lower left] morphological thinning and pruning, [lower right] adaptive edge linking.

Figure 6.2: The left images illustrate a filament segmentation method based on edge-detection using the Sobel operator (Qu et al.). The right panel shows the result of additional processing after segmentation. After morphological closing operations they track the filament spines which are then linked when belonging to the same filament body. The decision criterion for linking is based on pixel-distance and direction of the filament spines. [Image credit: Ming Qu]

be determined using the orientation of ‘barbs’ (these are small appendices) relative to the filament’s main axis (Pevtsov et al. 2003). Filaments are located in the corona, but are much cooler and hence much denser than its surrounding. They are best observed in $H\alpha$ images ($\lambda = 656.6$ nm). Because they absorb most emission from below they appear as dark ribbons against the bright solar disk.

Prior to any feature recognition, the images need to be preprocessed (Zharkova et al. 2003). Big Bear Solar Observatory (BBSO, California) standard *preprocessing*, for example, includes dark current and flat field correction, contrast enhancement and limb darkening removal. A BBSO processed image is shown in Fig. 6.1. To avoid limb darkening some methods (like Bernasconi and Rust 2004) only accept filaments within a cone of 60° of the sun center.

The most difficult part of filament tracking is its separation from the background, this is called *image segmentation*. The two main characteristics describing filaments are: (1) They are dark and thus can be separated from the background using a darkness threshold. (2) the majority of the filaments have a long elongated shape. In a first step the threshold defines seeds, which are then extended using region growing techniques to obtain the full



Figure 6.3: Example of a filament detection by Bernasconi & Rust, indicating the spine and barbs. Next to each barb is a letter indicating whether it is left-bearing (L), right-bearing (R) or undetermined (?). This filament was located in the southern hemisphere of the Sun. Since this filament has more left-bearing barbs than right-bearing ones, the code determines its chirality as "right-handed". It means that the magnetic flux rope in which it is embedded has a right-handed twist (helicity). [Image credit: P. Bernasconi]

filament. Roughly there are two types of *automatic thresholding*: global thresholding, based on the median intensity of the entire image (e.g. Gao et al. 2002) and local thresholding, where the threshold is calculated per pixel, depending on a small area centered at this pixel (Shih and Kowalski 2003). Methods which first *enhance the contrast* of the filament structures before thresholding are proven to be more successful. Shih and Kowalski (2003) introduced a directional morphological filter to enhance only the filament structures (this uses an 11×11 square with linear structuring elements like horizontal, vertical and diagonal lines). Fuller and Abouadarham (2004) don't make any postulate about the features shapes, they want to extract the most complete set of filaments. They contrast the filament contours by subtracting a Laplacian filtered version of the image from the original image. Recently Qu et al. (2005) proposed a new algorithm for automatic thresholding from the result of edge detection using the Sobel operator. For an illustration of Qu's improved method see Fig. 6.2.

Sunspots, also dark solar features, can be misinterpreted as filaments. Since sunspots are usually darker than filaments Shih and Kowalski (2003) simply apply a global threshold with a level below the usual filament brightness threshold. However, in a comparative study based on a data-set of 50 images between January 1999 and September 2004, Qu et al. (2005) report only a success rate of 60% for this method. They propose a new and efficient feature-based classifier called the Support Vector Machine (SVM), to distinguish sunspots from filaments. Applied on the same data-set they recover 94% of the classified sunspots. It is the first time that SVM is applied for sunspot detection.

After thresholding, the result is a black-and-white image with the black features indicating the filaments. A 'cleaning closing' operation is applied to eliminate small lines which are actually not part of a filament. The dark features then obtained are used as seeds for a *region growing* operation. In a last step small filament parts should be connected if they belong to the same filament body. This can be done using region growing techniques (Gao et al. 2002, Shih and Kowalski 2003, Fuller and Abouadarham 2004). The more advanced methods connect filament parts based on the orientation and distance of spines (Bernasconi and Rust 2004, Qu et al. 2005). A spine marks the skeleton of the filament and is defined by vertices which are calculated in an iterative process. Besides

the spine Bernasconi and Rust (2004) also define the orientation of the barbs. The latter is done to determine the chirality of the filament which is strongly related to its helicity. Barbs are small appendices at the left and right of the filament spine. The spine and barbs are illustrated in Fig. 6.3.

In the quest for CME-precursors, we are actually interested in filament-disappearances indicating the filament has possibly erupted. Gao et al. (2002) already send out alerts in near-real-time when a disappearing filament is found. Also Qu et al. (2005) and Bernasconi and Rust (2004) track the detected filaments in time.

6.3 Dimmings and EIT waves

After the discovery of the so-called ‘EIT wave’ phenomenon (Thompson et al. 1998) it was soon suggested that these waves are strongly associated with CMEs (Plunkett et al. 1998). Later, a statistical study of 173 EIT wave events in the period between March 1997 and June 1998 by Biesecker et al. (2002) confirmed this association unambiguously. Behind an EIT wave a dimming is usually observed and is most likely due to the evacuation of mass (Thompson et al. 1998, Harra and Sterling 2001).

Detecting EIT waves is a hard problem of feature recognition given their (1) large variety in physical appearance, (2) their weak intensity variation and (3) the fact that with the current instrumentation (the default EIT 195 cadence is 12 minutes) these events are strongly under-sampled: typically only 3 images are obtained of these highly dynamic events that last up till an hour and might cover the complete solar disc. A proof-of-principle demonstration for an automated detector is presented by Podladchikova and Berghmans (2005). To by-pass the first problem, the detection of the *occurrence* is done without using the spatial information in the images. Instead the detection is based on the characteristics of the histogram-distribution of rebinned (256×256 pixels) difference images. The average value of this distribution is typically close to zero. However, since EIT waves and dimmings are relatively large events disturbing a large number of pixels, they do clearly show up (Fig. 6.4) in the higher order moments of the distribution (variance, skewness and kurtosis). Once the occurrence of an event has been detected, the next step is to determine its location, structure and size. Two groups of pixels are collected for this: a maximal and a minimal pixelmap. The minimal pixelmap is constructed by selecting all pixels in the difference image below a very restrictive (i.e. low) threshold: these pixels belong, by assumption, to the dimming. However a certain fraction of the dimming, typically the weaker edges, is missed in the minimal pixelmap. The maximal pixelmap is constructed by selecting all pixels in the difference image below a weak (i.e. relatively high) threshold. All the pixels corresponding to the dimming area are contained in the maximal pixelmap, but typically much more than the dimming region is selected. To filter out phenomena not connected to the dimming region, one uses the pixels in the minimal pixelmap as seeds for a region-growing method. The region-growing is however restricted to pixels from the maximal pixelmap. The method shows very promising result on a clear test-case (solar minimum situation) but remains to be proven in a complex solar maximum situation.

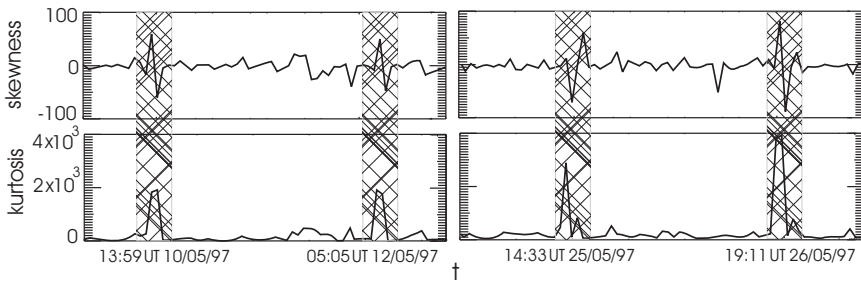


Figure 6.4: Illustration of 4 EIT wave and dimming signatures in May 1997. The upper panel plots the skewness (or asymmetry) of the difference images versus time, the lower panel shows the kurtosis (sharpness of the peak). [Image credit: Olena Podladchikova]

6.4 Erupting prominences in radio images

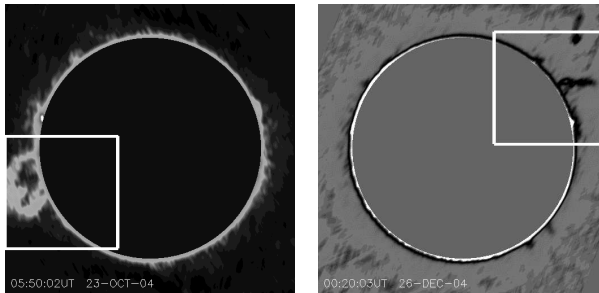


Figure 6.5: Two limb events visible in Radio images produced by the Nobeyama Radio-heliograph. A white squares indicates the detection of a limb event. [Image credit: Nobeyama]

Unique observations of solar eruptions are acquired with the Nobeyama Radio-heliograph- NoRH Nakajima et al. (1995) at the National Astronomical Observatory of Japan since April, 1992. During the daily 8-hours of observations, full disk solar images are produced at the 17 GHz and 34 GHz radio frequencies. In what follows we only consider the 17 GHz images which have a spatial resolution of 15 arcsec. The temporal cadence used for automated detection is 10 min.

An operational tool was developed that detects the so-called limb-events, including mostly prominence eruptions but also prominence activity and limb flares. The tool searches for pixels that are at least six times brighter than the daily average brightness. The center of gravity of these selected pixels is calculated. If this center of gravity is off-disc and if the corresponding structure persists in at least 3 consecutive images (lifetime > 30 min) then the structure is defined as an event. Out of the 226 events detected between January 1996 and December 2001, 186 had simultaneous data coverage from SOHO/LASCO. 134 of these (72%) could be linked with coronal mass ejections observed

by SOHO/LASCO Gopalswamy et al. (2003). Two illustrations of such limb events are shown in Fig. 6.5. The limb-detection method is known to typically miss events that are either very slow (daily average is then biased by the event itself) or very fast (spending less than 30 min in the field of view). Also weak events cannot be detected and two simultaneous events might have a joint center of mass that is on the disc. The results are distributed via the web (<http://solar.nro.nao.ac.jp/norh/html/prominence/>) in near real time.

6.5 CMEs in coronagraphic white light images

In Chapter 4 we have described the CACTus software, which we have developed to automatically detect CMEs in LASCO data. Our technique is based on height-time maps, introduced by Sheeley et al. (1999). Instead of making morphology assumptions, our technique essentially detects bright features moving radially outward along radial directions. Outward motion is thus a necessary condition for detection. Following the example of CACTus, other automated CME detection algorithms applicable to LASCO data have emerged during the last two years.

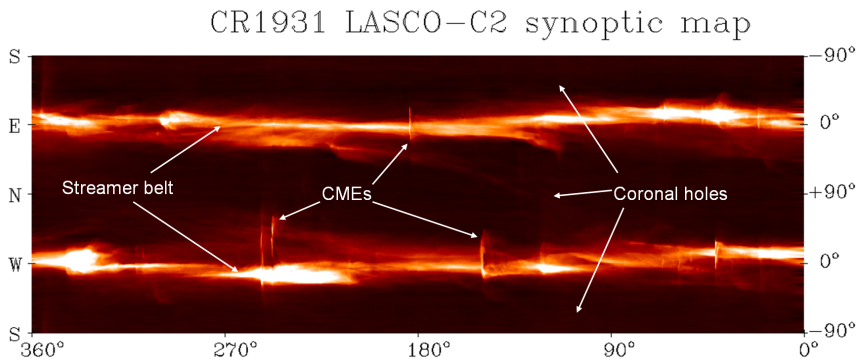


Figure 6.6: An example of a LASCO-C2 synoptic map at $3 R_{\odot}$ corresponding to Carrington rotation 1931. These maps serve as input for the ARTEMIS detection algorithm. [Image credit: Yannick Boursier]

Boursier et al. (2005) have developed ARTEMIS, a method for detecting CMEs in electron density synoptic maps computed from LASCO C2 images. These maps (see Fig. 6.6) are a convenient way of globally displaying the coronal evolution over a solar rotation (27 days). They are constructed from sequential LASCO C2 images by extracting circular rings at a given radial distance from the center of the Sun and stacking them vertically side by side. In this way, a map arises with the same dimensions as the CACTus output map, i.e. $[\theta, \text{time}]$, where θ runs from 0 to 360° around the occulter and time spans 27 days. On these synoptic maps coronal mass ejections appear as narrow streaks, elongated in the direction of θ , just as on the CACTus output maps. Three different filters have been tested to extract the elongated features. For a test sample of 49 CMEs, a median

filter gave the best CME detection rate. The method can return the time of appearance, the intensity, the principal angle and the angular extent of each detected CME. A preliminary comparison of the ARTEMIS output with the CDAW and CACTus CME catalogs during the period 1998-1999 reveals a detection rate comparable to the CACTus CME rate during solar active times. Similarly to the results from our statistical analysis (chapter 5, section 5.4), CACTus reports a lower CME rate during periods of lower activity as compared to ARTEMIS. In the case of CACTus, we attributed this lower detection rate during solar minimum to lower average intensities of the running difference images.

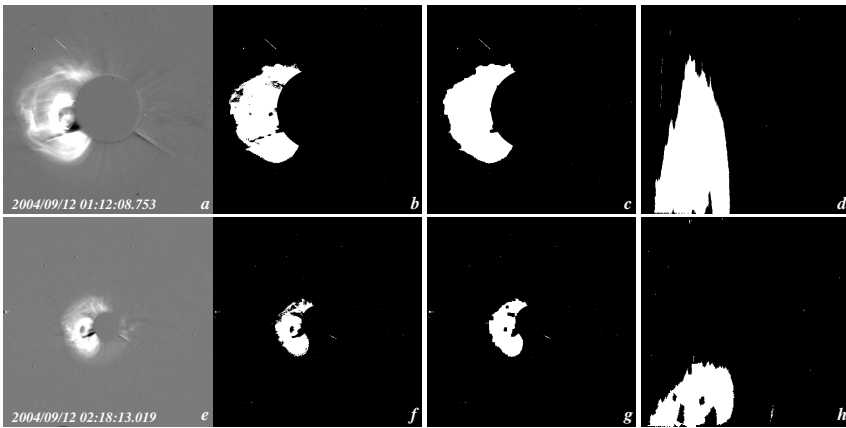


Figure 6.7: Illustration of the CME detection algorithm developed by Qu et al. (2006) which is based on direct detection of the CME in the LASCO C2 and C3 images. (a) & (e): running difference image, (b) & (f): binary segmented result, (c) & (g) result after morphological closing, (d) & (h) result in polar coordinates. [Image credit: Ming Qu]

Qu et al. (2006) detect CMEs directly in running difference images by applying a segmentation technique with variable intensity threshold. The method is illustrated in Fig. 6.7. To overcome the problem of missing faint CMEs in the vicinity of bright CMEs a ‘partial division image’ is constructed, based on the brightness ratio between the image and a reference image. The thresholding method produces binary images in which the CME candidate pixels are labeled “1”. A morphological closing operation is then performed to eliminate small gaps, merge detections which are spatially close and remove noise detections. After this, the CME candidates are accepted as CME if they appear in at least two consecutive images and if their centers of mass deviate less than a given threshold, depending on the image cadence. Using a set of 6 CME parameters, an automated system classifies the detections into strong, medium and weak CMEs according to Howard et al. (1985).

A similar detection algorithm, SEEDS, is developed by Olmedo et al. (2005) and shown in Fig. 6.8. Their Solar Eruptive Event Detection System detects CMEs in polar

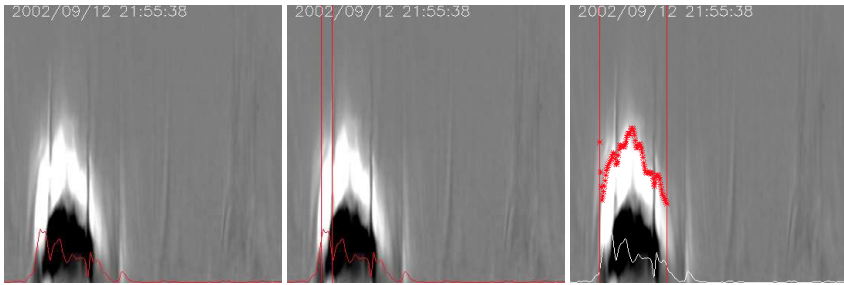


Figure 6.8: Illustration of the SEEDS CME detection algorithm. The result of preprocessing is a normalized running difference image, transformed to polar coordinates. *Left*: The images intensity is integrated in the vertical (r) direction and represented by the red line, *Middle*: Outstanding bright regions are labeled as CME cores, *Right*: Region growing and threshold segmentation determine the size of the CME. [Image credit: Oscar Olmedo]

transformed running difference images constructed from LASCO C2. Per polar image a 1D brightness profile is constructed by simply integrating the image intensity along the r direction. Outstanding bright regions, showing a peak in the brightness profile above a given threshold, are labeled as CME cores. Hereafter, the CME region grows by performing threshold segmentation techniques in the polar image and opening and closing operations are applied to merge or remove small detections. Next, a time-dependent causal filter is applied for tracking and locating the features in time sequences. Trailing blobs are removed from the detection. The detected events are then sent through a machine learning algorithm where they are classified. The method has been applied on a 12 month period of LASCO C2 data (2002). About 75% more events have been detected compared with the CDAW CME catalog, but only 62% of CACTus CME rate was retrieved during this period. This comparison is NOT performed on an event-per-event basis, but it regards the global CME rate. This lower rate can be partly explained by the removal of trailing blobs in SEEDS.

A totally different approach is adopted by Colaninno and Vourlidas (2006), who provide velocity maps by applying an optical flow method on density maps (in cartesian coordinates) derived from the LASCO C2 images. Optical flow methods are used on coronal EUV and solar granulation observations by Gissot and Hochedez (2007) to estimate intensity and velocity variations. Application of this technique on coronagraphic data for CME detection is still in an infant stage. Tests on nine well defined CME structures observed in high cadence LASCO C2 data give promising results. The method adopts a constant brightness approximation; every change in intensity is assumed to be caused by mass motion. This is a severe limitation for velocity estimation in the corona, where CMEs do have intrinsic brightness variations. Other limitations are the need for a higher than nominal cadence for successful optical flow estimation (nominal cadence is 24 minutes for C2) and CMEs with diffuse and irregular shapes are difficult to sample. So, while this method is leading the way for detailed CME velocity measurements, it is still far from being an ‘automated CME detection algorithm’.

6.6 Discussion

While a lot of the physics of coronal mass ejections remains unknown, some basic understanding exists on the link of CMEs with related phenomena. Instead of restricting the CME definition to its direct appearance as a bright moving plasma cloud as observed by a coronagraph (Hundhausen 1993), it can be seen as a complex reorganization of the solar corona involving other solar phenomena such as prominence/filament activation and eruptions, flares, dimmings and EIT waves. It has become clear also, that some of the characteristics of these other phenomena contain information on the geoeffectiveness of the associated CMEs. For example the chirality of the pre-eruption filaments is strongly related to the magnetic helicity of the magnetic flux rope of a CME at L1 (Yurchyshyn et al. 2001). At the same time, CMEs are not merely a scientific object anymore. As one of the main drivers of geomagnetic storms, they have become a reference object to be monitored for space weather operations. ‘CME observation’ is thus experiencing a transition from research to operations and this brings new requirements on their observation on the level of timeliness, objectiveness and completeness.

The concept ‘coronal mass ejection’ exists thus in several contexts (theoretical versus observational, high versus low coronal observation, etc.) and thus needs to be defined according to its framework. The conceptual CME models, briefly reviewed in chapter 4, are very useful for physical understanding, but useless *as such* in observational context. A translation into measurable parameters is required. The observational definition depends also on the detection method. In the previous section we have discussed four different approaches apart from our own method for CME detection in LASCO data. The SEED method, using direct segmentation in the LASCO images, imposes a different definition compared to CACTus or to the ARTEMIS method which detects CMEs in synoptic maps. These different approaches do not contradict the current physical insights and, although they are very different, they can co-exist and even complement each other. Every new method of CME detection leads to a new set of parameters describing a CME event. This leads to a number of catalogues treating the same data, but interpreted differently. Although the above described algorithms for LASCO CME detection are still in development, clear discrepancies arise. For example the inclusion of faint and small events and the merging of several parts into one CME leads to catalogs with highly deviating CME rates. We mention that the same applies to e.g. flare detection in GOES time series. At some level it is arbitrary to discriminate a small flare against the background baseline (Veronig et al. 2004). For example, the question whether trailing blobs behind a large eruption should be separately ‘counted’ or not is answered differently in each method. As a consequence it is difficult to cross-correlate different catalogs. New born initiatives on standardizing output parameters are valuable in this respect.

SIP requirements diverge according to the field of application. For example, for operational space weather purposes, the real-time efficiency of the algorithm is very important. The same applies to real-time simulations. Also thresholds can be set such that only space weather relevant CMEs are detected. A forecaster is not interested in small tiny events, but the scientist studying the CME initiation process or CME precursors might be interested. Further, the selection of measured parameters is again a function of application. For example, to reliably predict whether the Earth will pass through the CME trajectory or not, we need to estimate the direction and cone of influence of the CME and its asso-

ciated shock. These parameters contain still large uncertainties, simply because we lack the required input data. New STEREO data is expected to advance the 3D understanding of CMEs. Another important parameter to predict the geomagnetic response to the CME event is the magnetic configuration. Instead of delivering a user end product, SIP can also provide input data for real-time simulations. For example, the ‘Wang-Sheeley-Arge model’ (Wang and Sheeley 1992, Arge and Pizzo 2000) forecasts the background solar wind up to 1 AU by extrapolating the photospheric magnetic field into the heliosphere using the potential field source surface (PFSS) model (Schatten et al. 1969, Altschuler and Newkirk 1969).

Solar image processing is expected to facilitate the treatment of large data sets used for observational analysis on event basis or via a statistical approach. Huge amounts of data will be available thanks to the technical advancements. However, a profusion of data needs intelligent meta data, to help separating ‘the wheat from the chaff’. An important part of it can be provided by automated algorithms pre-digesting the data, like the ones described in this chapter. Some caveats have to be noticed here regarding the biases of automated detection. Therefore the algorithms must be tested and their results should be verified with comparable output. For example, the statistical study reported in chapter 5 raises the issue that the CACTus performance itself could be a (weak) function of the solar cycle. For event studies this is not such a problem, but it can introduce important biases when using a statistical approach. Standardization of output and cross correlating catalogs can be helpful ways to discover systematic errors. At this moment various algorithms are either up an running (e.g. NJIT’s filament disappearance detector, the Nobeyama limb event detector, CACTus for CME detection) or under development (other filament detectors, EIT wave detector). New techniques for the estimation of the helicity based on vector magnetogram data offer a great potential for *forecasting* CMEs (e.g. Pariat et al. 2006). In a next step the output of these routines should be gathered into databases. Internet technologies such as the various grid efforts (EGSO, Bentley (2002); VSO, Davey et al. (2003); coSEC, Hurlburt et al. (2004)) might make this possible. As a preparation for the massive data flow expected from the Solar Dynamics Observatory, automated, autonomous feature-event recognition algorithms are currently in development. The various outputs will then be mined to a ‘Solar Event Database (SED)’, containing, besides the usual parameters, also meta-data on the detected events and features.

Summary and Conclusions

In this dissertation we described two aspects of solar coronal dynamics: waves in coronal loops (Part I) and coronal mass ejections (Part II). We investigated the influence of (semi-) automated techniques on solar coronal research. This is a timely discussion since the observation of solar phenomena is transitioning from manual detection to ‘Solar Image Processing’. Our results are mainly based on images from the Extreme UV Imaging Telescope (EIT) and the Large Angle and Spectrometric Coronagraph (LASCO), two instruments onboard the satellite SOHO of which we recently celebrated its 11th anniversary. The high quality of the images together with the long timespan created a valuable database for solar physics research.

Part I reported on the first detection of slow magnetoacoustic waves in coronal loops observed in high cadence image sequences simultaneously produced by EIT and TRACE. These two instruments observe the hot corona in extreme UV emission lines. TRACE achieved a 25 sec image cadence in the Fe IX (171 Å) bandpass while EIT achieved a 15 sec cadence in the Fe XII (195 Å) bandpass. These multi-wavelength observations have revealed the existence of weak transients in extended coronal loop systems. The disturbances originate from small scale brightenings at the footpoints of the loops and propagate along the loops. By explaining the difference of the measured speeds with the sound speed as a projection effect we suggested that these weak transients are magnetoacoustic waves. The appearance of waves traveling at different speeds in the same loop, could point at sharp temperature gradients across these loops. A realistic loop model should be applied to verify this conclusion.

Part II addressed the question of detecting coronal mass ejections in coronagraphic white light data. CMEs are routinely detected by visual inspection and event catalogs are assembled. **As an alternative, we have developed a software package called CACTus (‘computer Aided CME Tracking’) to test the feasibility of automating the CME detection process.** Automated processing of solar data can produce meta-data which is useful for both, solar research and space weather forecasting. CACTus is exploited in two independent ways. It digests near-real-time LASCO images and characterises the most recent CMEs by listing their important parameters. Secondly, we have generated the first ‘objective’ LASCO CME catalog, a result of the large scale application of the CACTus software on the LASCO archive. The real-time output of the program as well as the catalog are freely available on the web (www.sidc.be/cactus).

Using our catalog, we have studied the CME characteristics over the solar cycle and compared them statistically with similar results obtained by manual detection. Significant differences are observed in the CME parameters. CACTus has detected twice as much CME events as the manually assembled catalog. The extra events are mainly narrow events. The parameter describing the angular extent of a CME follows a power-law

distribution with power close to 1.6. This means that a typical CME-size does not exist, but instead that a whole range of CMEs is present. **This very new result triggers the question of CME definition.** This discussion is analogous to the recent discussion on the definition of ‘planet’. Before the discoveries of the early 21st century, astronomers hadn’t really needed a formal definition for planets. Due to better observation capabilities however, more and more Pluto-alike bodies have been discovered. A recent debate led to a new definition specifying the necessary conditions for celestial bodies to be planets. As a consequence Pluto had to be reclassified from ‘planet’ to ‘dwarf-planet’. Analogously, high quality images of LASCO show many more events than originally thought of when speaking of CMEs. With our automated software we have shown that they obey the original CME definition and thus that they should be added to the list of CMEs. A deeper study on their origin and driving force is needed to either confirm their status as CME or reclassify them as a different type of events. In case of the second option, the CME definition should be adapted likewise.

In this work we have shown the importance of new techniques and automated methods to improve our understanding of coronal dynamics. They offer an objective approach and make it possible to treat large amounts of data. Analysing large data sets is interesting because they allow a statistical approach to problems. Additionally, new image processing techniques can perform certain analysis which is not possible otherwise. For example, optical flow techniques (applied in Part I) would make it possible to trace loops while moving due to spatial oscillations.

Appendix A

The effect of a sound wave on spectral line profiles

Eriksen and Maltby (1967) have studied the effect of propagating sound waves on the profiles of spectral lines. They found that, although there is no net mass motion, propagating compressive waves will cause spectral line asymmetries and line shifts in the direction of wave propagation. This theory was developed to explain the net redshift (downflow) observed in the transition region, coming from compressive waves originating in the corona and propagating down through the transition region.

Consider a pure sound wave propagating through a gas.

1. The wave equation for a pure sound wave is:

$$\omega^2 \mathbf{v}_1 = c_s^2 \mathbf{k}(\mathbf{k} \cdot \mathbf{v}_1). \quad (\text{A.1})$$

These waves are longitudinal, in the sense that according to the above equation the velocity perturbation (\mathbf{v}_1) is *in the direction of propagation* (\mathbf{k}). (Priest, page 157)

2. Consider now a sinusoidal propagating sound wave with wave frequency ω propagating along the loop in the z -direction towards the observer along the line of sight. Since a sound wave is a travelling compression region, this can be expressed in terms of a (gas) pressure variation

$$\Delta p = p - p_0 = \Delta p_m \sin(\omega t - k_\lambda z) \quad (\text{A.2})$$

where p_0 is the unperturbed value of the gas pressure and Δp_m is the amplitude of the pressure perturbation. In addition to the thermal motion, the particles will move with a velocity $v = v_z$, varying in phase with the pressure perturbation Δp . The velocity v given to the atoms by the wave implies that the atoms emit radiation at Doppler shifted wavelength

$$\lambda' = \lambda_0 \left(1 + \frac{v}{c}\right). \quad (\text{A.3})$$

The shift in wavelength introduced by the wave is can be (after calculation) also be expressed as a function of the pressure enhancement (adopted from Erikson and Maltby, 1967)

$$\lambda' - \lambda_0 = \left[\frac{A}{2\mu\gamma} \right]^{1/2} \Delta\lambda_D \frac{\Delta p}{p_0}, \quad (\text{A.4})$$

where A is the atomic weight and μ the average molecular weight. $\Delta\lambda_D$ is the doppler width of the line and p_0 the unperturbed value of the gas pressure. According to this equation heavier elements show a reasonable wavelength shift as A/μ may be large.

3. The sound wave causes not only pressure, but (of course) also temperature and density to change with time. We find

$$\frac{v}{c_s} = \frac{\Delta\rho}{\rho_0} = \frac{\Delta T}{T_0} = \frac{\Delta p}{\gamma p_0}, \quad (\text{A.5})$$

with c_s the speed of sound. After calculation, we find that indeed, the number of atoms $n_{r,s}$ capable of forming the emission line (by a transition from the level r , s where s is the level of excitation and r the number of times the atom is ionised) is again a function of the change in pressure $\Delta p/p_0$. In other words, the blue (or red) doppler shifted atoms emit more (or less) than when at rest. Differently stated $n_{r,s}$ may thus be expressed as a function of the wavelength shift $\lambda' - \lambda_0$, for a given value of the pressure amplitude $\Delta p/p_0$.

Conclusion

The phase relation between the density and velocity perturbation which causes the line *intensity* to vary with the line-of-sight velocity, leads to a net shift of the spectral line if we integrate over a wave period.

Appendix B

Comparative table of a CACTus and CDAW output

In the table below, the CACTus output is listed combined with the corresponding CDAW outputs, as could be found on http://cdaw.gsfc.nasa.gov/CME_list at the time of writing. The different outputs given by CACTus are:

- cmenr : cme identification number
- t_0^* : onset time, earliest indication of liftoff
- dt_0 : duration of liftoff (hours)
- pa^* : central axis, counterclockwise from north (degrees)
- da^* : angular width (degrees)
- v^* : median velocity (km/s)
- dv: variation of velocity over the width of the CME
- minv: lowest velocity detected within the CME
- maxv: highest velocity detected within the CME

The values for which we have found a corresponding measurement from the CDAW catalog are indicated with a '*'. The CDAW speed mentioned is the linear fit. The last column 'Q' indicates the quality_index of the catalog running from 1 to 5, meaning 1: poor, 2: fair, 3: typical, 4: good, 5: Excellent. A CME is indicated as 'marginal case', when the CME signal doesn't exceed the desired threshold (2σ) above the background.

B Comparative table of a CACTus and CDAW output

cmenr	t ₀	dt ₀	pa	da	v	dv	minv	maxv	catalog t ₀	pa	da	v	Q
0001	marginal case	02	234	024	0416	0722	0390	2101	2003/11/09 02:30:05	232	35	75	2
0002	2003/11/09 04:30	02	219	026	0372	0047	0286	0446					
0003	2003/11/09 06:06	03	226	036	1041	0624	0208	2174					
0004	2003/11/09 06:30	03	086	212	1041	0483	0440	2083	2003/11/09 06:30:05	Halo	360	2008	4
0005	2003/11/09 07:31	00	320	032	0637	0046	0578	0744					
0006	2003/11/09 09:30	05	225	038	0496	0642	0211	1743					
0007	marginal case	03	104	068	0489	0235	0195	1177					
0008	2003/11/09 15:06	01	104	024	0440	0147	0220	0725					
0009	2003/11/09 16:54	02	292	012	0400	0035	0343	0427	2003/11/09 17:06:05	290	15	639	1
0010	2003/11/10 02:06	07	226	044	0248	0033	0192	0315					
0011	2003/11/10 16:54	03	047	038	0428	0063	0276	0548	2003/11/10 16:54:05	55	43	478	2
0012	2003/11/11 00:06	01	240	028	0529	0101	0303	0625	2003/11/11 00:06:29	235	40	553	3
0013	marginal case	01	222	012	0844	0565	0664	1852					
0014	2003/11/11 02:30	08	270	300	0947	0374	0312	2083	2003/11/11 02:30:07	Halo	360	1359	5
0015	marginal case	00	105	014	0833	0056	0762	0946					
0016	2003/11/11 03:30	01	062	012	1633	0511	0744	2403					
0017	2003/11/11 04:06	00	356	020	0393	0775	0252	2065					
0018	2003/11/11 05:54	03	104	072	0919	0408	0343	1953	2003/11/11 05:54:05	118	52	1445	3
0019	2003/11/11 06:06	01	051	038	0933	0493	0306	1838					
0020	2003/11/11 06:30	00	026	020	0889	0387	0212	1630					
0021	2003/11/11 10:06	01	204	016	0395	0067	0269	0496					
0022	2003/11/11 13:54	05	265	150	1041	0245	0558	1366	2003/11/11 13:54:05	Halo	360	1315	3
0023	2003/11/11 15:54	02	090	196	0993	0468	0231	2232	2003/11/11 15:54:05	87	128	1785	3
0024	2003/11/11 20:06	01	102	012	0505	0440	0306	1562					
0025	2003/11/11 21:54	02	110	048	1009	0431	0504	1953					
0026	marginal case	01	108	020	0549	0422	0359	1497					
0027	marginal case	01	111	030	0529	0144	0233	0588					
0028	2003/11/12 10:54	06	123	346	0801	0199	0460	1360	2003/11/12 10:54:06	Halo	360	1197	2
0029	2003/11/12 12:06	00	212	012	1116	0075	0976	1201					
0030	2003/11/12 12:30	00	299	014	0948	0196	0822	1302					
0031	2003/11/12 12:54	03	180	040	1116	0585	0271	2403					
0032	2003/11/12 12:30	01	301	022	1335	0323	0915	1838					
0033	2003/11/12 12:30	00	210	012	1008	0165	0889	1302					
0034	2003/11/12 14:54	04	120	040	0529	0412	0229	1644					
0035	2003/11/12 12:54	01	236	020	1562	0000	1562	1562					
0036	2003/11/12 16:06	02	076	020	0868	0711	0395	1953					
0037	2003/11/12 18:30	03	264	128	0694	0156	0339	0976	2003/11/12 18:30:05	246	88	891	4
0038	marginal case	02	234	016	0589	0242	0228	0844					
0039	2003/11/12 22:30	01	165	026	0728	0169	0434	1041					
0040	2003/11/13 01:54	02	232	016	0600	0237	0229	0892					
0041	2003/11/13 05:30	03	116	028	0679	0092	0512	0892	2003/11/13 05:30:05	103	62	598	2
0042	2003/11/13 06:54	00	202	012	0466	0004	0466	0473	2003/11/13 06:54:05	202	18	444	1
0043	2003/11/13 09:54	05	—	360	1008	0476	0359	2083	2003/11/13 09:30:05	49	217	1141	4
0044	marginal case	01	116	012	0346	0083	0279	0496					
0045	2003/11/13 22:30	05	136	104	0355	0131	0182	0744	2003/11/13 22:30:05	130	113	554	3
0046	2003/11/14 11:06	02	273	046	0651	0095	0413	0844	2003/11/14 10:54:05	282	57	683	2
0047	2003/11/14 15:26	00	127	014	0987	0641	0219	1838					

Appendix C

The box-and-whisker plot

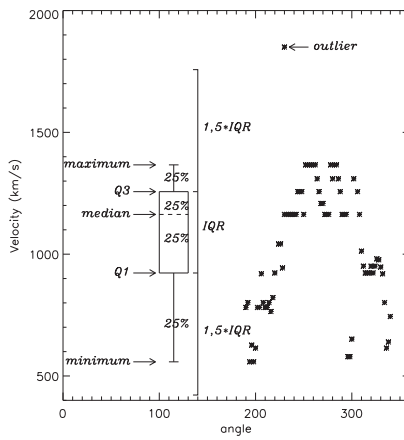


Figure C.1: Illustration of a box-and-whisker plot.

A box-and-whisker plot (or boxplot) is a graphical way of summarizing a set of data measured on an interval scale. It is often used in exploratory data analysis. For an illustration see Fig. C.1. The median (point at 50%) of the dataset is indicated by the dashed line, the first and third quartiles define the edges of the box, of which the length is called the inter-quartile range (IQR). Hence, the box always contains the central 50% of the data. The smaller the IQR is, the less variable the measurements are. The whiskers at both ends of the box each cover another 25% of the data. They reach up to the extreme values within 1.5 times the IQR from the edges of the box. Data points at a greater distance are regarded as outliers.

Nederlandstalige samenvatting

In deel I beschrijven we de eerste observaties van trage magnetoakoestische golven in coronale lussen. Deze observaties werden uitgevoerd in beelden van EIT aan boord van SOHO en TRACE. Deze twee instrumenten observeren de Zon in extreem ultraviolet licht (EUV), respectievelijk in de golflengten 195 Å en 171 Å. In deze hoge energieën worden de coronale magnetische structuren van de zon, het zogeheten ‘magnetische tapijt’, zichtbaar. Ook de reorganisatie van het magnetische veld en andere coronale activiteit kan waargenomen worden in deze hoge temperaturen. Het bestaan van golven in de corona was voorspeld door de theorie van de magnetohydrodynamica. Magnetoakoestische golven (cfr. geluidsgolven) veroorzaken veranderingen in dichtheid en kunnen geobserveerd worden als intensiteitsvariëaties die zich langs de voetpunten van coronale lussen voortbewegen. Gelijkaardige intensiteitsvariëaties werden ook waargenomen in coronale pluimen (Eng: coronal plumes) door Deforest and Gurman (1998). De verandering in intensiteit bedraagt slechts ongeveer 10% van de achtergrondintensiteit. Bijgevolg zijn ze maar vaag te onderscheiden boven het ruisniveau. Tegen de tijd dat ze de ‘top’ van de lus bereiken zijn ze volledig gedempt en worden ze onzichtbaar.

Uit onze analyse blijkt dat de gemeten snelheid waarmee deze verstoringen zich verplaatsen altijd kleiner is dan de geschatte geluidssnelheid. De snelheden die wij gemeten hebben zijn geprojecteerde snelheden en variëren rond 120 km/s voor de 195 Å golflengte en rond 85 km/s voor de 171 Å golflengte, met een foutenmarge van ± 10 km/s. De theoretische geluidssnelheden voor deze temperaturen zijn van de zelfde grootteorde, maar altijd hoger dan de geobserveerde snelheden: 192 km/s voor EIT en 152 km/s voor TRACE. Door het verschil tussen onze metingen en de geluidssnelheid te verklaren ten gevolge van projectie, leiden we een projectiehoek af van typisch 51 - 56°. Dit is in overeenstemming met het interval van $[30,70]^\circ$ dat we uit ‘randobservaties’ konden afleiden (wanneer het actief gebied zich aan de rand van de Zon bevond). In dezelfde lussen meten we systematisch een hogere snelheid in het warmer plasma (EIT, 195 Å) dan in het koeler plasma (TRACE, 171 Å). Dit bevestigt de interpretatie van deze verstoringen als geluidsgolven en niet als materie die zich verplaatst. Dit heeft als gevolg dat we grote snelheidsgradiënten meten in coronale lussen, wat suggereert dat coronale lussen grote temperatuursgradiënten hebben, gestructureerd volgens concentrische cirkels of dunne draadjes van verschillende temperatuur.

Ondanks de grote foutenmarge op onze metingen, onder andere ten gevolge van projectie, hebben we toch voldoende aanwijzingen die de interpretatie van magnetoakoestische golven ondersteunen. Overlappende observaties in verschillende golflengten kunnen in de toekomst geleverd worden door het AIA-instrument aan boord van SDO en het EUV-instrument aan boord van STEREO. Ook wordt er vooruitgang verwacht door het gebruik van geavanceerde beeldverwerkingstechnieken die momenteel in ontwikkeling zijn. In

de beschreven analyse hebben we een vast ‘pad’ gekozen door de coronale lussen met de hand te volgen. Kleine verplaatsingen van de lus worden geïnterpreteerd als intensiteitsvariaties en veroorzaken dus fouten in de metingen. Zulke fouten kunnen vermeden worden door automatisch een coronale lus te volgen. Daarenboven kan men ook het verband bestuderen tussen intensiteitsveranderingen en ruimtelijke oscillaties van de lus. Dit is interessant omdat we hieruit parameters van de corona kunnen af leiden, die niet direct waarneembaar zijn, zoals het magnetveld of de Alfvén snelheid. Dit indirect bepalen van parameters heet ‘coronale seismologie’, maar staat nog in de kinderschoenen. Door het grote aantal vrijheidsgraden en aannames blijven de onzekerheden op de berekende parameters groot.

In deel II beschrijven we de werking en resultaten van een softwarepakket CACTus (Computer Aided CME Tracking) dat we ontwikkeld hebben om automatisch coronale massa-uitstoten (CMEs) te detecteren in coronagrafe beelden van LASCO. Hiervoor hebben wij de observationele CME definitie vertaald in meetbare parameters. Volgens Hundhausen et al. (1984) en Schwenn (1995) wordt een coronale massa uitstoot in een coronograaf beeld gedefinieerd als *een heldere onafhankelijke structuur, die zich radieel verwijderd van de Zon*. CMEs werden voor het eerst geobserveerd en gedefinieerd in coronagrafe beelden. Tot nu toe bieden deze nog steeds de beste mogelijkheid om coronale massa uitstoten te observeren. Het LASCO experiment aan boord van SOHO bestaat uit drie coronografen: een intern geoculterde (C1) en twee extern geoculterde (C2 en C3). Het C1 instrument liep permanente schade op tijdens het verlies van contact met SOHO in 1998, waarna het niet meer kon gebruikt worden. C2 en C3 nemen beelden van de corona in zichtbaar licht. Hun gemeenschappelijk beeldgebied strekt zich uit van twee tot dertig zonnestrallen. De beelden worden gevormd door verstrooiing van zonlicht door electronen die zich in de corona bevinden. De theorie van de Thomson-verstrooiing maakt het ons mogelijk de elektronendichtheid af te leiden van de intensiteit van coronale structuren. Aldus wordt ook de massa van CMEs berekend onder bepaalde aannames. Naast CMEs, zijn ook andere structuren zichtbaar in deze coronografe beelden, zoals coronale stromers (Eng: coronal streamers), sterren, planeten, hoogenergetische deeltjes en kometen. We melden terloops dat met LASCO meer dan 1100 nieuwe kometen werden ontdekt.

Met de ontwikkeling van CACTus hebben we aangetoond dat het mogelijk is om automatisch CMEs te detecteren in coronagrafe beelden en ook hun belangrijkste parameters te meten. Deze zijn begin tijdstip, hoekgrootte, latitude (dit is de radiele richting in het LASCO beeldveld) en snelheid. Ter eerste validatie hebben we de performantie van CACTus getest voor een periode van zes dagen. Hiervoor hebben we de CACTus-detecties in deze periode vergeleken met de detecties uit de CDAW¹-catalogus. Dit is de standaard LASCO CME-catalogus en wordt manueel samengesteld door waarnemers van de Catholic University of America in samenwerking met het Naval Research Laboratory. Vijftien van de zestien CMEs die werden teruggevonden in de CDAW-catalogus werden door CACTus gedetecteerd met bijna hetzelfde begintijdstip en radiele richting. Voor de overige twee parameters (hoekgrootte en snelheid) werden grotere afwijkingen gemeten. Deze afwijkingen zijn niet louter een gevolg van verschil in meetmethode, maar eerder een gevolg van een te vage CME-definitie (zie boven). Deze definitie bood ‘nodige

¹CDAW staat voor ‘Coordinated Data Analysis Workshop’

en voldoende voorwaarden' voor de eerste observaties, maar nu de gegevens van betere kwaliteit zijn, moet ook de definitie van observatie verfijnd worden. Immers, elk ander helder verschijnsel dat radieel wegvliegt van de zon kan nu ook als CME of als deel ervan worden beschouwd. Dit noemen we de 'ambigüiteit van de CME-parameters'. Uit ons onderzoek blijkt dat de CME-hoekgrootte de minst duidelijk gedefinieerde CME-parameter is. Snelle CMEs drijven schokken voor zich uit. Ze kunnen direct waargenomen worden in coronografe beelden als heldere compressiegebieden of indirect als deflecties in coronale stromers. Stromerdeflecties worden door de waarnemer over het algemeen niet opgenomen bij de meting van de CME-hoekgrootte, maar een helder schokfront wel. Als gevolg worden verschillende CMEs gekwalificeerd als 'halo', terwijl in werkelijkheid het schokfront voor het 'halo' uiterlijk zorgt. Voor schokgerelateerde CMEs is de hoekgrootte dus een zeer onnauwkeurig gedefinieerde parameter. Uit onze statistische analyse volgt dat de hoekgrootte van een CME toch een goed gekozen parameter is beneden de 120° . De hoekgrootte kan geïnterpreteerd worden als de hoek van een kegel, met als top het centrum van eruptie op het zonneoppervlak en als centrale as de richting van CME-verplaatsing. Deze parameter kan dus het best gemeten worden in zijaanzicht, aan de rand van de zon. CMEs die uitbarsten dichtbij het centrum van de zonnenschijf bewegen zich voort langs de Zon-Aarde lijn. Voor deze CMEs vervalt de 'meetkundige' interpretatie van hoekgrootte als hoek van een kegel. In dit geval zal de basis van de kegel een 'halo' (of slechts een gedeeltelijke halo) rond de occulter vormen. Als gevolg daarvan kunnen we de hoek van de kegel niet meten. Met andere woorden, de hoekgrootte van een CME verandert van (of verliest zijn) betekenis rond 120° . De tweede parameter die het minst goed overeenkomt tussen beide catalogi is de CME snelheid. CACTus en CDAW hanteren een verschillende definitie. Deze parameter kan dus niet direct vergeleken worden. CACTus meet een snelheidsprofiel in functie van de hoek rond de occulter, terwijl CDAW enkel het snelste deel van de CME volgt. Onze software heeft aangetoond dat er in de meeste gevallen meerdere frontsnelheden kunnen gedetecteerd worden. Bijgevolg is het meten van één snelheid dus niet voldoende om de CME-snelheid te karakteriseren.

In hoofdstuk 5 hebben we de statistiek van de CACTus CME-catalogus vergeleken met die van de CDAW CME-catalogus, gebaseerd op de detecties van september 1997 tot december 2005 (cyclus 23). CACTus detecteert ongeveer het dubbele aantal CMEs dan er opgenomen zijn in de CDAW-catalogus. Dit is voornamelijk een gevolg van de inclusie van kleine CMEs. Alhoewel deze voldoen aan de observationele CME-definitie, worden ze niet als zodanig herkend door de CDAW-waarnemer. Onze statistische analyse toont dat de inclusie van deze kleine CMEs resulteert in significante verschillen in de verdelingsfuncties van hoekgrootte en latitude. Voor de hoekgrootte verandert de verdelingsfunctie van een lognormale verdeling (CDAW) naar een machtsverdeling (Eng: power-law; CACTus). Dit betekent dat de CACTus CME hoekgroottes θ verdeeld zijn volgens een functie

$$N(\theta) = N_0\theta^{-\alpha} \text{ met macht } \alpha \approx 1.6,$$

met $N(\theta)$ het aantal CMEs met hoekgrootte θ en N_0 een constante. Deze verdelingsfunctie werd bereikt voor alle jaren over meer dan één grootte-orde in het interval $[10, 100]^\circ$. De 'power law' suggereert dat magnetische herstructurering door CMEs een schaalinvariant proces is. Met andere woorden, er bestaat geen 'typische' CME-grootte. Dit is een belangrijk nieuw resultaat voor CMEs, maar is welbekend voor andere types van magnetische herstructurering (bijvoorbeeld zonnevlammen). Wanneer we de verdelingsfunc-

ties van de latitudes bekijken merken we op dat deze kleine CMEs tijdens de dalende fase van de zonnecyclus (2003-2005) geconcentreerd zijn in twee brede banden rond $\pm 50^\circ$ latitude, begrensd door de polaire coronale gaten aan de ene kant en door de activiteitsgordel (Eng: active region belt) aan de andere kant. Het feit dat ze niet willekeurig verspreid zijn over het zonneoppervlak wijst op de invloed van een onderliggend globaal mechanisme als drijfveer. Verder onderzoek naar deze sub-populatie van CMEs is nodig.

In sectie 5.2 bestuderen we het ‘CME-getal’ in functie van de zonnevlekkencyclus (cyclus 23). Het CME-getal wordt simpelweg gedefinieerd als het aantal CMEs dat per dag geteld wordt. Zoals hierboven vermeld is er nog geen eenduidigheid over wanneer heldere bewegende materie, gezien in LASCO, een CME is of niet. Hierdoor liggen de CME-getallen van CACTus en CDAW ver uit elkaar. Het CACTus CME-getal varieert van 2.5 CMEs tijdens zonneminimum naar 7.5 CMEs tijdens zonnemaximum, waarvan ongeveer de helft een hoekgrootte kleiner dan 20° heeft. De CME-curve volgt de zonnevlekkencurve met een vertraging van zes tot twaalf maanden. Dit fenomeen werd eerder al terug gevonden voor verschillende andere indicatoren van zonneactiviteit. Interessant is de vraag of deze verschuiving een uiting is van vertraging tussen de magnetische flux-opbouw in de corona (verschijnen van zonnevlekken) en de uitstoot ervan.

In het laatste hoofdstuk bespreken we bestaande automatische detectiemechanismen die in de laatste jaren werden ontwikkeld. ‘Solar Image Processing’ is een jonge wetenschap in de zonnefysica, maar wordt al langer toegepast in andere domeinen zoals de medische beeldvorming. Automatische verwerking van gegevens heeft verschillende voordelen en toepassingen. Ten eerste biedt het een *objectieve* benadering van gegevens en detectiemethoden. Ten tweede kan het gebruikt worden om *continu* gegevens te interpreteren en als input te gebruiken voor ruimteweersvoorspellingen. Ten derde biedt het de mogelijkheid om op een snelle manier veel gegevens te verwerken, zonder menselijke tussenkomst. Dit laatste is zeer belangrijk, aangezien we steeds meer data te verwerken krijgen op korte tijd. Een overvoed aan gegevens heeft intelligente meta-data nodig om ‘het kaf van het koren te scheiden’. Automatische beeldverwerking kan die data leveren. Naast coronografen zijn er nog tal van andere manieren om CMEs waar te nemen, zij het op indirecte manier. We bespreken de detectie van filamenten in $H\alpha$ beelden, dimmings en EIT golven in beelden in extreem UV-licht en protuberansuitbarstingen in radiogegevens. Deze ‘alternatieve’ bronnen vormen een belangrijke aanvulling op coronografe beelden. Ze kunnen complementaire informatie over CME-parameters verschaffen, zoals de heliceiteit van de CME. Deze parameter kan niet rechtstreeks gemeten worden in coronografe beelden. Nochtans is het een belangrijke parameter aangezien het mede de impact op het magneetveld van de Aarde bepaalt, in het geval de CME de omgeving van de Aarde bereikt.

Bibliography

- Alfvén, H., 1942, Existence of electromagnetic-hydrodynamic waves, *Nature*, 150, 405
- Altschuler, M. D., Newkirk, G., 1969, Magnetic Fields and the Structure of the Solar Corona. I: Methods of Calculating Coronal Fields, *Sol. Phys.*, 9, 131
- Andries, J., Arregui, I., Goossens, M., 2005, Determination of the Coronal Density Stratification from the Observation of Harmonic Coronal Loop Oscillations, *ApJ*, 624, L57–L60
- Antiochos, S. K., DeVore, C. R., Klimchuk, J. A., 1999, A Model for Solar Coronal Mass Ejections, *ApJ*, 510, 485–493
- Arge, C. N., Pizzo, V. J., 2000, Improvement in the prediction of solar wind conditions using near-real time solar magnetic field updates, *J. Geophys. Res.*, 105, 10 465–10 480
- Asai, A., Shimojo, M., Isobe, H., Morimoto, T., Yokoyama, T., Shibasaki, K., Nakajima, H., 2001, Periodic Acceleration of Electrons in the 1998 November 10 Solar Flare, *ApJ*, 562, L103–L106
- Aschwanden, M. J., 1987, Theory of radio pulsations in coronal loops, *Sol. Phys.*, 111, 113–136
- Aschwanden, M. J., 2004, *Physics of the Solar Corona. An Introduction*, Praxis Publishing Ltd.
- Aschwanden, M. J., 2005, Three Criteria to Discriminate between Elementary and Composite Coronal Loops, *ApJ*, 634, L193–L196
- Aschwanden, M. J., Fletcher, L., Schrijver, C. J., Alexander, D., 1999, Coronal Loop Oscillations Observed with the Transition Region and Coronal Explorer, *ApJ*, 520, 880–894
- Aschwanden, M. J., Nightingale, R. W., Alexander, D., 2000a, Evidence for Nonuniform Heating of Coronal Loops Inferred from Multithread Modeling of TRACE Data, *ApJ*, 541, 1059–1077
- Aschwanden, M. J., Nightingale, R. W., Tarbell, T. D., Wolfson, C. J., 2000b, Time Variability of the “Quiet” Sun Observed with TRACE. I. Instrumental Effects, Event Detection, and Discrimination of Extreme-Ultraviolet Microflares, *ApJ*, 535, 1027–1046

- Athay, R. G., White, O. R., 1978, Chromospheric and coronal heating by sound waves, *ApJ*, 226, 1135–1139
- Bachmann, K. T., White, O. R., 1994, Observations of hysteresis in solar cycle variations among seven solar activity indicators, *Sol. Phys.*, 150, 347–357
- Banerjee, D., O’Shea, E., Goossens, M., Doyle, J. G., Poedts, S., 2002, On the theory of MAG waves and a comparison with sunspot observations from CDS/SoHO, *A&A*, 395, 263–277
- Bemporad, A., Sterling, A. C., Moore, R. L., Poletto, G., 2005, A New Variety of Coronal Mass Ejection: Streamer Puffs from Compact Ejective Flares, *ApJ*, 635, L189–L192
- Bentley, R. D., 2002, EGSO - the next step in data analysis, in *ESA SP-477: Solspa 2001, Proceedings of the Second Solar Cycle and Space Weather Euroconference*, pp. 603–606
- Berghmans, D., 2002, Automated detection of CMEs, in *ESA SP-506: Solar Variability: From Core to Outer Frontiers*, (Ed.) J. Kuijpers, pp. 85–89
- Berghmans, D., Clette, F., 1999, Active region EUV transient brightenings - First Results by EIT of SOHO JOP80, *Sol. Phys.*, 186, 207–229
- Berghmans, D., Clette, F., Moses, D., 1998, Quiet Sun EUV transient brightenings and turbulence. A panoramic view by EIT on board SOHO, *A&A*, 336, 1039–1055
- Berghmans, D., Foing, B. H., Fleck, B., 2002, Automated detection of CMEs in LASCO data, in *ESA SP-508: From Solar Min to Max: Half a Solar Cycle with SOHO*, (Ed.) A. Wilson, pp. 437–440
- Bernasconi, P. N., Rust, D. M., 2004, Advanced Automated Solar Filament Detection and Characterization Code: Description, Performance, and Results, *AGU Fall Meeting Abstracts*
- Biesecker, D. A., Thompson, B. J., 2002, Can EIT Waves be used to Predict Halo CME Properties?, *Bulletin of the American Astronomical Society*, 34, 695
- Biesecker, D. A., Myers, D. C., Thompson, B. J., Hammer, D. M., Vourlidis, A., 2002, Solar Phenomena Associated with “EIT Waves”, *ApJ*, 569, 1009–1015
- Billing, D. E., 1966, *A guide to the Solar Corona*, New York: Academic Press
- Bohlin, J. D., Vogel, S. N., Purcell, J. D., Sheeley, Jr., N. R., Tousey, R., Vanhoosier, M. E., 1975, A newly observed solar feature - Macrospicules in He II 304 A, *ApJ*, 197, L133–L135
- Boursier, Y., Llebaria, A., Goudail, F., Lamy, P., Robelus, S., 2005, Automatic detection of coronal mass ejections on LASCO-C2 synoptic maps, in *Solar Physics and Space Weather Instrumentation*. Edited by Fineschi, Silvano; Viereck, Rodney A. *Proceedings of the SPIE*, Volume 5901, pp. 13–24 (2005)., (Eds.) S. Fineschi, R. A. Viereck, pp. 13–24

- Brekke, P., Kjeldseth-Moe, O., Harrison, R. A., 1997, High-Velocity Flows in an Active Region Loop System Observed with the Coronal Diagnostic Spectrometer (Cds) on SOHO, *Sol. Phys.*, 175, 511–521
- Brueckner, G. E., Howard, R. A., Koomen, M. J., Korendyke, C. M., Michels, D. J., Moses, J. D., Socker, D. G., Dere, K. P., Lamy, P. L., Llebaria, A., Bout, M. V., Schwenn, R., Simnett, G. M., Bedford, D. K., Eyles, C. J., 1995, The Large Angle Spectroscopic Coronagraph (LASCO), *Sol. Phys.*, 162, 357–402
- Chen, J., 1989, Effects of toroidal forces in current loops embedded in a background plasma, *ApJ*, 338, 453–470
- Clette, F., Muglach, K., Fludra, A., Mc Kenzie, D., Kankelborg, C., De Forest, C., 1998, JOP 80: High time resolution imaging study of coronal and transition region dynamics (EIT shutterless-mode campaign)
- Colaninno, R. C., Vourlidis, A., 2006, Analysis of the Velocity Field of CMEs Using Optical Flow Methods, in AAS/Solar Physics Division Meeting, p. 24.04
- Cremades, H., Bothmer, V., 2004, On the three-dimensional configuration of coronal mass ejections, *A&A*, 422, 307–322
- Cremades, H., Bothmer, V., 2005, Geometrical Properties of Coronal Mass Ejections, in IAU Symposium, (Eds.) K. Dere, J. Wang, Y. Yan, pp. 48–54
- Cremades, H., Bothmer, V., Tripathi, D., 2004, Properties of Structured Coronal Mass Ejections in Solar Cycle 23, in 35th COSPAR Scientific Assembly, p. 1939
- Crosby, N. B., Aschwanden, M. J., Dennis, B. R., 1993, Frequency distributions and correlations of solar X-ray flare parameters, *Sol. Phys.*, 143, 275–299
- Davey, A. R., Bogart, R. S., Dimitoglou, G., Gurman, J. B., Hill, F., Martens, P. C., Tian, K. Q., Wampler, S., 2003, First Steps Towards a VSO, AAS/Solar Physics Division Meeting, 34
- De Moortel, I., Ireland, J., Walsh, R. W., 2000, Observation of oscillations in coronal loops, *A&A*, 355, L23–L26
- De Moortel, I., Ireland, J., Walsh, R. W., Hood, A. W., 2002, Longitudinal intensity oscillations in coronal loops observed with TRACE - I. Overview of Measured Parameters, *Sol. Phys.*, 209, 61–88
- De Pontieu, B., Erdélyi, R., James, S. P., 2004, Solar chromospheric spicules from the leakage of photospheric oscillations and flows, *Nature*, 430, 536–539
- De Pontieu, B., Erdélyi, R., De Moortel, I., 2005, How to Channel Photospheric Oscillations into the Corona, *ApJ*, 624, L61–L64
- Deforest, C. E., Gurman, J. B., 1998, Observation of Quasi-periodic Compressive Waves in Solar Polar Plumes, *ApJ*, 501, L217

- Delaboudinière, J.-P., Artzner, G. E., Brunaud, J., Gabriel, A. H., Hochedez, J. F., Millier, F., Song, X. Y., Au, B., Dere, K. P., Howard, R. A., Kreplin, R., Michels, D. J., Moses, J. D., Defise, J. M., Jamar, C., Rochus, P., Chauvineau, J. P., Marioge, J. P., Catura, R. C., Lemen, J. R., Shing, L., Stern, R. A., Gurman, J. B., Neupert, W. M., Maucherat, A., Clette, F., Cugnon, P., van Dessel, E. L., 1995, EIT: Extreme-Ultraviolet Imaging Telescope for the SOHO Mission, *Sol. Phys.*, 162, 291–312
- Delannée, C., Delaboudinière, J.-P., Lamy, P., 2000, Observation of the origin of CMEs in the low corona, *A&A*, 355, 725–742
- Démoulin, P., Klein, K.-L., 2000, Structuring of the Solar Plasma by the Magnetic Field, in *LNP Vol. 553: Transport and Energy Conversion in the Heliosphere*, (Eds.) J. P. Rozelot, L. Klein, J.-C. Vial, p. 99
- Démoulin, P., Mandrini, C. H., van Driel-Gesztelyi, L., Thompson, B. J., Plunkett, S., Kovári, Z., Aulanier, G., Young, A., 2002, What is the source of the magnetic helicity shed by CMEs? The long-term helicity budget of AR 7978, *A&A*, 382, 650–665
- Donnelly, R. F., Heath, D. F., Lean, J. L., Rottman, G. J., 1983, Differences in the temporal variations of solar UV flux, 10.7-cm solar radio flux, sunspot number, and Ca-K plage data caused by solar rotation and active region evolution, *J. Geophys. Res.*, 88, 9883–9888
- Dryer, M., 1982, Coronal transient phenomena, *Space Science Reviews*, 33, 233–275
- Edlèn, B., 1942, Die Deutung der Emissionslinien im Spektrum der Sonnenkorona, *Z. Astrophys.*, 22, 30
- Edwin, P. M., Roberts, B., 1983, Wave propagation in a magnetic cylinder, *Sol. Phys.*, 88, 179–191
- Eriksen, G., Maltby, P., 1967, The Effect of Progressive Sound Waves on the Profiles of Stellar Spectral Lines, *ApJ*, 148, 833
- Fleck, B., Domingo, V., Poland, A., 1995, *The SOHO mission*, Dordrecht: Kluwer, [c1995, edited by Fleck, B.; Domingo, V.; Poland, A.
- Forbes, T. G., 2000, A review on the genesis of coronal mass ejections, *J. Geophys. Res.*, pp. 23 153–23 166
- Foukal, P. V., 1976, The pressure and energy balance of the cool corona over sunspots, *ApJ*, 210, 575–581
- Fuller, N., Abouadarham, J., 2004, Automatic detection of solar filaments versus manual digitization, *Lecture notes in computer science*
- Gao, J., Wang, H., Zhou, M., 2002, Development of an Automatic Filament Disappearance Detection System, *Sol. Phys.*, 205, 93–103
- Gissot, S., Hochedez, J.-F., 2007, Multiscale optical flow probing of dynamics in solar EUV images, *A&A*

- Gnevyshev, M. N., 1967, On the 11-Years Cycle of Solar Activity, *Sol. Phys.*, 1, 107
- Goedbloed, J. P. H., Poedts, S., 2004, *Principles of Magnetohydrodynamics*, Cambridge University Press
- Golub, L., Pasachoff, J. M., 1997, *The Solar Corona*, The Solar Corona, by Leon Golub and Jay M. Pasachoff, pp. 388. ISBN 0521480825. Cambridge, UK: Cambridge University Press, September 1997.
- Goossens, M., 2003, An introduction to plasma astrophysics and magnetohydrodynamics, *Astrophysics and Space Science Library*, Vol. 294. Dordrecht: Kluwer Academic Publishers
- Goossens, M., Andries, J., Aschwanden, M. J., 2002, Coronal loop oscillations. An interpretation in terms of resonant absorption of quasi-mode kink oscillations, *A&A*, 394, L39–L42
- Gopalswamy, N., 2004a, Chapter 8: A global picture of CMEs in the inner heliosphere, p. 201, ed. G. Poletto and S. Suess, KLUWER/Boston
- Gopalswamy, N., 2004b, A Global Picture of CMEs in the Inner Heliosphere, in *ASSL Vol. 317: The Sun and the Heliosphere as an Integrated System*, (Eds.) G. Poletto, S. T. Suess, p. 201
- Gopalswamy, N., Shimojo, M., Lu, W., Yashiro, S., Shibasaki, K., Howard, R. A., 2003, Prominence Eruptions and Coronal Mass Ejection: A Statistical Study Using Microwave Observations, *ApJ*, 586, 562–578
- Gosling, J. T., Hildner, E., MacQueen, R. M., Munro, R. H., Poland, A. I., Ross, C. L., 1974, Mass ejections from the sun - A view from SKYLAB, *J. Geophys. Res.*, 79, 4581–4587
- Gosling, J. T., Thomsen, M. F., Bame, S. J., Elphic, R. C., Russell, C. T., 1990, Cold ion beams in the low latitude boundary layer during accelerated flow events, *Geophys. Res. Lett.*, 17, 2245–2248
- Grotian, W., 1939, Zur Frage der Deutung der Linien im Spektrum der Sonnenkorona, *Naturwissenschaften*, 27, 214
- Handy, B. N., Acton, L. W., Kankelborg, C. C., Wolfson, C. J., Akin, D. J., Bruner, M. E., Carvalho, R., Catura, R. C., Chevalier, R., Duncan, D. W., Edwards, C. G., Feinstein, C. N., Freeland, S. L., Friedlaender, F. M., Hoffmann, C. H., Hurlburt, N. E., Jurcevich, B. K., Katz, N. L., Kelly, G. A., Lemen, J. R., Levay, M., Lindgren, R. W., Mathur, D. P., Meyer, S. B., Morrison, S. J., Morrison, M. D., Nightingale, R. W., Pope, T. P., Rehse, R. A., Schrijver, C. J., Shine, R. A., Shing, L., Strong, K. T., Tarbell, T. D., Title, A. M., Torgerson, D. D., Golub, L., Bookbinder, J. A., Caldwell, D., Cheimets, P. N., Davis, W. N., Deluca, E. E., McMullen, R. A., Warren, H. P., Amato, D., Fisher, R., Maldonado, H., Parkinson, C., 1999, The transition region and coronal explorer, *Sol. Phys.*, 187, 229–260

- Harra, L. K., Sterling, A. C., 2001, Material Outflows from Coronal Intensity “Dimming Regions” during Coronal Mass Ejection Onset, *ApJ*, 561, L215–L218
- Harrison, R. A., 1998, Scientific Achievements of SOHO: The Solar Atmosphere, in *ESA SP-417: Crossroads for European Solar and Heliospheric Physics. Recent Achievements and Future Mission Possibilities*, p. 19
- Hochedez, J.-F., Zhukov, A., Robbrecht, E., Van der Linden, R., Berghmans, D., Vanlommel, P., Theissen, A., Clette, F., 2005, Monitoring capabilities for solar weather nowcast and forecast, *Annales Geophysicae*, (submitted)
- Howard, R. A., 2006, A Historical Perspective on Coronal Mass Ejections, in *Geophysical Monograph 165: Solar Eruptions and Energetic Particles*, (Ed.) M. R. T. J. Gopalswamy, N., pp. 7–13
- Howard, R. A., Michels, D. J., Sheeley, Jr., N. R., Koomen, M. J., 1982, The observation of a coronal transient directed at earth, *ApJ*, 263, L101–L104
- Howard, R. A., Sheeley, Jr., N. R., Michels, D. J., Koomen, M. J., 1985, Coronal mass ejections - 1979-1981, *J. Geophys. Res.*, 90, 8173–8191
- Howard, R. A., Sheeley, Jr., N. R., Michels, D. J., Koomen, M. J., 1986, The solar cycle dependence of coronal mass ejections, in *ASSL Vol. 123: The Sun and the Heliosphere in Three Dimensions*, (Ed.) R. G. Marsden, pp. 107–111
- Howard, R. A., Moses, J. D., Socker, D. G., Dere, K. P., Cook, J. W., 2002, Sun earth connection coronal and heliospheric investigation (SECCHI), *Advances in Space Research*, 29, 2017–2026
- Hudson, H. S., Cliver, E. W., 2001, Observing coronal mass ejections without coronagraphs, *J. Geophys. Res.*, pp. 25 199–25 214
- Hundhausen, A. J., 1993, Sizes and locations of coronal mass ejections - SMM observations from 1980 and 1984-1989, *J. Geophys. Res.*, 98, 13 177
- Hundhausen, A. J., Sawyer, C. B., House, L., Illing, R. M. E., Wagner, W. J., 1984, Coronal mass ejections observed during the solar maximum mission - Latitude distribution and rate of occurrence, *J. Geophys. Res.*, 89, 2639–2646
- Hurlburt, N., Bose, P., Freeland, S., Woodward, M., Slater, G., 2004, Collaborative Virtual Observatories using CoSEC, *American Astronomical Society Meeting Abstracts*, 204
- Illing, R. M. E., Hundhausen, A. J., 1983, Possible observation of a disconnected magnetic structure in a coronal transient, *J. Geophys. Res.*, 88, 10 210–10 214
- Jackson, B. V., Hildner, E., 1978, Forerunners - Outer rims of solar coronal transients, *Sol. Phys.*, 60, 155–170
- Jacobs, C., Poedts, S., Van der Holst, B., Chané, E., 2005, On the effect of the background wind on the evolution of interplanetary shock waves, *A&A*, 430, 1099–1107

- Jahne, B., 2005, Digital image processing, Springer-Verlach
- Jeanquart, K., 2003, Computergestuurde detectie van coronale massa-uitstoten, Master's thesis, Katholieke Universiteit Leuven, Belgium
- Kahler, S. W., 1992, Solar flares and coronal mass ejections, *ARA&A*, 30, 113–141
- Kahler, S. W., 2006, Observational Properties of Coronal Mass Ejections, in *Geophysical Monograph 165: Solar Eruptions and Energetic Particles*, (Ed.) M. R. T. J. Gopalswamy, N., pp. 21–32
- King, D. B., Nakariakov, V. M., Deluca, E. E., Golub, L., McClements, K. G., 2003, Propagating EUV disturbances in the Solar corona: Two-wavelength observations, *A&A*, 404, L1–L4
- Kjeldseth-Moe, O., Brekke, P., 1998, Time Variability of Active Region Loops Observed with the Coronal Diagnostic Spectrometer (Cds) on SOHO, *Sol. Phys.*, 182, 73–95
- Kliem, B., Dammach, I. E., Curdt, W., Wilhelm, K., 2002, Correlated Dynamics of Hot and Cool Plasmas in the Main Phase of a Solar Flare, *ApJ*, 568, L61–L65
- Klimchuk, J. A., 2001, Theory of Coronal Mass Ejections, in *Space weather, Proc. Chapman Conference on Space Weather*, (Eds.) P. Song, H. Singer, G. Siscoe
- Kohl, J. L., Cranmer, S. R. (Eds.), 1999, Coronal Holes and Solar Wind Acceleration, *Proceedings of the SOHO-7 Workshop*.
- Koomen, M. J., Detwiler, C. R., Brueckner, G. E., Cooper, H. W., Tousey, R., 1975, White light coronagraph in OSO-7, *Appl. Opt.*, 14, 743–751
- Linker, J. A., Mikić, Z., Riley, P., Lionello, R., Odstroil, D., 2003, Models of Coronal Mass Ejections: A Review with A Look to The Future, in *AIP Conf. Proc. 679: Solar Wind Ten*, (Eds.) M. Velli, R. Bruno, F. Malara, B. Bucci, pp. 703–710
- Llebaria, A., Lamy, P., 1999, Time Domain Analysis of Solar Coronal Structures Through Hough Transform Techniques, in *ASP Conf. Ser. 172: Astronomical Data Analysis Software and Systems VIII*, (Eds.) D. M. Mehringer, R. L. Plante, D. A. Roberts, p. 46
- Low, B. C., 1982, Self-similar magnetohydrodynamics. I - The $\gamma = 4/3$ polytrope and the coronal transient, *ApJ*, 254, 796–805
- Low, B. C., 1984, Self-Similar Magnetohydrodynamics - Part Four - the Physics of Coronal Transients, *ApJ*, 281, 392
- Low, B. C., 2001, Coronal mass ejections, magnetic flux ropes, and solar magnetism, *J. Geophys. Res.*, 106, 25 141–25 164
- Low, B. C., Zhang, M., 2002, The Hydromagnetic Origin of the Two Dynamical Types of Solar Coronal Mass Ejections, *ApJ*, 564, L53–L56
- MacQueen, R. M., Fisher, R. R., 1983, The kinematics of solar inner coronal transients, *Sol. Phys.*, 89, 89–102

- MacQueen, R. M., Eddy, J. A., Gosling, J. T., Hildner, E., Munro, R. H., Newkirk, Jr., G. A., Poland, A. I., Ross, C. L., 1974, The Outer Solar Corona as Observed from Skylab: Preliminary Results, *ApJ*, 187, L85
- MacQueen, R. M., Csoeke-Poeckh, A., Hildner, E., House, L., Reynolds, R., Stanger, A., Tepoel, H., Wagner, W., 1980, The High Altitude Observatory Coronagraph/Polarimeter on the Solar Maximum Mission, *Sol. Phys.*, 65, 91–107
- Marsh, M. S., Walsh, R. W., 2006, p-Mode Propagation through the Transition Region into the Solar Corona. I. Observations, *ApJ*, 643, 540–548
- Mason, H. E., 1999, SOHO - Where has the Quiet Sun gone?, in *ASP Conf. Ser. 158: Solar and Stellar Activity: Similarities and Differences*, (Eds.) C. J. Butler, J. G. Doyle, p. 348
- Michalek, G., 2006, An Asymmetric Cone Model for Halo Coronal Mass Ejections, *Sol. Phys.*, 237, 101–118
- Moon, Y.-J., Choe, G. S., Wang, H., Park, Y. D., Gopalswamy, N., Yang, G., Yashiro, S., 2002, A Statistical Study of Two Classes of Coronal Mass Ejections, *ApJ*, 581, 694–702
- Moore, R. L., Sterling, A. C., 2006, Initiation of Coronal Mass Ejections, in *Geophysical Monograph 165: Solar Eruptions and Energetic Particles*, (Ed.) M. R. T. J. Gopalswamy, N., pp. 43–57
- Moses, D., Clette, F., Delaboudinière, J.-P., Artzner, G. E., Bougnet, M., Brunaud, J., Carabetian, C., Gabriel, A. H., Hochedez, J. F., Millier, F., Song, X. Y., Au, B., Dere, K. P., Howard, R. A., Kreplin, R., Michels, D. J., Defise, J. M., Jamar, C., Rochus, P., Chauvineau, J. P., Marioge, J. P., Catura, R. C., Lemen, J. R., Shing, L., Stern, R. A., Gurman, J. B., Neupert, W. M., Newmark, J., Thompson, B., Maucherat, A., Portier-Fozzani, F., Berghmans, D., Cugnon, P., van Dessel, E. L., Gabryl, J. R., 1997, EIT Observations of the Extreme Ultraviolet Sun, *Sol. Phys.*, 175, 571–599
- Mouradian, Z., Soru-Escout, I., Pojoga, S., 1995, On the two classes of filament-prominence disappearance and their relation to coronal mass ejections, *Sol. Phys.*, 158, 269–281
- Munro, R. H., Gosling, J. T., Hildner, E., MacQueen, R. M., Poland, A. I., Ross, C. L., 1979, The association of coronal mass ejection transients with other forms of solar activity, *Sol. Phys.*, 61, 201–215
- Nakajima, H., Nishio, M., Enome, S., Shibasaki, K., Takano, T., Hanaoka, Y., Torii, C., Sekiguchi, H., Bushimata, T., Kawashima, S., Shinohara, N., Irimajiri, Y., Koshiishi, H., Kosugi, T., Shiomi, Y., Sawa, M., Kai, K., 1995, NEW NOBEYAMA RADIO HELIOGRAPH, *Journal of Astrophysics and Astronomy Supplement*, 16, 437
- Nakariakov, V. M., Verwichte, E., 2005, Coronal Waves and Oscillations, *Living Reviews in Solar Physics*, 2, 3

- Nakariakov, V. M., Ofman, L., Deluca, E. E., Roberts, B., Davila, J. M., 1999, TRACE observation of damped coronal loop oscillations: Implications for coronal heating, *Science*, 285, 862–864
- Nakariakov, V. M., Verwichte, E., Berghmans, D., Robbrecht, E., 2000, Slow magnetoacoustic waves in coronal loops, *A&A*, 362, 1151–1157
- Nakariakov, V. M., Melnikov, V. F., Reznikova, V. E., 2003, Global sausage modes of coronal loops, *A&A*, 412, L7–L10
- Nightingale, R. W., Aschwanden, M. J., Hurlburt, N. E., 1999, Time Variability of EUV Brightenings in Coronal Loops Observed with TRACE, *Sol. Phys.*, 190, 249–265
- Ofman, L., Nakariakov, V. M., Deforest, C. E., 1999, Slow Magnetosonic Waves in Coronal Plumes, *ApJ*, 514, 441–447
- Olmedo, O., Zhang, J., Wechsler, H., Borne, K., Poland, A., 2005, Solar Eruptive Event Detection System (SEEDS), in *Bulletin of the American Astronomical Society*, p. 1342
- Özgüç, A., Ataç, T., 2001, Observations of Hysteresis Between Flare Index and Some Solar Indices, in *IAU Symposium*, (Eds.) P. Brekke, B. Fleck, J. B. Gurman, p. 125
- Pariat, E., Nindos, A., Démoulin, P., Berger, M. A., 2006, What is the spatial distribution of magnetic helicity injected in a solar active region?, *A&A*, 452, 623–630
- Parker, E. N., 1983, Direct coronal heating from dissipation of magnetic field, in *Solar Wind Conference*, (Eds.) J. M. Wilcox, A. J. Hundhausen, pp. 23–32
- Pevtsov, A. A., Balasubramaniam, K. S., Rogers, J. W., 2003, Chirality of Chromospheric Filaments, *ApJ*, 595, 500–505
- Plunkett, S. P., Thompson, B. J., Howard, R. A., Michels, D. J., St. Cyr, O. C., Tappin, S. J., Schwenn, R., Lamy, P. L., 1998, LASCO observations of an Earth-directed coronal mass ejection on May 12, 1997, *Geophys. Res. Lett.*, 25, 2477–2480
- Podladchikova, O., Berghmans, D., 2005, Automated Detection Of Eit Waves And Dimmings, *Sol. Phys.*, 228, 265–284
- Priest, E. R., 1984, *Solar magneto-hydrodynamics*, Geophysics and Astrophysics Monographs, Dordrecht: Reidel, 1984
- Qu, M., Shih, F. Y., Jing, J., Wang, H., 2005, Automatic Solar Filament Detection Using Image Processing Techniques, *Sol. Phys.*
- Qu, M., Shih, F. Y., Jing, J., Wang, H., 2006, Automatic Detection and Classification of Coronal Mass Ejections, *Sol. Phys.*, 237, 419–431
- Reale, F., Peres, G., Serio, S., DeLuca, E. E., Golub, L., 2000, A Brightening Coronal Loop Observed by TRACE. I. Morphology and Evolution, *ApJ*, 535, 412–422

Bibliography

- Richardson, I. G., Cliver, E. W., Cane, H. V., 2001, Sources of geomagnetic storms for solar minimum and maximum conditions during 1972-2000, *Geophys. Res. Lett.*, 28, 2569–2572
- Riley, P., Linker, J. A., Mikić, Z., Odstreil, D., Pizzo, V. J., Webb, D. F., 2002, Evidence of Posteruption Reconnection Associated with Coronal Mass Ejections in the Solar Wind, *ApJ*, 578, 972–978
- Robbrecht, E., Berghmans, D., 2004, Automated recognition of coronal mass ejections (CMEs) in near-real-time data, *A&A*, 425, 1097–1106
- Robbrecht, E., Berghmans, D., 2005, Entering The Era Of Automated CME Recognition: A Review Of Existing Tools, *Sol. Phys.*, 228, 239–251
- Robbrecht, E., Berghmans, D., 2006, A broad perspective on automated CME tracking: towards higher level Space Weather forecasting, in *Geophysical Monograph 165: Solar Eruptions and Energetic Particles*, (Ed.) M. R. T. J. Gopalswamy, N., pp. 33–41
- Robbrecht, E., Berghmans, D., Nakariakov, V., Poedts, S., 1999, Slow Magnetoacoustic Waves in Coronal Loops?, in *ESA SP-446: 8th SOHO Workshop: Plasma Dynamics and Diagnostics in the Solar Transition Region and Corona*, p. 575
- Robbrecht, E., Verwichte, E., Berghmans, D., Hochedez, J. F., Poedts, S., Nakariakov, V. M., 2001, Slow magnetoacoustic waves in coronal loops: EIT and TRACE, *A&A*, 370, 591–601
- Roberts, B., 2000, Waves and Oscillations in the Corona - (Invited Review), *Sol. Phys.*, 193, 139–152
- Roberts, B., Edwin, P. M., Benz, A. O., 1984, On coronal oscillations, *ApJ*, 279, 857–865
- Rosenberg, H., 1970, Evidence for MHD Pulsations in the Solar Corona, *A&A*, 9, 159
- Schatten, K. H., Wilcox, J. M., Ness, N. F., 1969, A model of interplanetary and coronal magnetic fields, *Sol. Phys.*, 6, 442–455
- Schrijver, C. J., Title, A. M., Berger, T. E., Fletcher, L., Hurlburt, N. E., Nightingale, R. W., Shine, R. A., Tarbell, T. D., Wolfson, J., Golub, L., Bookbinder, J. A., Deluca, E. E., McMullen, R. A., Warren, H. P., Kankelborg, C. C., Handy, B. N., de Pontieu, B., 1999, A new view of the solar outer atmosphere by the Transition Region and Coronal Explorer, *Sol. Phys.*, 187, 261–302
- Schrijver, C. J., Aschwanden, M. J., Title, A. M., 2002, Transverse oscillations in coronal loops observed with TRACE - I. An Overview of Events, Movies, and a Discussion of Common Properties and Required Conditions, *Sol. Phys.*, 206, 69–98
- Schwenn, R., 1995, Mass ejections from the sun and their interplanetary counterparts, in *Solar Wind Conference*, p. 45

- Sheeley, N. R., Walters, J. H., Wang, Y.-M., Howard, R. A., 1999, Continuous tracking of coronal outflows: Two kinds of coronal mass ejections, *J. Geophys. Res.*, 104, 24 739–24 768
- Sheeley, N. R., Hakala, W. N., Wang, Y.-M., 2000, Detection of coronal mass ejection associated shock waves in the outer corona, *J. Geophys. Res.*, 105, 5081–5092
- Sheeley, Jr., N. R., Michels, D. J., Howard, R. A., Koomen, M. J., 1980, Initial observations with the SOLWIND coronagraph, *ApJ*, 237, L99–L101
- Sheeley, Jr., N. R., Wang, Y.-M., Hawley, S. H., Brueckner, G. E., Dere, K. P., Howard, R. A., Koomen, M. J., Korendyke, C. M., Michels, D. J., Paswaters, S. E., Socker, D. G., St. Cyr, O. C., Wang, D., Lamy, P. L., Llebaria, A., Schwenn, R., Simnett, G. M., Plunkett, S., Biesecker, D. A., 1997, Measurements of Flow Speeds in the Corona between 2 and 30 R sub sun, *ApJ*, 484, 472
- Shih, F. Y., Kowalski, A. J., 2003, Automatic Extraction of Filaments in H α Solar Images, *Sol. Phys.*, 218, 99–122
- Shimojo, M., Shibata, K., Yokoyama, T., Hori, K., 1998, Physical parameters of solar X-ray jets, in *ESA SP-421: Solar Jets and Coronal Plumes*, p. 163
- Sime, D. G., Hundhausen, A. J., 1987, The coronal mass ejection of July 6, 1980 - A candidate for interpretation as a coronal shock wave, *J. Geophys. Res.*, 92, 1049–1055
- St. Cyr, O. C., Plunkett, S. P., Michels, D. J., Paswaters, S. E., Koomen, M. J., Simnett, G. M., Thompson, B. J., Gurman, J. B., Schwenn, R., Webb, D. F., Hildner, E., Lamy, P. L., 2000, Properties of coronal mass ejections: SOHO LASCO observations from January 1996 to June 1998, *J. Geophys. Res.*, 105, 18 169–18 186
- Svestka, Z., 1994, Slow-mode oscillations of large-scale coronal loops, *Sol. Phys.*, 152, 505–508
- Temmer, M., Veronig, A., Hanslmeier, A., 2003, Does solar flare activity lag behind sunspot activity?, *Sol. Phys.*, 215, 111–126
- Thompson, B. J., Plunkett, S. P., Gurman, J. B., Newmark, J. S., St. Cyr, O. C., Michels, D. J., 1998, SOHO/EIT observations of an Earth-directed coronal mass ejection on May 12, 1997, *Geophys. Res. Lett.*, 25, 2465–2468
- Tousey, R., 1973, The Solar Corona, in *Space Research*, (Eds.) M. J. Rycroft, S. K. Runcorn, p. 713
- Tripathi, D., Bothmer, V., Cremades, H., 2004, The basic characteristics of EUV post-eruptive arcades and their role as tracers of coronal mass ejection source regions, *A&A*, 422, 337–349
- van Ballegoijen, A. A., Martens, P. C. H., 1989, Formation and eruption of solar prominences, *ApJ*, 343, 971–984

- Veronig, A. M., Temmer, M., Hanslmeier, A., 2004, The solar soft X-ray background flux and its relation to flare occurrence, *Sol. Phys.*, 219, 125–133
- Verwichte, E., Nakariakov, V. M., Ofman, L., Deluca, E. E., 2004, Characteristics of transverse oscillations in a coronal loop arcade, *Sol. Phys.*, 223, 77–94
- Verwichte, E., Nakariakov, V. M., Cooper, F. C., 2005, Transverse waves in a post-flare supra-arcade, *A&A*, 430, L65–L68
- von Rosenvinge, T., Cane, H., 2006, Solar Energetic Particles: An Overview, in *Geophysical Monograph 165: Solar Eruptions and Energetic Particles*, (Ed.) M. R. T. J. Gopalswamy, N., pp. 103–114
- Vourlidas, A., Buzasi, D., Howard, R. A., Esfandiari, E., 2002, Mass and energy properties of LASCO CMEs, in *ESA SP-506: Solar Variability: From Core to Outer Frontiers*, (Ed.) A. Wilson, pp. 91–94
- Vourlidas, A., Wu, S. T., Wang, A. H., Subramanian, P., Howard, R. A., 2003, Direct Detection of a Coronal Mass Ejection-Associated Shock in Large Angle and Spectrometric Coronagraph Experiment White-Light Images, *ApJ*, 598, 1392–1402
- Wang, T., Solanki, S. K., Curdt, W., Innes, D. E., Dammach, I. E., 2002, Doppler Shift Oscillations of Hot Solar Coronal Plasma Seen by SUMER: A Signature of Loop Oscillations?, *ApJ*, 574, L101–L104
- Wang, T. J., Solanki, S. K., 2004, Vertical oscillations of a coronal loop observed by TRACE, *A&A*, 421, L33–L36
- Wang, Y.-M., Sheeley, N. R., 1992, On potential field models of the solar corona, *ApJ*, 392, 310–319
- Webb, D. F., Howard, R. A., 1994, The solar cycle variation of coronal mass ejections and the solar wind mass flux, *J. Geophys. Res.*, 99, 4201–4220
- Wu, S. T., Hu, Y. Q., Wang, S., Dryer, M., Tandberg-Hanssen, E., 1982, A mechanism for a class of solar coronal disturbances, *Ap&SS*, 83, 189–194
- Wu, S. T., Wang, A. H., Plunkett, S. P., Michels, D. J., 2000, Evolution of Global-Scale Coronal Magnetic Field due to Magnetic Reconnection: The Formation of the Observed Blob Motion in the Coronal Streamer Belt, *ApJ*, 545, 1101–1115
- Yashiro, S., Gopalswamy, N., Michalek, G., Howard, R. A., 2003, Properties of narrow coronal mass ejections observed with LASCO, *Advances in Space Research*, 32, 2631–2635
- Yashiro, S., Gopalswamy, N., Michalek, G., St. Cyr, O. C., Plunkett, S. P., Rich, N. B., Howard, R. A., 2004, A catalog of white light coronal mass ejections observed by the SOHO spacecraft, *Journal of Geophysical Research (Space Physics)*, 109, 7105
- Yurchyshyn, V., Yashiro, S., Abramenko, V., Wang, H., Gopalswamy, N., 2005, Statistical Distributions of Speeds of Coronal Mass Ejections, *ApJ*, 619, 599–603

- Yurchyshyn, V. B., Wang, H., Goode, P. R., Deng, Y., 2001, Orientation of the Magnetic Fields in Interplanetary Flux Ropes and Solar Filaments, *ApJ*, 563, 381–388
- Zhao, X. P., Plunkett, S. P., Liu, W., 2002, Determination of geometrical and kinematical properties of halo coronal mass ejections using the cone model, *Journal of Geophysical Research (Space Physics)*, 107, 13–1
- Zharkova, V. V., Ipson, S. S., Zharkov, S. I., Benkhalil, A., Abouadarham, J., Bentley, R. D., 2003, A full-disk image standardisation of the synoptic solar observations at the Meudon Observatory, *Sol. Phys.*, 214, 89–105
- Zhukov, A. N., 2004, Solar sources of geoeffective CMEs: a SOHO/EIT view, in *Proceedings IAU symposium*, No. 226
- Zhukov, A. N., Auchère, F., 2004, On the nature of EIT waves, EUV dimmings and their link to CMEs, *A&A*, 427, 705–716

